




Review

Metal-Supported Biochar Catalysts for Sustainable Biorefinery, Electrocatalysis, and Energy Storage Applications: A Review

Rubén Ramos, Víctor K. Abdelkader-Fernández, Renata Matos , Andreia F. Peixoto * 
and Diana M. Fernandes * 

LAQV-REQUIMTE, Departamento de Química e Bioquímica, Faculdade de Ciências, Universidade do Porto, 4169-007 Porto, Portugal; rrveldar@hotmail.com (R.R.); victorkarim@ugr.es (V.K.A.-F.); renata.matos@fc.up.pt (R.M.)

* Correspondence: andreia.peixoto@fc.up.pt (A.F.P.); diana.fernandes@fc.up.pt (D.M.F.); Tel.: +351-2-2040-2560 (A.F.P.)

Abstract: Biochar (BCH) is a carbon-based bio-material produced from thermochemical conversion of biomass. Several activation or functionalization methods are usually used to improve physicochemical and functional properties of BCHs. In the context of green and sustainable future development, activated and functionalized biochars with abundant surface functional groups and large surface area can act as effective catalysts or catalyst supports for chemical transformation of a range of bioproducts in biorefineries. Above the well-known BCH applications, their use as adsorbents to remove pollutants are the mostly discussed, although their potential as catalysts or catalyst supports for advanced (electro)catalytic processes has not been comprehensively explored. In this review, the production/activation/functionalization of metal-supported biochar (M-BCH) are scrutinized, giving special emphasis to the metal-functionalized biochar-based (electro)catalysts as promising catalysts for bioenergy and bioproducts production. Their performance in the fields of biorefinery processes, and energy storage and conversion as electrode materials for oxygen and hydrogen evolutions, oxygen reduction, and supercapacitors, are also reviewed and discussed.

Keywords: metal-supported biochar catalysts; electrocatalysis; oxygen reactions; supercapacitors; biodiesel production; reforming; hydrogenation; hydrodeoxygenation



Citation: Ramos, R.; Abdelkader-Fernández, V.K.; Matos, R.; Peixoto, A.F.; Fernandes, D.M. Metal-Supported Biochar Catalysts for Sustainable Biorefinery, Electrocatalysis, and Energy Storage Applications: A Review. *Catalysts* **2022**, *12*, 207. <https://doi.org/10.3390/catal12020207>

Academic Editor: Lucian Baia

Received: 9 January 2022

Accepted: 4 February 2022

Published: 9 February 2022

Publisher's Note: MDPI stays neutral with regard to jurisdictional claims in published maps and institutional affiliations.



Copyright: © 2022 by the authors. Licensee MDPI, Basel, Switzerland. This article is an open access article distributed under the terms and conditions of the Creative Commons Attribution (CC BY) license (<https://creativecommons.org/licenses/by/4.0/>).

Contents

1	Introduction	2
2	Production and Activation of Biochar	3
2.1	Thermochemical Production	4
2.2	Activation	4
3	Metal Functionalization	5
3.1	One-Step Method: In-Situ Synthesis	5
3.2	Two-Step Method: Post-Activation	6
4	Applications for Biorefinery Processes	6
4.1	Transesterification Reaction	7
4.2	Hydrogenation/Hydrodeoxygenation Reactions	9
4.3	Reforming and Gasification Reactions	12
4.4	Pyrolysis Reaction	17
4.5	Hydrolysis Reactions	19
4.6	Other Catalytic Reactions	20
4.6.1	Fischer–Tropsch Synthesis	20
4.6.2	Isomerization Reactions	21

5	Electrochemical Applications	21
5.1	Supercapacitors	21
5.2	ORR, OER, HER	37
5.2.1	Oxygen Reduction Reaction (ORR)	38
5.2.2	Oxygen Evolution Reaction (OER)	50
5.2.3	Hydrogen Evolution Reaction (HER)	51
5.2.4	Multifunctional Electrocatalysts	56
6	Conclusions	57

1. Introduction

Growing global concerns about climate change and environmental pollution are raising the search for alternative renewable and cost-effective resources that ensure sustainable development. As the most abundant and renewable natural reserve, biomass available from lignocellulose, crops, animal fats, and agricultural wastes is considered a promising substitute for fossil fuels [1]. It can be converted into materials, power, and value-added chemicals through distinctive processes including biochemical, thermochemical, physical, and mechanical transformations. Above all, thermochemical processes—such as pyrolysis, gasification, and hydrothermal treatments—are characterized by a strong efficiency, in terms of quality and yield, to provide biofuels (e.g., syngas and bio-oil) [2]. Furthermore, during thermochemical processing takes place the production of biochar as a solid carbon-rich residue formed via biomass thermal degradation (pyrolysis: 300–900 °C) [3] in an oxygen-limited environment. In comparison with other carbon materials typically synthesized by complex and energy-consuming processes (e.g., activated carbons, nanotubes/nanofibers and carbon black synthesized via vapor deposition, or polymer carbonization routes), biochar is a greener solid produced by cost-competitive processes that may valorize biomass wastes formed in forthcoming biorefineries, thus reducing their environmental impact [4,5]. The chemical and physical properties of BCH materials are extremely conditioned on the intrinsic nature of the biomass feedstock, as well as the employed production method [6]. Advantageously for its use as catalyst, biochar presents high mineral contents (mostly P, Ca, Mg, and K), enriched surface functional groups (mainly C-O, COOH, C=O, and OH), and a highly modifiable structure for the doping of a broad range of species [7]. However, some characteristics of as-produced biochar, such as a low surface area and a poor porosity, hamper its catalytic applications [8]. To overcome these limitations, various activation strategies are typically applied to endow biochar with an enhanced specific surface and porous network. Activated BCHs can acquire abundant chemical-active functional groups and multi-scale porous structure along with large surface area, displaying remarkable applications in fields related to environmental and agricultural practices [9]. Thus, a great deal of studies have focused on the benefits of biochar-based catalysts for removing water contaminant (inorganic metals, organic dyes, ions, etc.) [10], increasing crop yield (soil amendment) [11], NO_x removal [12], carbon capture and storage [13], or photocatalytic degradation of organics [14]. Additionally, biochar-based materials are highly appropriate to be used as a carbon support for metal functionalization due to its stability in basic and acidic media, large surface area (after activation) that enables high dispersion rates, and presence of many surface functional groups that enhance the anchoring of the metal precursors. For example, it has been suggested that alkali metals—such as Ca, Na, and K—govern transesterification reactions [15,16]. Other metals such as Fe and Ni are commonly used for gasification and pyrolysis reactions [17,18], whereas Ti, Sn, and Zr oxides emerge as relevant species in photocatalysis [19]. It is also prominent that magnetic phases like Fe₂O₃ or Fe₃O₄ provide excellent activity for the removal of water pollutants, together with magnetic properties that enable an easy recovery [20]. Equally, transition metal oxides/hydroxides—such as NiO, Co₃O₄, MnO₂, Co(OH)₂, and Ni(OH)₂—are frequently pseudo-capacitor materials [21], while precious metals like Pt or Ru have been proved active in the electro-oxidation of methanol [22].

Existing reviews condense biochar production methods, activation methodologies, and derived catalytic properties and applications, especially in fields such as restoration of soil/water and pollution control. Nevertheless, information about the different strategies to incorporate metal active phases onto biochar material and their main application fields remains occasional and segregated. Such divergent knowledge must be structured and critically reviewed to offer insights for the rational design of novel M-BCH materials. This review is devoted to discussing the applications of M-BCHs in three topical fields: (i) biorefinery processes, (ii) electrocatalysis, and (iii) energy storage (Figure 1). The links between biochar properties, added metal phases and catalytic performance will be revised to provide a critical overview, highlighting the most recent research advancements of M-BCH materials in catalytic applications for biomass conversion technologies and energy storage applications. Finally, current challenges and outlooks on how M-BCH materials will progress and, in particular, how can be expanded their applications into the three analyzed fields will be also discussed, expecting to encourage innovative findings.

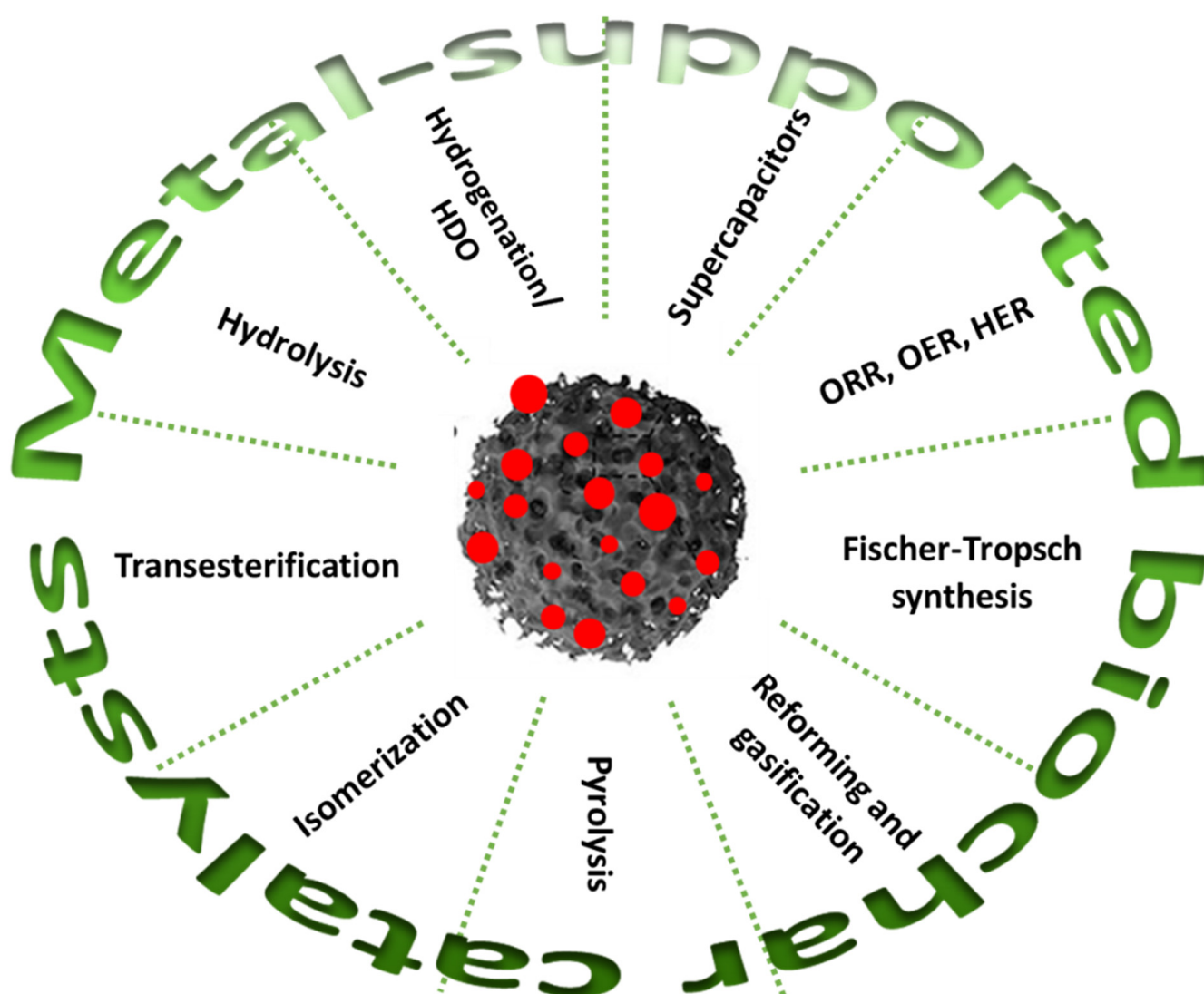


Figure 1. Overview of M-BCH applications in sustainable catalytic processes.

2. Production and Activation of Biochar

Biochar can be produced on a scale ranging from individual farms to large industrial facilities. Biomass degradation pathway to form biochar is a compromise of numerous and complex processes that vary significantly according to biomass nature, reaction medium,

and applied methodology. Abundant procedures and detailed mechanisms for biochar production and activation have been broadly reviewed and discussed in recent years. Hereby, we will only focus on explaining the main features derived from these methodologies.

2.1. Thermochemical Production

The production of biochar can be mostly divided into pyrolysis (slow and fast), hydrothermal carbonization (HTC), and gasification according to the different thermochemical processes, all under oxygen-limited conditions to avoid severe biomass oxidation. Typical operating conditions of slow pyrolysis platforms are within a temperature range of 300–900 °C with heating rates of 5–7 °C min⁻¹ and residence times longer than 1 h. During the slow pyrolysis process, high biochar yields can be obtained together with small quantity of bio-oil and syngas [23]. Alternatively, fast pyrolysis is a less energy-intensive method based on much higher heating rates (>200 °C min⁻¹) and shorter residence times (<10 s). It results in biochars with higher carbon content and stability, whilst having a negative impact on biochar yield (maximizing bio-oil formation) and on the number of surface functional groups [24]. Biochar can be also formed via biomass gasification at temperatures above 750 °C in the presence of oxidizing agents (e.g., air, O₂, and steam), producing syngas as the major product. While biochar from slow and fast pyrolysis presents a similar size of bonded aromatic ring cluster (7–8 rings), the biochar from high-temperature gasification has a more condensed structure (>15 rings) with a high level of alkali metals (Ca, K, Mg, etc.) [25]. Finally, through the HTC process the biochar production occur via depolymerization of cellulose, hemicellulose, and lignin at relatively lower temperature (180–250 °C) and under pressurized hydrothermal conditions. Additionally, biomass can be decomposed more easily in an aqueous medium than under pyrolysis conditions. For example, the decomposition of hemicellulose and cellulose occur at 180 °C and 230 °C, respectively, under hydrothermal conditions, whereas during pyrolysis hemicellulose totally degrades at 300 °C after c.a. 2 h, and cellulose begins decomposing at about 270–300 °C [26]. HTC biochar typically possesses a higher number of surface functional groups (mainly hydroxyl and carbonyl moieties) and a higher degree of microporosity (pore size < 2 nm) [27]. Lastly, HTC is a convenient technology for processing feedstock with high moisture contents (e.g., aquatic plants and algae) and for coating pre-formed nanostructures with carbonaceous shells [28].

2.2. Activation

Generally, the biochars obtained directly from biomass degradation present poor specific surface areas (<150 m² g⁻¹) and porosity compared to conventional activated carbon. Because high porosity and large surface areas are essential for applications in energy storage and catalysis, and can significantly enhance active phase loading, suitable activation process are required to enhance the catalytic properties of the as produced biochar materials. Furthermore, the activated biochar can provide more active sites and higher mass transfer capacities. Based on the activation agents/temperature/environment/time applied, activation processes can be in general separated into physical and chemical activation.

During the physical activation, the as-produced biochar is exposed to a controlled flow of steam and/or CO₂ at temperatures over 700 °C. Under these conditions, the gaseous agent leads to gasification processes via C–H₂O and/or C–CO₂ reactions, in which the oxidizing agent selectively removes the most reactive C atoms leading to the opening of closed pores and the interconnection of new pores and channels. Consequently, the specific surface area of the activated biochar is expressly enhanced, and a well-developed microporous structure with little contribution of mesopores is achieved. The physicochemical properties of physically activated biochar are strongly dependent on the feedstocks, activation temperature, oxidizing agent, and degree of activation [8]. There are several articles and reviews available highlighting the correlation of biochar physicochemical properties with the feedstocks, gaseous agents, and activation conditions selection [6–8]. It is reported that higher temperature and longer activation time can improve the development of porosity.

However, higher porosity developments are usually associated to a broadening of the pore size distribution which typically implies a lower selectivity due to the higher production of side products.

Regarding the chemical activation, the biochar is firstly impregnated in acid, alkaline or metal salt solutions using different activating agents such as H_2SO_4 , H_3PO_4 , KOH , ZnCl_2 , and K_2CO_3 . Next, the dried solid is pyrolyzed in presence of inert gas at a temperature range of 400–900 °C. Through a combination of dehydration/degradation reactions, the chemical agent triggers the release of gaseous species such as H_2O , CO , and CO_2 that eliminate reactive C atoms from the biochar matrix and promote the formation of new pores. Key factors in the chemical activation processes include activation temperature, features, and quantity of the chemical agent, biomass type, etc. [8]. Among the most commonly used activating agents, KOH mainly widens the microporosity, while ZnCl_2 contributes to both wide micropores and low mesopores; and H_3PO_4 develops large mesopores and even macropores. Comparing physical activation with chemical activation this latter achieves higher surface area and enhanced porosity at relatively lower temperatures [29]. However, this process needs a post-activation washing step to remove the impregnated agent and its respective salts. Additionally, there are even other complementary issues that limit the chemical activation treatment such as equipment corrosion, recycling of chemicals, and generation of secondary pollutants [29].

3. Metal Functionalization

Biochar functionalization is used to confer specific catalytic properties generally via surface alteration or incorporation of active metals. One of the most frequently used biochar modification method is sulfonation, which attaches biochar with $-\text{SO}_3\text{H}$ groups by addition of concentrated sulfuric acid (H_2SO_4) or its derivatives (e.g., HSO_3Cl , gaseous SO_3 , etc.) [16]. Sulfonated biochars can be extensively applied as solid acid catalysts for acid-driven catalytic reactions as hydrolysis, dehydration, polymerization, etc. [30]. The application of biochar-solid acids as effective catalysts is discussed in detail in other reviews [7,31]. Hereby, we focus on the incorporation of metals and/or metal oxides onto the biochar support by preloading the metal precursors into the biomass matrix before production (one-step method) or by impregnating biochars with the metal precursors after the thermo-physical or chemical activation step (two-step method), Figure 2 [32].

3.1. One-Step Method: In-Situ Synthesis

The metal precursor is mixed previously with biomass matrix using high-valent metal precursors before activation steps is a common method to produce M-BCH catalyst. Firstly, the biomass carbon precursor is impregnated with a metal solution (typically nitrates or chlorides), depositing metal ions onto the surface or interior of the biomass matrix. After drying, the metal precursor/biomass matrix is pyrolyzed (usually from 400 °C to 800 °C) converting metal ions to metal oxide nanoparticles or zero-valent metals (due to the release of strong reducing volatile compounds during activation pyrolysis such as CO_2). This method presents several advantages for the synthesis of biochar-supported metal nanoparticles (NPs) such as: (i) the activation/production of biochar and the reduction of metal NPs proceed simultaneously in one-step method, thus eliminating the use of additional reducing agents; (ii) the metal precursors may have some catalytic effects on the pyrolysis process itself, thus reducing the required activation conditions (temperature and pressure) and improving the porous structure of the final biochar; and (iii) the entire preparation process involves only one pyrolysis step, making it easy to scale up [8]. This one-step method can be also applied to prepare metal carbide-supported onto biochar catalysts. Typically, as the pyrolysis temperature increases, the added metal precursors can be transformed following the order metal salt/metal oxide/metal/metal carbide. Thus, if the pyrolysis temperature is high enough, the biochar can act not only as a support but also as a provider of carbon atoms for the production of active carbide composites [33–35].

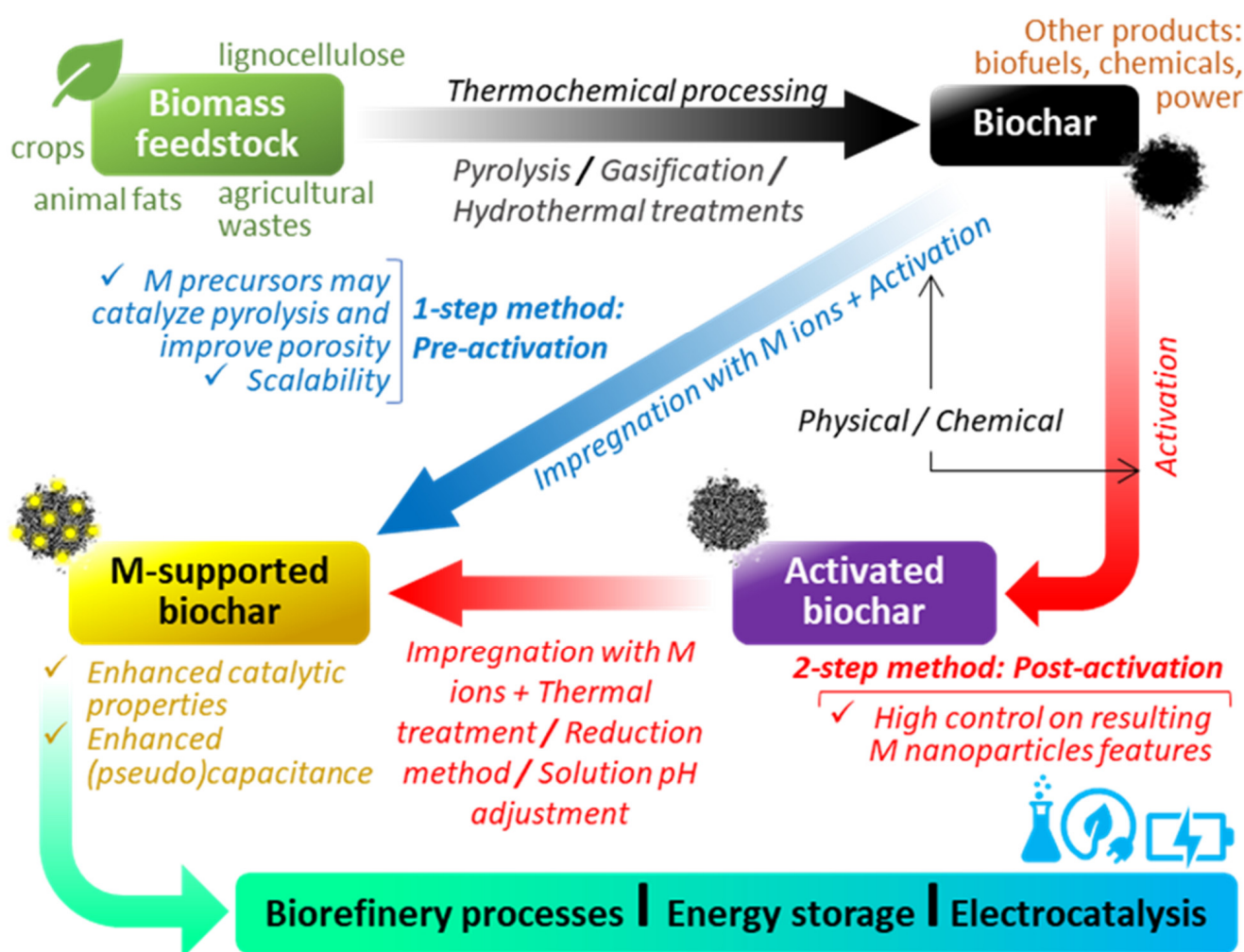


Figure 2. Schematic diagram of: one-step and two-step methodologies to metal-supported biochar synthesis, properties enhancement, and the advantages to the applications proposed in this review.

3.2. Two-Step Method: Post-Activation

Most of the biochar-based catalysts modified by the incorporation of metal phases are synthesized after the activation (chemical or physical) of the biochar support. Commonly, activated biochar is soaked into a solution of the corresponding metal salts, being metal ions adsorbed into the pores and surface of the biochar. Then, after further thermochemical processing, the attached metal oxides are precipitated onto the biochar matrix to form the composites by the reduction method, pyrolysis, adjustment of metal salt solution pH, and other methods [36]. Comparing with the one-step method, the size, shape, composition, and type of metal NPs are more easily controlled by using the two-step methodology. Monolayer, double-layer, and multilayer metal NPs supported onto biochar can simply be synthesized via post-activation. On the other hand, this method is relatively more complex and expensive, which makes it more difficult to upgrade into large-scale production [37].

4. Applications for Biorefinery Processes

Recent works to study the activation and functionalization of biochar-derived materials have revealed that their chemical stability and ability to fine-tune their structural properties, make them an appropriate catalyst support for the addition of metal species. Functionalized M-BCH catalysts can be applied for a broad variety of reactions involved in biorefineries processes to substitute the traditional petrochemical industry. In this section, the use of biochars as versatile catalyst supports for biomass upgrading is evaluated sorting

them into transesterification, reforming/gasification, pyrolysis, Fischer–Tropsch synthesis, hydrolysis, hydrogenation/hydrodeoxygenation, and isomerization reactions [3,29,32].

4.1. Transesterification Reaction

The transesterification reaction is generally used for the synthesis of biodiesel fuels from inexpensive and non-edible acid oils with high free fatty acids (FFAs) content (e.g., vegetable oils, microalgal oils, or animal fats). Biodiesel, composed of fatty acid alkyl esters, is an attractive carbon-neutral technology alternative to petroleum diesel, which has already been industrialized and commercialized. Transesterification reactions usually involve the use of short chain alcohols like methanol and ethanol, and the presence of acid and/or base catalysts (e.g., H_2SO_4 , KOH, and NaOH). Among heterogeneous catalysts (more easily recoverable and reusable), it is typical the preparation of solid acid catalysts by sulfonation methodologies (gaseous SO_3 or liquid H_2SO_4). Alternatively, biodiesel production can also be assisted by solid alkali catalysts (e.g., CaO, MgO, ZnO, CaZrO₃, etc.), but they are associate to cost limitation problems due to the requirement of expensive metal precursors. Despite the high yield of biodiesel produced from the different oils with fresh acid- or base-functionalized catalysts, most of the catalytic systems tended to deactivate after several recycling cycles, needing significant improvements to maximize their lifetime.

Biochar-based catalysts can also be applied to transesterification reactions, offering a cost competitive option for this industrialized process. Up to now, sulfonated biochar catalysts have been the most commonly used solution for biodiesel production [38]. Alternatively, solid alkali biochar-supported catalysts—such as K_2CO_3 /Biochar, KOH/Biochar, and CaO/Biochar—have attracted much attention to further convert high purity oils with low free fatty acid contents. Table 1 lists their catalytic efficiency and potential yield of biodiesel/fatty acid methyl esters (FAMES).

Table 1. Metal-supported biochar-based catalyst used in transesterification reactions for biodiesel production.

M-BCH Catalyst Preparation			Biodiesel Production			
Biochar Feedstock	Synthesis	Catalyst M-Support	Substrate	Reaction Conditions	FAME Yield	Ref.
Peat	Pyrolysis: 600 °C, 2 h/WI: K_2CO_3 (30 wt %)	KOH	Palm oil	Methanol (8:1); 65 °C, 1.5 h	98.6%	[39]
Pomelo peel	Pyrolysis: 600 °C, 2 h; treatment: 2 M KOH, 2 h; WI K_2CO_3 (15–35 wt %)	KOH	Palm oil	Methanol (8:1); 65 °C, 2.5 h	98%	[40]
Flamboyant pods	Pyrolysis: 500 °C, 1.5 h; steam flow treatment: 1.5–2.0 kg/cm ² , 300–400 °C. Impregnation: KOH, 30 °C, 24 h	KOH	Hevea brasiliensis oil	Methanol (15:1); 60 °C; 1 h	89.3%	[41]
Peat	Pyrolysis at 700 °C; treatment: 2 M KOH, 1 h. WI CaO (30 wt %); dry: 105 °C; calcined for 2 h at 600–800 °C in N ₂	KOH-CaO	Palm oil	Methanol (8:1); 65 °C; 2.5 h	93.4%	[15]
Avocado seeds	Pyrolysis: 900 °C; 2 h (N ₂ flow: 100 mL/min). Precipitation: aqueous solution $Ca(NO_3)_2 \cdot 4H_2O$; addition of NaOH 1.5 N at 70 °C; calcination: 900 °C, 2 h, N ₂	CaO	Sunflower oil	Methanol (15.6:1); 99.5 °C; 5 h	96%	[42]

Table 1. Cont.

M-BCH Catalyst Preparation			Biodiesel Production			
Biochar Feedstock	Synthesis	Catalyst M-Support	Substrate	Reaction Conditions	FAME Yield	Ref.
Bamboo powders	Pre-treatment: Aqueous solution of nickel nitrate, urea and bamboo powders, 135 °C, 10 h; dry: 105 °C. Pyrolysis: 700 °C. Aqueous sodium silicate solution at 85 °C to achieve a gel; Activation: 400 °C, 2 h, N ₂ ; milled with ZrO ₂ balls, 230 rpm, 12 h	Ni	Soybean oil	Methanol (9:1); 65 °C; 2 h	98.1%	[43]
Rice husk	Activation: 450 °C, 3 h, N ₂ ; Treatment: 1 M KOH, 105 °C, 3 h; washing: 1 M HCl; dry: 105 °C; impregnation: K ₂ CO ₃ (20 wt %) and Ni(NO ₃) ₂ ·6H ₂ O solutions; mixed for 6 h; Pyrolysis: 600 °C	Ni-KOH	Cooking oil	Methanol (12:1); 65 °C; 2 h	98.2%	[44]

WI: Wet impregnation; I: ImpW.

Wang et al., achieved a maximum biodiesel yield of 98.6% from palm oil at 65 °C and after 1.5 h using 30 wt % K₂CO₃ loaded peat biochar-derived catalyst [39]. Further increase in K₂CO₃ loading (up to 40%) showed a little improvement in biodiesel yield due to the crystallization or agglomeration of K compounds which resulted in poor dispersion of active species on the catalyst surface [45]. Similarly, Zhao and co-workers found that the porous pomelo peel biochar could also be used as support material for K₂CO₃ loading, obtaining up to 98% FAME yield under the same reaction conditions and after 2.5 h [40]. Both research groups concluded that the strong basic sites caused by the addition of K₂CO₃ resulted in the outstanding activity of biochar for the conversion of palm oil to FAME. Similarly, Dhawane et al., prepared (from flamboyant pods) and used a biochar, loaded with KOH by impregnation method, in the transesterification of *Hevea brasiliensis* oil with methanol at 65 °C, achieving 89.3% of biodiesel yield after 1 h reaction [41].

Various carbon material supported CaO catalysts have been also reported as solid-base catalysts for biodiesel production. Thus, a biochar obtained from peat and modified by impregnation with CaO was served for the transesterification reaction of palm oil [15]. The best performance was observed for the resulting 30 wt % CaO loading and 700 °C calcination temperature, with a maximum biodiesel yield of 93.4%. Excessive CaO (30–40 wt %) potentially influenced on decreasing textural properties and total basicity (coverage of the Ca₂SiO₄ phase). Equally, CaO impregnated biochar from the pyrolysis of avocado seeds was successfully employed as catalyst to produce biodiesel from waste oils [42]. The prepared catalytic systems promoted the transesterification with methanol with the advantage of an easy recover and reuse without loss of activity. By carrying out the reaction at 99.5 °C for 5 h, a FAME content of over 96% was achieved with final compositions conforming to the main EN14214 specifications. Although the above-mentioned potassium and calcium salts-loaded catalysts exhibited high catalytic activity in the transesterification reaction, they experienced harmful leaching problems. In this sense, it was observed by other authors that the formation of Ca–O–Si bond with Si from rice husk and peat matrix has been recently found to partly prevent Ca²⁺ ions leaching issues, increasing the catalysts' stability [46].

Apart of alkali metals, readily available transition metals like nickel biochar-based catalysts have been prepared and used in biodiesel production, showing a high recyclability arising from their magnetic nature. Thus, the Na₂SiO₃@Ni/C catalysts prepared from bamboo powders could be recycled four times with a biodiesel yield of over 93% [43].

Zhang et al., found significant advantages in this catalytic system (less corrosion, higher recovery, and enhanced stability for at least 10 cycles) compared with catalysts from traditional carbon sources, mainly due to more abundant acid/base functional groups as well as higher specific surface area and pore volume.

Very recently, the combination of alkali and Ni biochar-supported catalyst for the transesterification of used cooking oil was studied by Hazmi et al. [44]. This research group prepared a bifunctional magnetic nano-catalyst from rice husk by impregnating it with nickel and potassium oxide. A biodiesel yield of 98.2% was reached at 65 °C within 2 h of reaction. The catalyst showed to be reusable for up to five cycles. Due to the magnetic properties of this catalyst, it was easily recovered simplifying the separation and purification processes (Figure 3).

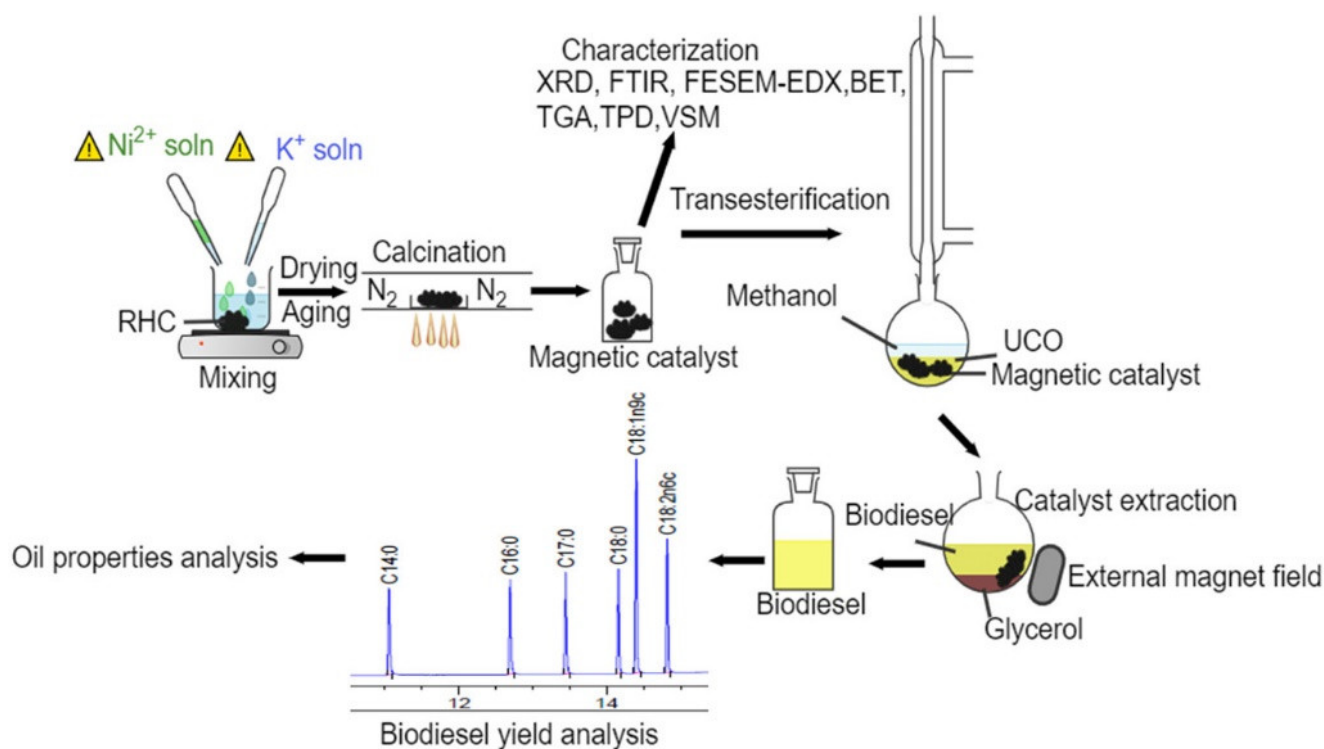


Figure 3. Bifunctional alkali (K)/metal (Ni) biochar-supported catalyst from rice husk for the transesterification of cooking oil. With permission from [44].

In summary, biochar-based catalysts are comparable to conventional non-biochar heterogeneous catalysts in terms of ester yield from triglycerides. However, for their practical use as catalysts for biodiesel production, the stability of biochar catalysts must be further studied to avoid the post-separation steps for removing metals. Therefore, it is still quite challenging to find more effective ways to synthesize robust M-BCH systems to avoid active centers leaching in reaction medium (FFA and water).

4.2. Hydrogenation/Hydrodeoxygenation Reactions

Biochar can be also applied as the catalyst support for the hydrotreating process (Table 2). There is a recent review on this topic by Wang et al. [3], with fresh advances in the preparation of M-BCH catalysts and catalytic performance for hydrogenation of biomass. Generally, metals like palladium, nickel, or cobalt have been developed as catalysts for catalytic reactions involving hydrogenation steps. Thus, a biochar-based catalyst for hydrodeoxygenation (HDO) was prepared by adding Ni onto the surface of biochar obtained from microalgae biomass pyrolysis (400 °C for 2 h) [17]. The obtained bio-oil from such pyrolysis was treated under H₂ pressure and over the as-synthesized Ni/biochar catalyst. The results showed that the Ni/biochar catalyst was very effective

in the HDO process, producing mainly n-heptadecane as a key component of diesel fuel. Alternatively, a novel magnetic Co-doped MoO₂/biochar was prepared by in-situ co-pyrolysis, and used to catalyze the HDO of guaiacol. The authors conclude that the synergy among Co, MoO₂, and biochar played a crucial role in H₂ and ethanol activation, allowing high conversions and selectivities (70% to arenes and 91.7% to phenols) [47].

Ni-Mo preloaded sawdust was also employed to prepare a M-BCH for the catalytic hydrogenation of lignin to produce chemical commodities [35]. Under mild reaction conditions, 61.3 wt % of lignin was converted to liquid products (phenols, guaiacols, and trimethoxybenzenes). This high catalytic performance, and its proved stability and reusability, was attributed to the synergistic effect of the graphitized biochar matrix and the Ni-Mo₂C nanoparticles which facilitates electron transfer. Based on the analysis of the products, the authors proposed that using the Ni-Mo₂C/BCH the potential mechanism for the reaction is the catalytic depolymerization of lignin. Another example of hydrogenation reaction over a M-BCH catalyst was carried out by Casoni et al. using sunflower seed hulls as raw material to produce furfuryl alcohol [48]. The method involved initial fast pyrolysis of the pre-treated hulls to produce bio-oil rich in furfural and biochar as a side product, followed by the catalytic hydrogenation of such furfural over Pd-supported biochar. High catalytic performance was observed under batch conditions, reaching yields of furfuryl alcohol of up to 48%.

In 2019, Ido et al., investigated the upgrading of algal crude oil over Ni-based (20 wt %) biochar produced from rice husk [49]. The synthesized catalyst was prepared by a KOH-treatment and activation with H₂SO₄ previous to impregnation. Additionally, biochars produced from rice straw and activated via pyrolysis under N₂ or a CO₂ environment to increase surface area and porosity were then employed as support to a bifunctional Ru-Re/biochar catalyst. The catalysts were used in the HDO of furan with the production of THF (>50%) and 1,4-butanediol (10–20%) as major value-added products [50,51]. Bimetallic Cu-Ni encapsulated in carbon catalysts were prepared by loading Ni and Cu onto biochar through wetness impregnation method and mild conditions. The catalysts were used in the HDO of 5-hydroxymethylfurfural (HMF) to produce 2,5-dimethylfurfural (DMF), a promising liquid fuel/fuel additive with 93.5% yield under optimized conditions. A synergistic effect of NiOx Lewis acidity in the activation of hydroxyl group in HMF and the neighboring of Cu–Ni alloyed particles in hydrogenolysis was illustrated by the authors the effect of temperature reaction variations to control the conversion pathways [52].

Table 2. Metal-supported biochar-based catalysts used in hydrogenation of biomass resources.

M-BCH Catalyst Preparation			Catalytic Biomass Upgrading			
Biomass Feedstock	Synthesis	Catalyst M-Support	Substrate	Reaction Type/Conditions	Yield (%)	Ref.
Microalgal	Two step synthesis: slow pyrolysis: 400 °C, 2 h/IWI: Ni(NO ₃) ₂ (0.2–M); reduction H ₂ /N ₂ flow	Ni/BCH	Microalgal bio-oil	HDO batch; 300 °C; H ₂ /N ₂ flow (10% volume of H ₂) 2 h	hydrocarbons (80%, n-heptadecane) oxygenated compounds (12%)	[17]
α-cellulose	One-step synthesis: Impregnation: cobalt nitrate and ammonium heptamolybdate; pyrolysis: 650 °C; passivation: RT, 2 h	Co-doped MoO ₂ -BCH	Guaiacol	HDO autoclave; 340 °C; 0.8 MPa H ₂ ; 4 h.	Arenes (70%); Phenols (91.7%)	[47]

Table 2. Cont.

M-BCH Catalyst Preparation			Catalytic Biomass Upgrading			
Biomass Feedstock	Synthesis	Catalyst M-Support	Substrate	Reaction Type/Conditions	Yield (%)	Ref.
Microcrystalline cellulose	Treatment: [BMim]Cl. Addition of H ₂ SO ₄ . Carbonization: 600 °C, 4 h, N ₂ flow. IWI (Bimetallic Cu–Ni)	Cu-Ni/BCH	HMF	HDO THF; 220 °C; 40 bar H ₂ , 1 h	DMF (93.5%)	[52]
Fir sawdust	One-step synthesis: impregnation: nickel chloride and ammonium heptamolybdate; pyrolysis: 800 °C	Ni–Mo ₂ C-BCH	Lignin	Hydrogenation; 250 °C, 2 h; 2 MPa H ₂	49 wt % yield to phenols, guaiacols, trimethoxybenzenes	[35]
Sunflower seeds hulls	Two-step synthesis: Treatment: phosphoric acid and zinc chloride; pyrolysis: 500 °C (200 mL min ⁻¹)/Precipitation: PdCl ₂ (5 wt %), 80 °C/Reduction: 37% formaldehyde solution	Pd/BCH	Furfural	Hydrogenation; batch; 110 °C; 0.4 MPa H ₂	Furfuryl alcohol (48%)	[48]
Rice husk	Pré-Treatment: KOH/Sulfonation: H ₂ SO ₄ ; 90 °C, 9 h/Impregnation: Ni(NO ₃) ₂ ·6H ₂ O (20 wt %), 65 °C, 4 h/Calcination: 500 °C, 4 h	Ni/BCH	Scenedesmus obliquus microalgae oil	Hydrotreatment; 246 °C; 3.72 (w/w) dodecane/oil; 3.84 MPa H ₂ ; 6 h	69.4% liquid-phase biofuel	[49]
Rice straw	Pyrolysis at 550 °C under N ₂ or CO ₂ atmosphere IWI with (HReO ₄ and RuCl ₃) dried at 110 °C; reduced at 300 °C for 2 h under an H ₂ flow of 300 mL/min	Ru-ReO _x -BCH	Furan	HDO 160 °C under 30 bar H ₂	THF (>50%) and 1,4-butanediol (10–20%)	[52,53]
Coconut shell	Oxidized with 20 wt % HNO ₃ at 85 °C for 4 h; washed and dried at 105 °C. Impregnation with PdCl ₂ , NiCl ₂ ·6H ₂ O and HCl aqueous solution; reduced with of 1 mol/L KBH ₄	Pd–Ni–B/BCH	Nitronaphthalene and <i>p</i> -chloronitrobenzene	250 mL vessel with 100 mL of tetrahydrofuran; 110 °C; 3.0 MPa H ₂ ; 4 h	99.6% conversion	[53]
Vine shoots	Deminerlization/Pyrolysis (800 °C): physical (CO ₂) and chemical activation (ZnCl ₂); IWI (palladium (II) acetate).	Pd/BCH	Vanillin	HDO water; 100 °C; 30 bar H ₂ ; 3 h	100% conversion p-creosol (92%)	[54,55]

IWI: incipient wet impregnation.

A Pd-Ni-B amorphous alloy incorporated in coconut shell activated carbon allowed a nearly 100% conversion of nitroaromatic compounds [53]. This illustrates the great potential of M-BCH as a solid catalyst for other analogous industrial processes.

Santos et al. [54] presented recently the synthesis and characterization of real waste biomass vine shoot biochars. Different activation methods were used to improve the poor textural properties of pristine biochar. A combination of physical (CO₂) and chemical activation (ZnCl₂) was evaluated. The chemical activation treatment with ZnCl₂ significantly increased the surface area and pore volume of the biochars. The authors used incipient wet impregnation (IWI) to support a series of noble metal catalysts (Pd, Au, and Ru). The Pd-supported biochar catalyst showed to be the most promising catalyst in HDO of vanillin with a complete conversion after 3 h with a selectivity for *p*-creosol of 92% [55].

The presented works in Table 2 details the use of different M-BCH catalyst to biomass hydro-upgrading processes. Due to biochar oxygen-containing functional groups, rich pore structure, and long catalytic life, it is an excellent structure to support metal phases allowing to excellent catalytic activity and selectivity in hydrogenation and hydrodeoxygenation reactions. These works, although using distinct model substrates (only two studies used real bio-oil), [17,49] offers important mechanistic insights for biomass upgrading. Performing the reactions with phenolic and furan derivatives model compounds, it is possible to find that noble metal-supported biochar catalysts exhibits better performance in hydrogenation and non-noble metal-supported biochar catalysts favors deoxygenation which is a result of their effective oxygen affinity ability. A synergistic effect of the combination of bimetals can strongly improve hydrogenation/deoxygenation, so further studies of catalyst optimization are necessary to enhance the potential of M-BCH catalysts for biomass upgrading in the biorefinery context [3].

4.3. Reforming and Gasification Reactions

Reforming or steam gasification of biomass is a promising renewable route, as it can facilitate the mass production of syngas (mixture of H₂ and CO) that can be further used as feedstock for the synthesis of fuels, platform molecules, and fine chemicals. However, this process involves the production of solid tar, an unavoidable by-product made of a mixture of heavily condensable hydrocarbons such as toluene, naphthalene, styrene, phenol, and other polycyclic aromatic hydrocarbons (Figure 4). Formation of tars deposits in pipelines and equipment damage, clog, and block downstream processes, consume feedstock carbon atoms, and hence, reduce the yield of syngas. Thus, the removal and/or mitigation of tar is a critical step to commercialize the biomass reforming/gasification process for syngas production. Dolomite, olivine, nickel, alkali metals are commonly used catalysts for tar cracking [56]. However, these conventional catalysts suffered from deactivation arising from coking and poisoning during the process. Alternatively, many efforts have been made to decompose tars in a secondary reactor with more robust noble metal catalysts (e.g., Rh, Pt, and Pd), nevertheless the necessary recovery due to their high costs remains a challenging task for the application of this approach. Therefore, it is desirable to use inexpensive catalysts for tar decomposition. In this respect, several M-BCH have been reported as catalysts to enhance syngas production, reduce tar fraction or to meet both goals concurrently (Table 3).

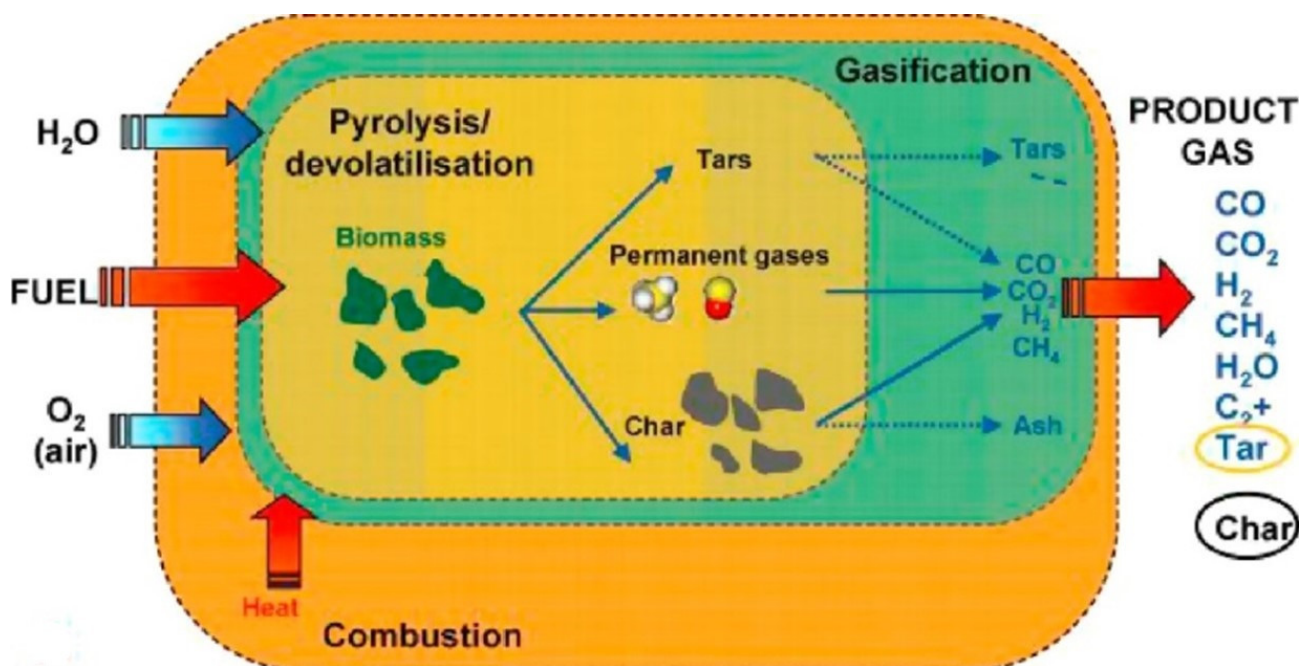


Figure 4. Main chemical transformations during biomass conversion in a gasifier. With permission of [57]. Copyright Clearance Center Inc. (2010).

Table 3. Metal-supported biochar-based catalysts used in reforming/gasification reactions for syngas production and/or tar decomposition.

M-BCH Preparation			Syngas Production and/or Tar Decomposition				Ref.
Biochar Feedstock	Synthesis	Catalyst M-Support	Substrate	Reaction Conditions	Syngas Production	Tar Removal Efficiency	
Rice husk	Pyrolysis at 700 °C; IWI with Ni(NO ₃) ₂ ·6H ₂ O; reduction: (i) pyrolysis at 700 °C, (ii) addition of NaBH ₄	Ni-BCH	Rice husk	Reforming; 1 L min ⁻¹ ; 800 °C	-	96.5%	[58]
	Reforming; 1 L min ⁻¹ ; 750 °C			LHV = 11.32 MJ/m ³	96.9–98.6%	[59]	
	IWI with Ni(NO ₃) ₂ ·6H ₂ O and Fe(NO ₃) ₃ ·9H ₂ O; dried at 105 °C; reduced: (i) pyrolysis at 600 °C, (ii) addition of NaBH ₄	Ni-Fe-BCH	Reforming; 1 L/min; 800 °C	Higher CO/CO ₂ ratio	92.3%	[60]	
	Pyrolysis at 500 °C; carbonization at 700 °C; treated with KOH (5 mol L ⁻¹); filtered and dried at 110 °C; calcined at 700 °C. Impregnation with nickel nitrate (10 wt %); filtrated and dried at 110 °C; pyrolyzed at 500 °C	Ni-BCH	Reforming; LHSV 10 h ⁻¹ ; 700 °C	71.2% H ₂ yield	-	[61]	

Table 3. Cont.

Biochar Feedstock	M-BCH Preparation		Substrate	Syngas Production and/or Tar Decomposition			Ref.
	Synthesis	Catalyst M-Support		Reaction Conditions	Syngas Production	Tar Removal Efficiency	
Red cedar	Gasification; treated with KOH; calcined at 800 °C for 1.5 h. Impregnated with Ni nitrate; reduced in H ₂ flow at 350 °C	Ni-BCH	Lignin	Reforming at 0.1–2.2 MPa; 700–900 °C; 1–5 µL water	-	70%	[62]
	Gasification; treated with KOH and NaOH. Treated with HNO ₃ (30 vol%); impregnated with Ni salts (10 wt %)	Ni-BCH	Toluene	Reforming with water at 800 °C	-	99%	[63]
Wheat straw, rice husk and cotton stalk	Fast pyrolysis at 500 °C. Impregnation with Ni(NO ₃) ₂ ·6H ₂ O (5–20 wt %); dried at 105 °C; pyrolyzed at 800 °C	Ni-BCH	Wheat straw	Steam gasification in a two-stage fixed bed reactor; 600–900 °C	92 mg H ₂ /g biomass	-	[64]
Oak wood	Mechanically mixing with NiO (5–20 wt %); reduce in Ar/H ₂ at 800 °C	NiO-BCH	Syngas	Reforming at lab-scale gasifier; 650–850 °C; 0.1–1.2 s	H ₂ and CO increase up to 34% and 32%, respectively	97%	[18]
Pine bark	Pyrolysis at 950 °C for 2 h. Impregnated with iron nitrate (9–13 wt %); dried at 105 °C; calcined at 300 °C in air	Fe-BCH	Toluene	Reforming at 400–900 °C; 1 atm N ₂ (700 mL min ⁻¹)	-	Conversion 91%. Benzene selectivity = 0.02%	[65]
Mallee wood	Soaked with FeCl ₃ solution (0.2 mol L ⁻¹) for 24 h; pyrolyzed to 630 °C for 30 min	Fe-BCH	Mallee wood	Steam gasification; 4.4 kg h ⁻¹ ; 880 °C	Enhance formation of H ₂ and CO	95%	[66]
Japanese cedar	Impregnated with ammonium heptamolybdate (5–30 wt %); calcined in Ar flow at 800 °C	Mo ₂ C-BCH	Japanese cedar	Reforming at 650 °C; 0.09 g min ⁻¹ ; RT; 1 atm	H ₂ production x5 vs. non catalytic test	99%	[68]
Pine sawdust	Fast pyrolysis; pre-treated with 0.1 mol L ⁻¹ HNO ₃ at 100 °C for 12 h; filtered and washed with H ₂ O (pH ≈ 7); dried at 105 °C. IWI with ammonium molybdate tetrahydrate (15 wt %); dried at 105 °C; calcined with Ar at 800 °C for 2 h	Mo ₂ C-BCH	CH ₄	Reforming with CO ₂ in a fixed-bed tubular reactor at 0.5 MPa; GHSV = 4000–12,000 h ⁻¹	CH ₄ conversion of 94%		[33]

Table 3. Cont.

Biochar Feedstock	M-BCH Preparation		Syngas Production and/or Tar Decomposition				Ref.
	Synthesis	Catalyst M-Support	Substrate	Reaction Conditions	Syngas Production	Tar Removal Efficiency	
Pine wood	Soaking wood chips in KOH solution, (10 wt %); dried at 105 °C; calcined at 700 °C in N ₂	K-BCH	Bio-oil	Gasification at 700 °C; GHSV of 237 h ⁻¹	H ₂ yield ≈ 0.5 m ³ kg ⁻¹ CO yield = 0.3 m ³ kg ⁻¹	×10 vs. parent biochar	[69]
	Fast pyrolysis. Boiled in 0.1 mol L ⁻¹ HNO ₃ ; washed and dried at 105 °C. Impregnation with ammonium tungstate; heated to 80 °C for 30 min and dried at 110 °C. Carbothermal reduction in N ₂ (50 mL min ⁻¹) at 1000 °C for 1–3 h	WC-BCH	Bio-gas	Reduction at 800 °C in H ₂ /N ₂ flow Reforming with CO ₂ ; 0.5 MPa, 6000 h ⁻¹ ; 600–900 °C	90% CO		[70]
Corncobs	1 mol L ⁻¹ HCl solution pyrolysis at 600 °C, 5% Ni loading	Ni-BCH	Toluene	Reforming W/F = 0.5 h, S/C = 3, 1 vol.% of toluene in gas, 1 atm 400–650 °C	H ₂ , CO, CO ₂ , CH ₄		[72]
	IWI with Ni(NO ₃) ₂ ·6H ₂ O and H ₃ BO ₃ ; dried 105 °C; calcined 600 °C in N ₂ for 30 min	Ni/B-BCH	Toluene	Steam reforming W/F = 0.25 h, S/C = 3; 600 °C; 1–10 h	-	>60% conversion	[67]
Palm shells	Carbonized at 850 °C in N ₂ for 30 min Impregnation with K ₂ CO ₃ and Fe(NO ₃) ₃ ·9H ₂ O for 12 (5 wt %), dried at 105 °C for 24 h	Fe-BCH	Toluene and naphthalene	Steam reforming 0.17–0.51 s, 90 min, 730–900 °C	-	80% conversion	[71]

Shen and co-workers prepared a Ni supported on rice husk biochar catalyst for the in-situ production of syngas and conversion of tar via reforming of rice husk [58,59]. It was found that the carbothermal reduction of the NiO nanoparticles during the pyrolysis of the biochar enhanced the catalytic performance of the catalyst (maximum tar removal efficiency of 98.6%). It is noteworthy that the syngas fuel characteristics were improved for power generation, corresponding to an increase in the lower heating value from 10.25 to 11.32 MJ m⁻³. Bimetallic Ni-Fe supported rice husk biochar was also explored for tar conversion via in-situ dry reforming by the same research group [60]. This study showed tar removal yields of 92.3–93%, together with an increase in the heating value of the gaseous products due to a higher CO/CO₂ ratio. Similarly, by fast pyrolysis of rice husk followed by IWI with nickel, Chen et al. developed a series of novel Ni biochar-based catalysts for the steam reforming of acetic acid in a continuous reactor [61]. The best catalytic performance was found with biochar catalyst activated by KOH combined with HNO₃ reflux. Acetic acid conversion and hydrogen yield reached 91.2% and 71.2%, respectively.

Ni loaded on red cedar biochar was also effectively used to reduce the contents of lignin tar by Qian et al., reaching up to 70% tar removal efficiency [62]. In this work, the effects of reaction temperature, water amount, pressure and atmosphere (inert and hydrogen) were assessed, showing that the increase of temperature and pressure lead to higher removal of most tar components (except for naphthalene). On the other hand, the decrease in the water loading resulted in lower tar removal efficiencies. In a similar study, the same research group tested Ni-supported red cedar biochar catalysts for the steam reforming of toluene [63]. They found that the catalysts prepared from nickel nitrate

precursor had superior catalytic performance than that of nickel acetate because of their much smaller average Ni particle size, reaching tar removal efficiencies of 99%.

Aiming at increasing hydrogen production from biomass steam gasification, a series of Ni-based biochar catalysts were investigated by Yao et al. using a two-stage fixed bed reactor [64]. The textural and chemical composition characterization of cotton stalk, rice husk, and wheat straw biochar derived catalysts suggested that the interaction between volatiles and biochar endorsed the reforming of pyrolysis gases. Thus, the cotton-biochar supported Ni exhibited the highest activity of H₂ production (64 vol.%, 92 mg g⁻¹) due to the higher content of alkali and alkaline earth metallic species (AAEMs) and also the much higher external surface area, while rice-biochar showed the lowest (35 mg g⁻¹). In a similar study, Wang et al., studied wood and coal chars supported Ni catalysts prepared by mechanically mixing NiO and oak wood chips at different ratio [18]. The synthesized catalysts removed more than 97% of tars in syngas reforming at 800 °C, also significantly increasing the concentration of H₂ (up to 34%) and CO (up to 32%).

Iron-supported biochar (13–19 wt %) produced from pine bark were described as an efficient catalyst for toluene (a model tar compound) decomposition with conversion approached to 91% (at 800 °C for 4 days) [65]. Relative to pristine biochar, the presence of Fe nanoparticles lowered the activation energy by 47% and decreased the formation of benzene (selectivity of 0.02%), an intermediate in toluene decomposition. Similar studies have been carried out to examine the effects of Fe in biochar as a catalyst for the reforming of tar during the gasification of mallee wood in a pilot plant [66]. The tar contents were drastically reduced to concentration levels below 100 mg m⁻³ (95%), especially on large aromatic ring systems. The Fe species in the mallee wood-derived biochar tended to enhance the formation of H₂ and CO during the reforming reactions in the catalytic reactor. In addition, the tested Fe loaded biochar catalyst bed also acted as effective filters to arrest the volatilized alkali and alkaline earth metallic species and ash fine particles from the raw gasification product gas. The performance of B doping Ni/B-BCH catalysts were also study for steam reforming of toluene [67]. The authors found that B doping significantly enhance the lifetime of Ni/BCH catalysts and simultaneously reduces the gasification consumption rate of the biochar support and coke deposition on the Ni particles. The authors evaluated the variation of B content using 600 °C, a space-time defined as the ratio of catalyst mass to the mass flow rate of toluene (W/F) of 0.25 h, and a steam/carbon (S/C) ratio of 3 and observed that the catalysts with a 3.5 wt % of B-doping showed the best stability under the selected reaction conditions.

Kaewpanha et al. reported an active Mo₂C loaded biochar catalyst for the catalytic steam reforming of tar derived from Japanese cedar [68]. The results exhibited a good catalytic performance at relatively low carburization temperatures (optimum found at 650 °C) and Mo loading (<30 wt %). In the case of Mo₂C/biochar with 20 wt %, the highest H₂ yield was obtained (ca. 22 mmol g⁻¹), which is about 5 times higher than that of the non-catalytic test. Nanostructured molybdenum carbide on biochar derived from pine sawdust was also used for CO₂ reforming of CH₄ [33]. The Mo₂C/Biochar carbide was prepared from a simple procedure of carburization with molybdate salts and without using extra carbon source or reducing gas. By temperature programmed surface reactions, it was possible to conclude that CH₄ dissociated as CH₄ ⇌ C + 2H₂ on the catalyst surface, and CO₂ reacted as CO₂ + C ⇌ 2CO⁺ due to oxidation of Mo₂C at 850 °C, reaching both CH₄ and CO₂ conversions higher than 80%.

In addition to catalytic steam reforming of tar, biochar catalysts were also employed for reforming other bioderived resources such as bio-oil or bio-gas. Thus, for the gasification of bio-oil at 700 °C, Postma et al., developed a potassium salt loaded biochar catalyst [69]. Both the K dissolved in the pyrolysis oil feed and the K-loaded biochar catalysts were found to enhance the gas yield (ca. 0.5 m³/kg) and prevent the formation of large tar species. Another metal-supported phase tested in the reforming of methane was tungsten carbide nanoparticles on a pine-wood derived biochar support [70]. Characterization results exposed the transformation of tungsten oxide (WO₃) to tungsten carbide nanoparticles

(WC) during pyrolysis steps. During CO₂ reforming, CH₄ conversion decreased with an increasing in CH₄/CO₂ ratio, whereas CO₂ conversion increased with an increase in CH₄/CO₂ ratio. Stability testing of the tungsten carbide nanoparticles in the biochar matrix revealed no catalyst deactivation during the 500 h test. Palm shell chars were impregnated with K- and Fe- and it was also found that these functionalized palm shell chars exhibited much better catalytic activity than palm shell char for tar reforming. The results indicated that prepared palm shell char had excellent catalytic activity for reforming toluene and naphthalene, showing conversions of 80% in a short residence time of 0.17 s at 900 °C. In contrast to CaO, palm shell char presented relatively low selectivity to benzene, and its spontaneous gasification allowed to generate extra syngas [71].

All of the studies summarized in Table 3, indicate that M-BCH catalysts are a promising alternative to remove tar in reforming/gasification reactions. Biochar as itself exhibits a fair catalytic activity for tar reforming usually influenced by surface area, pore size, and mineral content. Nickel and Iron-biochar-based catalysts seems to be good alternatives to the expensive noble-metal catalysts. The main drawback associated to its use is reaction temperature, as tar removal typically proceeds only at temperatures higher than 700 °C (vs. ≈550 °C with conventional Ni catalysts) [73]. Hence, upcoming efforts need to focus on overpassing these limitations and widen biochar suitability to milder reforming/gasification conditions. In this sense, microwave heating is an emerging method that could improve tar treatment using biochar catalysts by providing advantages such as high heating rates, volumetric heating, and thermochemical reaction acceleration [74].

4.4. Pyrolysis Reaction

Along with reforming, pyrolysis at 500–900 °C is another effective method to break down chemical bonds of biomass molecules and produce H₂-rich gas (Table 4). Thereby, the strategy of impregnating lignocellulosic resources such as beech wood with aqueous metal salts of Ni was applied in the pyrolysis of such wood at 700 °C [75,76]. The oxygenated groups present in the biochar acted as adsorption sites for metal cations, yielding a highly dispersed distribution of metallic Ni species into the wood matrix. Through carbothermal reduction (400–500 °C), the in situ formed Ni nanoparticles exhibited a higher catalytic activity for aromatic tar conversion (60–70%) and an enhanced H₂ production (57–91%) than preformed Ni species added into the biomass prior to pyrolysis. Their results showed that the Ni²⁺ was reduced to Ni⁰, leading to a highly dispersed Ni metallic phase on the biochar surface (avg. particle size ≈ 4 nm). By a primary vacuum impregnation, it was possible to optimize the Ni into the wood rate and generate stronger interactions with the lignocellulosic matrix through the formation of inner-sphere complexes, as well as enhance the penetration of Ni²⁺ cations in the cellulose crystalline zones (Figure 5).

Table 4. Metal-supported biochar-based catalysts used in the pyrolysis of biomass resources.

Biochar Feedstock	M-BCH Preparation		Pyrolysis of Biomass			
	Synthesis	Catalyst M-Support	Substrate	Reaction Type and Conditions	Yield (%)	Ref.
Beech wood	Impregnation with nickel nitrate; filtrated, washed and dried at 60 °C; pyrolyzed at 400–500 °C	Ni-BCH	Oak wood	Pyrolysis at 700 °C	H ₂ concentration increased by 260%	[76]
Beech wood	Vacuum impregnation with nickel nitrate solutions (0.1–1 mol L ⁻¹) at 25 °C; filtrated and dried at 60 °C; carbothermal reduction at 500 °C	Ni-BCH	Beech wood	Pyrolysis in stainless-steel horizontal tube; 40 L h ⁻¹ ; 700 °C	91% H ₂ vs. 60–70% for pristine wood	[75]

Table 4. Cont.

M-BCH Preparation			Pyrolysis of Biomass			
Biochar Feedstock	Synthesis	Catalyst M-Support	Substrate	Reaction Type and Conditions	Yield (%)	Ref.
Switchgrass	Pyrolysis at 500 °C; 30 min. Impregnated with iron oxide and nickel nitrate at 50 °C; kept for 24 h; dried at 103 °C	Fe-BCH	Acetic acid	Pyrolysis at 450 °C under N ₂ flow 42 cm ³ s ⁻¹	40.6% conversion	[77]
Beech wood	Impregnated with nickel nitrate (1 mol L ⁻¹); 3 days; 293 K; filtered, washed and dried at 323 K; calcined at 850 °C	Ni-BCH	Methane	Pyrolysis; 5% of CH ₄ in Ar; 900 °C; 10 °C/min; 1 h; 100 mL min ⁻¹	527 mmol g ⁻¹ H ₂ production	[78]
<i>Chlorella vulgaris</i> microalgae	Washed with HCl; activated with KOH at 80 °C; calcined at 700 °C in N ₂ . IWI with Fe ₃ (NO ₃) ₉ H ₂ O (2.5–10 wt %); calcined at 400 °C; dried at 105 °C	Fe-BCH	<i>Chlorella vulgaris</i> microalgae	Pyrolysis in dual-bed reactor 450–850 °C in Ar (30 mL min ⁻¹)	Bio-oil with HHV of 31.26 MJ kg ⁻¹	[79]

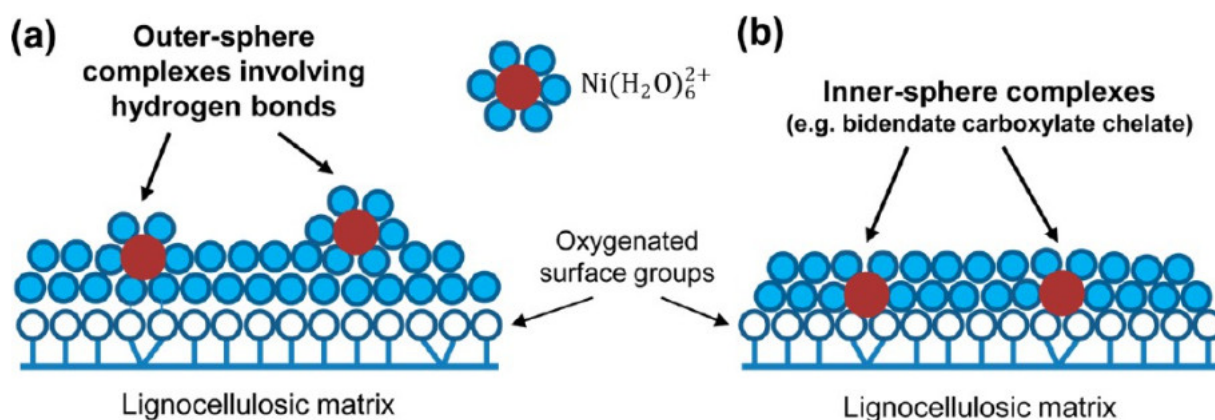


Figure 5. Effect of the impregnation method on Ni²⁺ adsorption mechanisms; (a) atmospheric pressure impregnation and (b) vacuum impregnation [75]. Reprinted with permission from [75]. Copyright (2013) American Chemical Society.

Aiming at evaluating thermal degradation capabilities for acetic acid at 450 °C, Poggi and Singh synthesized switchgrass-derived biochar catalysts and impregnated it with nickel nitrate and iron oxide [77]. Both samples showed acetic acid degradation capability higher than traditional FCC catalyst (12.4%), which resulted especially promising in case of the iron-modified biochar with a total conversion of 40.6%. However, leaching carbon from the biochar structure makes this catalyst not suitable for the studied purpose. Equally, Guizani et al. prepared a beech wood derived biochar catalyst loaded with Ni for studying the decomposition of methane by catalytic cracking in N₂ [78]. The raw chars exhibited a moderated catalytic activity in methane cracking, while the Ni-loaded chars showed a catalytic activity 10 times higher reaching 527 mmol of H₂ per gram of substrate. Thus, these works prove that the preloading of metal precursor into the biomass matrix is a suitable strategy to prepare efficient biochar-based catalysts for biomass pyrolysis.

On the other hand, to determine the best operational conditions for producing high-quality bio-oil, *Chlorella vulgaris* microalgae pyrolysis was investigated using its Fe-BCH catalysts [79]. Thus, various concentrations of iron (2.5, 5, and 10 wt %) were used to

impregnate the pristine and KOH-activated biochars. In non-catalytic experiments at 650 °C, the highest bio-oil yield was 51.22 wt %, whereas energy recovery achieved 58.51%. In catalytic experiments using the prepared biochar-based samples, the energy recovery factor was increased to 71.58%, with a high heating value of 31.26 MJ kg⁻¹.

4.5. Hydrolysis Reactions

As the most abundant biopolymers in biomass, the effective conversion of cellulose and hemicelluloses into valuable platform compounds—such as sugars, furfural, or 5-hydroxymethylfurfural HMF—is a highly desirable processing. Hydrolysis involves the breakage of glycosidic bonds in polysaccharides to release monosaccharides and in general it is initiated by a Brønsted acid (proton) at temperatures ranging from 80 to 250 °C. However, Lewis acids (electron pair acceptor) may also weaken glycosidic bond by coordinating with the oxygen atom. Produced sugars may also undergo dehydration by Brønsted acid driven steps (120–200 °C) producing furanic compounds.

Hydrolysis by using enzymes, mineral acids, and solid acids, have been traditionally employed in biomass upgrading. However, the enzymatic hydrolysis of cellulose and hemicelluloses is slow and costly, whereas mineral acids are usually difficult to recycle. In contrast, sulfonated biochar is a promising Brønsted-acid catalyst due to its high reaction activity and low cost. Nevertheless, the recyclability of sulfonated biochar is in question, for which metal impregnation may be a viable alternative for catalytic hydrolysis. Thus, several recent studies reported metal-functionalized biochar to modify pure sulfonated catalysts (Table 5).

Table 5. Metal-supported biochar-based catalysts used in hydrolysis of biomass resources.

Biochar Feedstock	M-BCH Preparation		Hydrolysis of Biomass			
	Synthesis	Catalyst M-Support	Substrate	Reaction Type and Conditions	Yield (%)	Ref.
Corncob	Mixed with tin (IV) hydroxide and cobalt (II) hydroxide; dried by rotary evaporation at 45 °C under 0.09 MPa; carbonized in N ₂ at 100–200 °C for 38 h	SnO ₂ -Co ₃ O ₄ -BCH	Corncob	Hydrolysis in batch autoclave at 180 °C, for 200 min	Furfural 30%	[80]
Bamboo	Carbonization at 700 °C and sulfonation with H ₂ SO ₄ for 4 h at 80 °C. Treated with aqueous solution of NaCl; dried at 120 °C; treated with (IL)-ZnCl ₂ ; acidified by HCl; washed and dried at 120 °C	IL-Zn-BCH-SO ₃ H	Cellulose and bamboo	Microwave-assisted hydrolysis; 2.45 GHz; 350–750 W; 90–110 °C for 2 h	Sugars (60%) HMF (30%)	[81]
	Carbonization at 700 °C and sulfonation with H ₂ SO ₄ for 3 h at 80 °C. Treated with NaCl; dried at 120 °C; treated with (IL)-CuCl ₂ ; acidified by HCl; washed and dried at 120 °C	IL-Cu-BCH-SO ₃ H			Sugars (35%) HMF (10%)	[82]
	Mixing with 2 mol L ⁻¹ NaOH or 1 mol L ⁻¹ Na ₂ CO ₃ solutions; dried at 105 °C; pyrolyzed at 400–600 °C; washed by 1 mol L ⁻¹ H ₂ SO ₄ at 100 °C		Cellulose	Hydrolysis; 150 °C; 12 h	TRS (58.6%) Glucose (43.5%)	[83]

The corncob hydrolysis to furfural over $\text{SnO}_2\text{-Co}_3\text{O}_4$ /biochar prepared from lignocelluloses residue of corncob degradation was studied by Liu et al. [80]. A maximum furfural yield of 30% was achieved at 180 °C and 200 min, indicating Lewis driven xylose isomerization as a key step for increasing furfural production. The dehydration of xylose is promoted by the hydrolysis of glycosidic bond which is supported by the Brønsted acid density (0.538 mmol/g) generated by the reaction of the metals with hydroxyl ions from water. In order to further improve activity of the solid acid-biochar catalyst in hydrolysis reaction, ionic liquid-modification methods were applied. Thus, Zhang et al., reported chlorozincate and chlorocuprate ionic liquid-functionalized biochar sulfonic acid catalysts for cellulose and bamboo hydrolysis to reduce sugars and HMF. Biochar supports were prepared using bamboo powder as a carbon resource, followed by calcination and sulfonation treatments [81,82]. It was found that the Cu and Zn salts played a better synergistic role to improve acidity in the $-\text{SO}_3\text{H}$ groups and catalyze the cleavage of cellulose and bamboo bonds under microwave irradiation (350–750 W). In another attempt to enhance the hydrolysis of cellulose, Wei et al. improved the properties of bamboo-derived biochar by molten alkali carbonates pyrolysis, obtaining a catalyst with superior surface area and porous structure compared to non-treated and alkali impregnation materials [83]. This biochar was employed as a catalyst support of biochar-bearing sulfonic acid groups, achieving remarkable yields of TRS and glucose (52.8% and 43.5%). These sugars from the hydrolysis of cellulose can be further exploited to produce alcohols. These works indicated that the combination of Lewis and Brønsted acids is a key factor to led to the conversion of biopolymers towards high yields of total reduced sugars and furans.

4.6. Other Catalytic Reactions

M-BCH catalysts have been also employed in other catalytic reactions, although in a restricted extension, including Fischer–Tropsch and isomerization of monomeric aldoses obtained from hydrolysis of lignocellulosic biomass. The summary of this published results is also here in represented:

4.6.1. Fischer–Tropsch Synthesis

In addition to generate heat/power or producing natural gas, ammonia or methanol, syngas can be also converted into fuels and chemicals through Fischer–Tropsch reaction over biochar-based catalysts. For example, Yan et al., used biochar from the fast pyrolysis of pine wood as the support for iron nanoparticles using impregnation methodology of iron nitrate and calcination at 1000 °C [84]. Characterization results revealed that the nanoparticles had core–shell structures with iron in situ encapsulated within a graphitic shell. The Fischer–Tropsch synthesis were performed in a fixed-bed reactor at 310 °C, 6.7 MPa with GHSV = 2000 h^{-1} using the carbon-encapsulated iron nanoparticles which showed to be highly active on conversion of bio-syngas (CO conversion ca. 95%), together with a significant selectivity towards liquid C5–C13 hydrocarbons (68%; with olefins as the dominant product).

Ruthenium activated biochar derived from the fast pyrolysis of lauan at 773 K with further activation with KOH (5 mol L^{-1}) and pyrolysis at 973 K under N_2 , was also used in the methanation of bio-syngas [85]. Excellent results were obtained with improved CO conversion (up to 97%) upon increasing the Ru loading, and selectivity to CH_4 of 84% and 92% using a $\text{H}_2/(\text{CO} + \text{CO}_2)$ ratio of 2 and 4, respectively. The large specific surface area (ca. 757 $\text{m}^2 \text{g}^{-1}$) of activated biochar favored a higher dispersion of Ru nanoparticles (>70%) compared to other usual support such as Al_2O_3 (43%) and SiO_2 (17%), which may account for the effective catalytic performance [86]. Later on, the same authors observed a high CH_4 selectivity (98%) and a CO conversion of 100% and also an excellent stability for a period of at least 100 h on stream over the Ru activated biochar catalysts [87].

4.6.2. Isomerization Reactions

The monomeric aldoses from hydrolysis of lignocellulosic biomass (e.g., glucose and xylose) can be isomerized into ketoses (fructose and xylulose, respectively) by isomerization reactions. These compounds, with high reactive carbonyl functional groups (C=O), can be more easily upgraded due to their lower activation barrier than the aldoses precursors with stable ring structures [88]. These isomerization reactions generally involve the participation of Lewis acid or Brønsted base sites at 90–110 °C that catalyze the critical hydrogen transfer steps.

Glucose isomerization is a promising reaction pathway for the synthesis of fructose, the most important precursor for the production of key platform molecule HMF. In this sense, recently, Yang et al., explored an Sn-BCH from wood waste as catalyst for the isomerization of glucose, showing that both the biochar porosity and acid/base properties derived from Sn/biochar chemical interactions contributed to enhance the fructose yield (max. 15.2 mol %) [89]. Al-biochar was also devised to serve as a novel heterogeneous catalyst for isomerization of glucose. Yu et al., reached a remarkable yield of 21.5 mol % fructose (selectivity 73.8 mol %) after only 5 min heating at 160 °C in acetone/H₂O medium. They found that the aluminum species (Al₂O₃, Al(OH)₃, AlO(OH) and Al–O–C moieties) were the major contributor of the catalytic activity via the Lewis acid-driven mechanism [90]. Similar conclusions were obtained from a study performed by Sheng et al., in which a cellulose derived biochar supported Al catalyst with carbonaceous microspheres (evidenced by SEM) led to fructose selectivity of 77.8 mol % [91].

In summary, the use of M-BCH catalysts in biorefinery processes is quite well reported highlighting the potential of biochar as an alternative to the conventional catalysts in biorefineries for a broad variety of reactions. Generally, in these reactions, it is worth noting an effect of the biochar support, in which the oxygen-containing functional groups or oxygen vacancies plays an important role on anchoring of metal particles, contributing positively for the metal deposition, control of particle size, and interaction metal-support.

Moreover, these works also pointed out that the catalytic properties of biochar can be readily adjusted by changing the atmosphere under which pyrolysis is performed and the engineered biochar could potentially be an alternative to the conventional catalysts applied for the synthesis of renewable fuels and chemicals.

5. Electrochemical Applications

The ever-increasing global energy demand and the incessant consumption of fossil fuel sources has posed serious challenges to energy security, pollution, and climate change but has also had a tremendous impact on our planet's ecosystems and biodiversity leading to the urgent development of green, renewable, and highly efficient energy storage and conversion technologies. Presently, solar cells, fuel cells, water splitting, lithium-ion batteries, and supercapacitors are probably the most promising alternatives for a clean energy supply. However, these devices rely on a series of electrochemical reactions (hydrogen evolution (HER) and oxygen evolution (OER) and reduction reactions (ORR)) where electrode materials play a central role. Therefore, the development of novel high performance, low-cost, industrially and economically attractive, and scalable materials is of utmost importance.

In this section, we will focus on the application of M-BCH materials for supercapacitors and the demanding oxygen and hydrogen reactions associated with fuels cells, batteries, and water splitting devices.

5.1. Supercapacitors

At the end of this section, Table 6 summarizes all the M-BCH supercapacitor materials (biomass feedstocks, catalyst preparations, surface areas, and electrochemical performances) described below.

Table 6. Metal-supported biochar-based nanocomposites for supercapacitor electrodes.

Nanomaterial Properties				Electrochemical Supercapacitor Metrics				Ref.
Biochar Feedstock ^a	Synthesis ^b	Metal	Biochar Nanocomposite	Surface Area ^c (m ² g ⁻¹)	Test Cell Type/Electrolyte	Capacitance ^d (F g ⁻¹)/Current Density (A g ⁻¹)	Energy Density ^e (Wh kg ⁻¹)/Power Density (W kg ⁻¹)	
Agaric	Immersion in NaCl + Mn(AcO) ₂ ·4H ₂ O solution. Heating at 60 °C for 6 h. Carbonization in Ar atmosphere at 800 °C for 12 h	Mn	Hierarchical porous MnO/biocomposite	139.6	3-electrode/3 M KOH _(aq) solution	402 ⁽¹⁾ /2	-	[92]
	Immersion in Mn(AcO) ₂ ·4H ₂ O solution. Heating at 60 °C for 6 h. Carbonization in N ₂ atmosphere at 800 °C for 2 h with heating rate of 5 °C min ⁻¹	Mn	Porous MnO/biocomposite	≈133	Asymmetric 2-electrode/3 M KOH _(aq) solution	101/1	35.9/800	[93]
Bambo leaves	Carbonization at 600 °C in N ₂ atmosphere for 2 h with heating rate of 1 °C min ⁻¹ . Hydrothermal treatment of carbon and Cu(OAc) ₂ at 180 °C for 24 h	Cu	CuO/Cu ₂ O/hierarchical porous biocomposite	301.85	3-electrode/3 M KOH _(aq) solution	147/1	-	[133]
	Carbonization at 600 °C in N ₂ atmosphere for 2 h with heating rate of 1 °C min ⁻¹ . Hydrothermal treatment of carbon and Mn(OAc) ₂ ·4H ₂ O at 180 °C for 24 h	Mn	MnSi/heteroatom-doped porous biocomposite	300.3	Asymmetric 2-electrode/Polyvinyl alcohol (PVA)/KOH gel	54.6 ⁽²⁾ /12 ⁽³⁾	24.6/604.8	[118]
	Carbonization at 600 °C in N ₂ atmosphere for 2 h with heating rate of 1 °C min ⁻¹ . Hydrothermal treatment of carbon and Zn(OAc) ₂ ·2H ₂ O at 180 °C for 24 h	Zn	Zn ₄ Si ₂ O ₇ (OH) ₂ /3D N, S-enriched biocomposite	475		124 ⁽²⁾ /10 ⁽³⁾	0.44 ⁽⁴⁾ /40 ⁽⁵⁾	[132]
Banana peel	Hydrothermal treatment at 120 °C for 24 h. Carbonization at 500 °C in Ar flow for 2 h. Immersion in SnCl ₂ 2H ₂ O water/EtOH solution. Addition of ammonia solution (keeping pH = 8) and stirring for 4 h. Annealing at 200 °C for 1 h	Sn	SnO ₂ /biochar	376.2	3-electrode/1 M H ₂ SO _{4(aq)} solution	476/0.15	-	[135]
	Immersion in 2 mol L ⁻¹ KOH _(aq) solution for 24 h. Carbonization at 900 °C in Ar atmosphere for 2 h. Hydrothermal treatment of carbon, urea and KMnO ₄ at 120 °C for 12 h	Mn	MnO ₂ /3D porous biocomposite	-	3-electrode/1 M Na ₂ SO _{4(aq)} solution	70/10	-	[124]

Table 6. Cont.

Nanomaterial Properties				Electrochemical Supercapacitor Metrics				Ref.
Biochar Feedstock ^a	Synthesis ^b	Metal	Biochar Nanocomposite	Surface Area ^c (m ² g ⁻¹)	Test Cell Type/Electrolyte	Capacitance ^d (F g ⁻¹)/Current Density (A g ⁻¹)	Energy Density ^e (Wh kg ⁻¹)/Power Density (W kg ⁻¹)	
Cellulose	Immersion in Ni(NO ₃) _{2(aq)} solution. Carbonization at 500 °C for 1 h. Electrophoretic deposition on Ni foils using Pt wire anode, with isopropanol electrolyte, at 40 V for 1 h	Ni	Biochar wrapped Ni/NiO nanobricks	198	3-electrode/ 1 M KOH _(aq) solution	640/5	-	[95]
					Asymmetric 2-electrode	-	81/6000	
Cladophora Glomerata	Immersion in 6 mol L ⁻¹ KOH _(aq) solution at 80 °C (reflux) for 6 h. Carbonization at 700 °C for 2 h. Reflux with H ₂ SO ₄ and HNO ₃ at 80 °C for 6 h. Hydrothermal treatment with NH ₄ OH and FeSO ₄ ·7H ₂ O at 120 °C for 15 h	Fe	Fe NPs/interconnected 3D pore network biochar	957	Asymmetric 2-electrode/3 M KCl _(aq) solution	368.9/1	16.4/25,600	[127]
Cornstalks	Mixing with KOH and KMnO ₄ . Carbonization at 800 °C for 2 h under N ₂ atmosphere	Mo	MoS ₂ nanoflowers/biocrarbon	930	Symmetric 2-electrode/6 M KOH _(aq) solution	38.1/50.0	12.1/37,775	[94]
Cotton	Carbonization at 900 °C for 2 h under N ₂ atmosphere. Immersion in Co(NO ₃) _{2(aq)} solution for 12 h. Calcination at 300 °C for 3 h in air	Co	Co ₃ O ₄ /hollow-biocrarbon-fiber	177	Asymmetric 2-electrode/6 M KOH _(aq) solution	77.8/1	15.41/7500	[130]
						Mixing of CoCl ₂ ·6H ₂ O with urea in water at 90 °C (reflux) for 3 h. Ultrasonic dispersion in this solution. Carbonization at 350 °C for 4 h with heating rate of 3 °C min ⁻¹	Co	
Crab waste	Carbonization at 500 °C for 1 h in N ₂ atmosphere. Immersion in KOH _(aq) solution for 24 h. Activation at 700 °C for 2 h in N ₂ atmosphere. Ultrasonic dispersion in CoCl ₂ ·6H ₂ O and FeCl ₃ ·6H ₂ O aqueous solution. Addition of NaOH to fix pH into 11. Heat treatment at 120 °C for 12 h	Co	CoFe ₂ O ₄ /biocrarbon	1602 ⁽⁶⁾	3-electrode/6 M KOH _(aq) solution	437.4/10	~600/1	[129]

Table 6. Cont.

Nanomaterial Properties				Electrochemical Supercapacitor Metrics				Ref.
Biochar Feedstock ^a	Synthesis ^b	Metal	Biochar Nanocomposite	Surface Area ^c (m ² g ⁻¹)	Test Cell Type/Electrolyte	Capacitance ^d (F g ⁻¹)/Current Density (A g ⁻¹)	Energy Density ^e (Wh kg ⁻¹)/Power Density (W kg ⁻¹)	
Dairy manure/sewage sludge	Carbonization at 600 °C for 4 h under <0.5% O ₂ condition. Immersion in Ni(NO ₃) _{2(aq)} solution for 24 h. Microwave oxidative heating under 1000 W power for 30 min	Ni	NiO-NiOOH/biochar	≈30	3-electrode/0.5 M KOH _(aq) solution	123 ⁽⁷⁾ 100 ⁽⁸⁾	-	[102]
Durian rind	Ultrasonic dispersion in FeCl ₃ ·6H ₂ O, HNO ₃ and KMnO ₄ aqueous solution for 5 h at 40 °C. Drying at vacuum for 5 days at 70 °C. Carbonization at 800 °C for 25 min under vacuum condition. Ultrasonic dispersion in 1 mol L ⁻¹ HCl solution along with aniline monomer (cooled by ice batch). Slow addition of 0.125 M (NH ₄) ₂ S ₂ O _{8(aq)} solution and stirring (2 h) for aniline polymerization	Fe	Fe ₃ O ₄ /biochar/polyaniline	510.5	3-electrode/0.1 M KNO _{3(aq)} solution	615 ⁽⁹⁾	76.88 ⁽⁹⁾	[98]
	Idem to the immediately above-described protocol, except for the monomer: instead of aniline, pyrrole	Fe	Fe ₃ O ₄ /biochar/polypyrrole	474.8		572 ⁽⁹⁾	71.50 ⁽⁹⁾	[99]
Fresh bamboo strip	Carbonization at 650 °C for 2 h in N ₂ atmosphere with heating rate of 3 °C min ⁻¹ . "In situ" growth of CoZn-ZIF-8: heating at 120 °C for 12 h of M(AcO) ₂ ·x H ₂ O (M = Zn and Co), 2-MeIm with carbon mixture in aqueous solution. Carbonization at 900 °C for 3 h in N ₂ atmosphere	Co and Zn	CoZn/biocarbon	-	3-electrode/6 M KOH _(aq) solution	757.8 ⁽¹⁰⁾	-	[131]
Hemp stem	Carbonization at 600 °C for 2 h in N ₂ flow with heating rate of 10 °C min ⁻¹ . Heating in steam atmosphere at 800 °C for 2 h. Immersion in KMnO ₄ and MnSO ₄ for 30 min. Hydrothermal treatment at 140 °C for 24 h	Mn	MnO ₂ nanowire/biocarbon	438	3-electrode/1 M Na ₂ SO _{4(aq)} solution	≈299/30	-	[123]
					Asymmetric 2-electrode/1 M Na ₂ SO _{4(aq)} solution	-	31.0/14,800	

Table 6. Cont.

Nanomaterial Properties				Electrochemical Supercapacitor Metrics				Ref.
Biochar Feedstock ^a	Synthesis ^b	Metal	Biochar Nanocomposite	Surface Area ^c (m ² g ⁻¹)	Test Cell Type/Electrolyte	Capacitance ^d (F g ⁻¹)/Current Density (A g ⁻¹)	Energy Density ^e (Wh kg ⁻¹)/Power Density (W kg ⁻¹)	
Infested ash tree residue	Carbonization at 700 °C in inert gas flow with heating rate of 0.5 °C min ⁻¹ . Immersion in Ag ₂ SO ₄ /HNO ₃ aqueous solution for 24 h	Ag	Ag/Biochar	335	Symmetric 2-electrode/2 M LiN(SO ₂ CF ₃) _{2(aq)} solution	489 ⁽¹¹⁾	5.8/619	[136]
Luffa plant	Heat pre-treatment at 200 °C for 6–8 h in vacuum. Mixing/milling with K ₂ FeO ₄ and dicyandiamide. Carbonization at 1000 °C for 2 h in N ₂ with heating rate of 10 °C min ⁻¹ . Ultrasonic dispersion (for 30 min) in EtOH/ethylene glycol solution with Ni(AcO) ₂ ·4H ₂ O and Mn(AcO) ₂ ·4H ₂ O. Solvothermal treatment at 185 °C for 20 h	Ni and Mn	NiMn ₂ O ₄ nanocrystals/3D porous graphitized biocarbon	832	Asymmetric 2-electrode/6 M KOH _(aq) solution	100.6/8	45.25/11,380	[110]
Natural metasequoia wood	Immersion in ZnCl _{2(aq)} solution under vacuum for 24 h. Carbonization at 750 °C for 3 h. Immersion in Co(NO ₃) ₂ ·6H ₂ O Ni(NO ₃) ₂ ·6H ₂ O aqueous solution. Hydrothermal treatment at 140 °C for 12 h. Immersion in Na ₂ S·9H ₂ O _(aq) solution. Hydrothermal treatment at 160 °C for 12 h	Ni and Co	NiCo ₂ S ₄ nanowires/3D biocarbon	-	3-electrode/6 M KOH _(aq) solution	281.8/10	-	[117]
Natural wood slice	Multi-step carbonization: (1) T = 500 °C for 1 h with heating rate of 5 °C·min ⁻¹ , (2) T = 1000 °C for 2 h with heating rate of 5 °C·min ⁻¹ , and (3) T = 500 °C with cooling rate of 5 °C·min ⁻¹ . Immersion in KMnO _{4(aq)} solution. Heating at 60 °C for 12 h	Mn	Core-shell MnO ₂ nanosheets/biochar	683 ⁽⁶⁾	3-electrode/1 M Na ₂ SO _{4(aq)} solution	43/10	-	[121]
Peanut shells	Mixing with KOH. Carbonization at 800 °C for 1 h in vacuum. Dispersion in EtOH/ethylene glycol solution for 4 h. Hydrothermal treatment at 80 °C for 12 h in presence of Ni foam.	Ni	Biocarbon hooks on Ni foam	1279 ⁽⁶⁾	3-electrode/1 M Li ₂ SO _{4(aq)} solution	≈90/10	~12.2/4000	[106]

Table 6. Cont.

Nanomaterial Properties				Electrochemical Supercapacitor Metrics				Ref.
Biochar Feedstock ^a	Synthesis ^b	Metal	Biochar Nanocomposite	Surface Area ^c (m ² g ⁻¹)	Test Cell Type/Electrolyte	Capacitance ^d (F g ⁻¹)/Current Density (A g ⁻¹)	Energy Density ^e (Wh kg ⁻¹)/Power Density (W kg ⁻¹)	
Pinecone flowers	Carbonization at 600 °C for 3 h in N ₂ atmosphere with heating rate of 10 °C min ⁻¹ . Immersion in KOH _(aq) solution. Activation at 800 °C for 1.5 h in N ₂ . Impregnation with H ₃ PMo ₁₂ O ₄₀ in aqueous solution for 1 h	Mo	Polyoxometalate/biochar	510	3-electrode/1 M H ₂ SO _{4(aq)} solution	≈850 ⁽¹²⁾	-	[134]
	Activation in KOH _(aq) solution (reflux conditions) for 10 h. Carbonization at 900 °C for 2 h in Ar flow with heating rate of 5 °C min ⁻¹ . Ultrasonic dispersion in ethanol for 30 min. Mixing with Ni(NO ₃) ₂ ·6H ₂ O _(aq) solution, hexamethylenetetramine and ammonia via stirring for 1 h. Solvothermal treatment at 90 °C for 10 h	Ni	Ni(OH) ₂ nanosheets/honeycomb-like porous biocarbon	80.3	3-electrode/1 M KOH _(aq) solution	565.71/10	-	[105]
Pomelo peel	Activation in 1 M KOH _(aq) solution for 12 h. Carbonization at 700 °C for 2 h in N ₂ atmosphere with heating rate of 5 °C min ⁻¹ . Hydrothermal treatment with Co(NO ₃) ₂ ·6H ₂ O, Ni(NO ₃) ₂ ·6H ₂ O and urea at 120 °C for 16 h	Ni and Co	NiCo ₂ O ₄ nanosheets/honeycomb-like porous biocarbon	-	Asymmetric 2-electrode/2 M KOH _(aq) solution	≈35/10	14.9/5346	[112]
	Hydrothermal treatment at 180 °C for 6.5 h. Mixing with Co(NO ₃) ₂ ·6H ₂ O, Ni(NO ₃) ₂ ·6H ₂ O, Al(NO ₃) ₃ ·9H ₂ O and urea in MeOH solution. Solvothermal treatment at 150 °C for 12 h	Ni, Co and Al	CoNiAl-layered double hydroxide/biocarbon aerogel	-	3-electrode/2 M KOH _(aq) solution	902/10	-	[111]

Table 6. Cont.

Nanomaterial Properties				Electrochemical Supercapacitor Metrics				Ref.
Biochar Feedstock ^a	Synthesis ^b	Metal	Biochar Nanocomposite	Surface Area ^c (m ² g ⁻¹)	Test Cell Type/Electrolyte	Capacitance ^d (F g ⁻¹)/Current Density (A g ⁻¹)	Energy Density ^e (Wh kg ⁻¹)/Power Density (W kg ⁻¹)	
Poplar catkins	Carbonization at 800 °C for 2 h in Ar atmosphere with heating rate of 2 °C min ⁻¹ . Ultrasonic dispersion in Tris-HCl (pH = 8.5, 10 mM) buffer solution for 30 min. Addition of dopamine while stirring for 24 h to self-polymerization. Mixing with Ni(NO ₃) ₂ , Co(NO ₃) ₂ , hexamethylenetetramine, and citric acid trisodium salt in aqueous solution. Hydrothermal treatment at 120 °C for 6 h. Calcination at 300 °C for 2 h in air with heating rate of 1 °C min ⁻¹	Ni and Co	NiCo ₂ O ₄ nanosheets/biocomposite microsheets	143.21	Asymmetric 2-electrode/6 M KOH _(aq) solution	96.0 (13)/10	21.7/8218.9	[113]
Rice husk charcoal	Activation in KOH _(aq) solution at 110 °C for 1 h. Annealing at 850 °C for 1 h in CO ₂ atmosphere. Mixing with Ni(NO ₃) ₂ ·6H ₂ O and thiourea in aqueous solution. Immersion of Ni foam. Hydrothermal treatment at 120 °C for 16 h	Ni	Ni ₃ S ₂ /porous biocomposite	-		89.3/2	27.9/1500	[107]
Seeds of Toona sinensis	Activation in KOH _(aq) solution for 30 min. Carbonization at 800 °C for 2 h in Ar atmosphere. Mixing with Co(NO ₃) ₂ ·6H ₂ O, Ni(NO ₃) ₂ ·6H ₂ O and hexamethylenetetramine in aqueous solution. Hydrothermal treatment at 100 °C for 9 h	Ni and Co	Ni-Co layered double hydroxide/biocomposite	111.21		29.6/10	23.5/959.7	[116]
Sorghum stalk	Carbonization at 550 °C for 0.5 h in N ₂ atmosphere. Activation in KOH _(aq) solution at 700 °C for 1 h. Ultrasonic dispersion in Ni(NO ₃) ₂ ·6H ₂ O _(aq) solution. Addition of urea solution. Microwave deposition at 700 W for 3 min	Ni	Ni(OH) ₂ /biocomposite	-		3-electrode/3 M KOH _(aq) solution	490.1/20	12.3/6314.4

Table 6. Cont.

Nanomaterial Properties				Electrochemical Supercapacitor Metrics				Ref.
Biochar Feedstock ^a	Synthesis ^b	Metal	Biochar Nanocomposite	Surface Area ^c (m ² g ⁻¹)	Test Cell Type/Electrolyte	Capacitance ^d (F g ⁻¹)/Current Density (A g ⁻¹)	Energy Density ^e (Wh kg ⁻¹)/Power Density (W kg ⁻¹)	
Sugarcane bagasse	Activation with KOH in abs. EtOH at 60 °C until EtOH evaporation. Carbonization at 800 °C for 2 h in N ₂ atmosphere with heating rate of 10 °C min ⁻¹ . Treatment with KMnO _{4(aq)} solution at 70 °C until color change	Mn	MnO ₂ /biocarbon	471.33	Asymmetric 2-electrode/1 M KOH _(aq) solution	51.3/10	25.9 ⁽¹⁴⁾ /750	[122]
	Activation with KOH in abs. EtOH at 60 °C until EtOH evaporation. Carbonization at 800 °C for 2 h in N ₂ atmosphere with heating rate of 10 °C min ⁻¹ . Mixing with FeCl ₃ ·6H ₂ O _(aq) and FeCl ₂ ·4H ₂ O _(aq) solution. Addition of NaOH _(aq) solution until pH = 11. Heating at 90 °C for 1 h	Fe	Fe ₃ O ₄ /activated biocarbon	490.93		35.6/10	29.1 ⁽¹⁴⁾ /800	[128]
Typha domingensis	Addition to a Co(NO ₃) ₂ ·6H ₂ O and Ni(NO ₃) ₂ ·6H ₂ O aqueous solution. Hydrothermal treatment at 200 °C for 12 h. Carbonization at 700 °C for 3 h in Ar atmosphere	Ni and Co	Ni-Co oxides NPs/biocarbon fiber	≈110	Asymmetric 2-electrode/6 M KOH _(aq) solution	≈92/25	≈30/25,600	[96]
	Activation in KOH _(aq) solution at 80 °C for 2 h. Mixing with water-dispersed graphene oxide. Carbonization at 700 °C for 3 h. Ultrasonic dispersion in water. Mixing with Ni(NO ₃) ₂ ·6H ₂ O, Al(NO ₃) ₃ ·9H ₂ O and urea. Hydrothermal treatment at 95 °C for 24 h	Ni and Al	Ni-Al layered double hydroxide nanosheets/biocarbon-graphene oxide	≈390		144/30	≈100/28,800	[109]
Walnut shells	Activation in KOH _(aq) solution. Carbonization at 600 °C for 2 h in N ₂ atmosphere with heating rate of 5 °C min ⁻¹ . Mixing with Ni(NO ₃) ₂ ·6H ₂ O, hexamethylenetetramine and thiourea in aqueous solution. Hydrothermal treatment at 180 °C for 8 h	Ni	NiS NPs/porous biocarbon	-	3-electrode/2 M KOH _(aq) solution	350/10	-	[108]

Table 6. Cont.

Nanomaterial Properties				Electrochemical Supercapacitor Metrics				Ref.
Biochar Feedstock ^a	Synthesis ^b	Metal	Biochar Nanocomposite	Surface Area ^c (m ² g ⁻¹)	Test Cell Type/Electrolyte	Capacitance ^d (F g ⁻¹)/Current Density (A g ⁻¹)	Energy Density ^e (Wh kg ⁻¹)/Power Density (W kg ⁻¹)	
Wasted litchi shell	Mixing with thiourea and (NH ₄) ₆ Mo ₇ O ₂₄ aqueous solution. Hydrothermal treatment at 200 °C for 1 h. Carbonization at 1000 °C for 3 h in N ₂ atmosphere	Mn	MnO nanosheets/porous biocarbon	326	Symmetric 2-electrode/1 M LiPF ₆ in ethylene carbonate/diethyl carbonate/dimethyl carbonate solution	250/20	-	[100]
Watermelon	Hydrothermal treatment at 180 °C for 12 h. Mixing with KMnO ₄ and Na ₂ S ₂ O ₃ ·5H ₂ O in aqueous solution. Hydrothermal treatment at 120 °C for 12 h. Carbonization at 350 °C for 2 h in N ₂ atmosphere	Mn	MnO ₂ /biocarbon aerogel	Not specified	3-electrode/6 M KOH _(aq) solution	49.3/0.5	-	[119]
Water caltrop	Carbonization at 800 °C for 5 h in N ₂ atmosphere. Mixing with KOH. Carbonization at 850 °C for 2 h in N ₂ atmosphere. Ultrasonic dispersion in Co(NO ₃) ₂ ·6H ₂ O, Ni(NO ₃) ₂ ·6H ₂ O and polyvinylpyrrolidone MeOH solution. Solvothermal treatment at 180 °C for 12 h	Ni and Co	Ni-Co layered double hydroxide NPs/porous biocarbon	136.6	Asymmetric 2-electrode/6 M KOH _(aq) solution	78/10	29/14,736	[115]
Wheat flour	Dispersion in KOH and urea aqueous solution. Carbonization at 800 °C for 1 h in N ₂ flux. Mixing with Fe(NO ₃) ₃ ·9H ₂ O, Na ₂ SO ₄ in water. Hydrothermal treatment at 120 °C for 9 h	Fe	Fe ₂ O ₃ nanorods/porous biocarbon	700	Asymmetric 2-electrode/1 M Li ₂ SO _{4(aq)} solution	≈180/10	102/9300	[126]
Wheat straw	Immersion in KOH _(aq) solution for 8 h. Carbonization at 800 °C for 2 h in Ar atmosphere. Mixing with Fe(NO ₃) ₃ ·9H ₂ O in EtOH at 50 °C until EtOH evaporation. Calcination at 200 °C for 5 h in air	Fe	Ultrathin Fe ₂ O ₃ film/porous biocarbon	775.8	Asymmetric 2-electrode/1 M KOH _(aq) solution	108/30	20.8/20,650	[125]

Table 6. Cont.

Nanomaterial Properties				Electrochemical Supercapacitor Metrics				Ref.
Biochar Feedstock ^a	Synthesis ^b	Metal	Biochar Nanocomposite	Surface Area ^c (m ² g ⁻¹)	Test Cell Type/Electrolyte	Capacitance ^d (F g ⁻¹)/Current Density (A g ⁻¹)	Energy Density ^e (Wh kg ⁻¹)/Power Density (W kg ⁻¹)	
Willow catkin	Immersion in KOH _(aq) solution at 100 °C until water evaporation. Multi-step carbonization: (1) T = 400 °C for 3 h with heating rate of 5 °C·min ⁻¹ , and (2) T = 850 °C for 1 h with heating rate of 10 °C·min ⁻¹ . Mixing with KMnO _{4(aq)} solution. Hydrothermal treatment at 120 °C for 1 h with heating rate of 2 °C min ⁻¹	Mn	MnO ₂ nanoplates/cross-linked biocarbon nanosheets	234	Asymmetric 2-electrode/1 M Na ₂ SO _{4(aq)} solution	32.1/5	12.1/3570.5	[120]
	Carbonization at 500 °C for 4 h in Ar atmosphere. Refluxing in HNO _{3(aq)} solution at 50 °C for 5 h. Dispersion in water and mixing with Ni(NO ₃) ₂ ·6H ₂ O, NH ₄ F and urea. Hydrothermal at 150 °C for 6 h	Ni	Ni(OH) ₂ nanosheet arrays/hollow biocarbon microtube	155.7	Asymmetric 2-electrode/6 M KOH _(aq) solution	53/20	16.6/15,000	[104]
	Carbonization at 1000 °C in Ar atmosphere. Mixing with Ni(AcO) ₂ ·4H ₂ O, Co(AcO) ₂ ·4H ₂ O and thiourea in ethylene glycol. Solvothermal at 180 °C for 8 h	Ni and Co	Ni-Co sulfides NPs/biocarbon microtubes	17.3		57/20	17.7/17,200	[114]
Yellow soybean sprouts	Carbonization at 400 °C in N ₂ flow. Immersion in Ce(NO ₃) _{3(aq)} solution. Addition of KOH. Hydrothermal treatment at 100 °C for 12 h. Carbonization at 800 °C for 2 h in N ₂ flow	Ce	CeO ₂ /biocarbon	859	Symmetric 2-electrode/poly(vinyl alcohol)–KOH gel electrolyte	≈85/3	≈7.5/1200	[101]

^a Alphabetically-ordered authors' biomass precursor denominations. ^b Synthetic protocols are summarized, not including simple drying, washing, and separation (filtering, centrifuging, etc.) steps. ^c Specific surface area calculated from N₂-adsorption isotherm data using the Brunauer–Emmett–Teller (BET) method. ^d Specific capacitance value measured at the maximum tested current density. ^e Energy density value measured at the maximum tested power density. ⁽¹⁾ Capacitance expressed in mAh g⁻¹; ⁽²⁾ Capacitance expressed in mF cm⁻²; ⁽³⁾ Current density expressed in mA cm⁻²; ⁽⁴⁾ Energy density expressed in Wh m⁻²; ⁽⁵⁾ Power density expressed in W m⁻²; ⁽⁶⁾ Specific surface area value of the biocarbon—not including metal functionalization; ⁽⁷⁾ Specific capacitance (F g⁻¹) at scan rate of 5 mV s⁻¹ of nanocomposite electrode derived from dairy manure; ⁽⁸⁾ Specific capacitance (F g⁻¹) at scan rate of 5 mV s⁻¹ of nanocomposite electrode derived from sewage sludge; ⁽⁹⁾ Specific capacitance (F g⁻¹) or energy density (Wh kg⁻¹) measured at scan rate of 10 mV s⁻¹; ⁽¹⁰⁾ Specific capacitance (F g⁻¹) measured at scan rate of 5 mV s⁻¹; ⁽¹¹⁾ Specific capacitance (F g⁻¹) measured at scan rate of 5 V s⁻¹; ⁽¹²⁾ Areal capacitance (mF cm⁻²) measured at scan rate of 200 mV s⁻¹; ⁽¹³⁾ Capacitance expressed in C g⁻¹; ⁽¹⁴⁾ Maximum energy density value, i.e., achieved at the minimum tested power density.

Pre-activated M-BCH applied as electrode materials in supercapacitors are presented in the first place. Zhang et al. [92,93] prepared several MnO-containing biocarbon nanocomposites via impregnation of agaric biomass with $\text{Mn}(\text{AcO})_2$ and subsequent carbonization. In the first work [92], the authors utilized NaCl to form a molten-salt mixture during the heat treatment resulting in the generation of macropores and mesopores within the agaric-derived carbon matrix. This fact propitiated a specific capacitance (C_{sp}) of 508 F g^{-1} at a current density of 20 mA cm^{-2} and 94% capacity retention after 5000 cycles (at 20 mA cm^{-2}). In the second article [93], the obtained MnO/porous carbon used as cathode in an asymmetric supercapacitor system delivered 637 F g^{-1} at 3 mA cm^{-2} , with significant cycling stability: 91% capacity retention over 5000 cycles (at 10 mA cm^{-2}). In 2020, another work [94] reported the preparation of a MnO/biomass-derived carbon, but in this case, the feedstock was wasted litchi shell and the MnO precursor, KMnO_4 . With this material, the authors assembled a symmetric supercapacitor device that developed 162.7 F g^{-1} of C_{sp} at a current density of 0.5 A g^{-1} and 57.7 Wh kg^{-1} of energy density at a power density of 400 W kg^{-1} .

Regarding M-BCH supercapacitors involving Ni compounds, two works were reported. On one hand, Paravannoor [95] described the fabrication of a Ni/NiO nanobrick/BCH nanocomposite via nickel nitrate-cellulose mix carbonization followed by its electrophoretic deposition on Ni foil support. Remarkably, this material achieved up to 1058 F g^{-1} of specific capacitance in single-electrode test, and 81 Wh kg^{-1} and 6 kW kg^{-1} of energy and power density, respectively, in asymmetric setup. On the other side, a bimetallic Ni-Co oxide/*Typha domingensis*-derived biocarbon was tested as supercapacitor electrode by Golmohammadi and Amiri [96]. This nanocomposite reached—in charge–discharge experiments— 1770 F g^{-1} of specific capacitance at current density of 1.0 A g^{-1} , retaining 60% of it when the current density was increased to 66 A g^{-1} . Besides, it showed a good cycling stability ($\approx 92\%$ retention after 5000 cycles), and an energy density of 101 Wh kg^{-1} at 25.6 kW kg^{-1} acting as positive electrode within a hybrid supercapacitor device employing Vulcan XC-72R carbon black as negative electrode. Another study involving cobalt was reported by Shi et al. [97] in 2018. In this case, Co is present in form of Co_3O_4 generating a sandwich Co_3O_4 /carbon fiber/ Co_3O_4 nanocomposite being prepared from cotton. This material exhibited a specific capacitance of 892 F g^{-1} (at 0.5 A g^{-1}) and 88% capacitance retention over 6000 cycles.

Focusing on pre-activated Fe/BCH supercapacitors, a pair of publications by Thines et al. [98,99] proposed the utilization of durian rind as precursor to obtaining similar magnetic biochars—(thanks to the formation of magnetite, Fe_3O_4) combined with ‘in situ’-polymerized polyaniline (PANI) [98] or polypyrrole (PPy) [99]. These related materials showed similar outcomes when were assessed for supercapacitor applications: Fe_3O_4 /carbon/PANI developed 615 F g^{-1} of specific capacitance (at 10 mV/s) and $\approx 77 \text{ Wh kg}^{-1}$ of energy density, whereas the Fe_3O_4 /carbon/PPy nanocomposite exhibited 572 F g^{-1} and $\approx 72 \text{ Wh kg}^{-1}$, respectively.

Then, cornstalks were chosen by Zhao et al. [100] as biocarbon precursors to prepare MoS_2/C nanocomposites via a first step of cornstalk impregnation with thiourea and ammonium molybdate followed by consecutive hydrothermal (at $200 \text{ }^\circ\text{C}$) and carbonization ($1000 \text{ }^\circ\text{C}$) steps. The authors tested different carbonization periods (1, 2, or 3 h), being the material produced with the shortest treatment the most active as supercapacitor anode (250 F g^{-1} of C_{sp} at 20 A g^{-1}) mainly due to its highest surface area. Lastly, a very recent article [101] reported the production of CeO_2 /biocarbon material from yellow soybean sprouts (biomass feedstock) and $\text{Ce}(\text{NO}_3)_3$ as cerium dioxide precursor. The nanocomposite carbonized at the highest temperature ($800 \text{ }^\circ\text{C}$) resulted in the most active material for supercapacitor application, presenting a maximum specific capacitance equal to 752 F g^{-1} and only 2.5% capacitance loss over 10,000 charge–discharge cycles. Additionally, this material delivered an energy density up to 25.5 Wh kg^{-1} when it was assembled in a symmetric supercapacitor system.

Henceforth, all the mentioned M-BCH supercapacitor electrode materials have been prepared by a post-carbonization metal functionalization strategy. The nickel-containing materials are preponderant among this class because up to 17 studies on biochar-based electrodes for supercapacitors, involving uniquely Ni or Ni combined with another metal, have been published since 2017. Focusing on biocarbons exclusively containing nickel, Wang et al. [102] employed two wastes (dairy manure and sewage sludge) to produce two different Ni-loaded biochars. For that, the authors carbonized the previously-dried precursors at 600 °C for 4 h, loaded the resulting carbonaceous materials in Ni(NO₃)₂ aqueous solution, and activated them via microwave (MW) oxidation. Thus, the microwave-treated dairy manure-derived biochar supercapacitor exhibited the highest specific capacitance, 123 F g⁻¹ at 5 mV/s, with less than 2% loss after 1000 charge–discharge cycles. More recently, in 2020, a Ni(OH)₂/sorghum stalk biomass carbon [103], synthesized via microwave deposition, was tested as supercapacitor electrode. Due to the uniformly microwave-deposited Ni(OH)₂ this material achieved specific capacitances of 889.2 and 490.1 F g⁻¹ at current densities of 2 and 20 A g⁻¹, respectively. Additionally, it preserved 95.9% of capacitance after 30,000 cycles at 20 A g⁻¹. Li et al. [104] also used nickel hydroxide to decorate biochar by growing β-Ni(OH)₂ nanosheets arrays on hollow microtubes derived from willow catkin. Then, they assembled an asymmetric supercapacitor using the Ni(OH)₂-containing nanocomposite as positive electrode and porous carbon microtubes as negative electrode reaching a remarkable energy density level of 37.8 W h kg⁻¹ at 750 W kg⁻¹. Another work involving Ni(OH)₂-decorated biocarbon [105] describes the obtention of ultrathin Ni(OH)₂ nanosheet arrays grafted honeycomb-like porous carbon. The biocarbon support was produced by carbonizing pinecone flowers previously activated with KOH, while the Ni(OH)₂ was synthesized from Ni nitrate via solvothermal reaction in presence of methenamine. The as-prepared nanocomposite showed an enhanced supercapacitor performance ($C_{sp} = \approx 916.4$ F/g at 1 A/g and significant stability) in comparison with the honeycomb-like porous carbon and the nickel hydroxide separately. In 2021, the assessment of a peanut shell-derived biocarbon deposited on a Ni foam [106] as working electrode in a three-electrode cell system reported maximum specific capacitances (at a scan rate of 10 mV s⁻¹) of 243 and 272 F g⁻¹ using KOH and Li₂SO₄ as electrolytes, respectively. Wang et al. [107] deposited a promising biocarbon/Ni₃S₂ nanocomposite on Ni foam as well. The authors activated a rice husk-derived charcoal with KOH and CO₂ and generated nickel sulfide hydrothermally from Ni nitrate and thiourea. This material prepared with the longest hydrothermal reaction time (16 h) reached the maximum energy density of 35.7 Wh Kg⁻¹, which was remained at 27.9 Wh Kg⁻¹ with a high-power density at 1500 W kg⁻¹ when was assembled in a C/Ni₃S₂//C asymmetric supercapacitor. This high performance was attributed to the well-developed porosity of the biocarbon, leading to a maximized electrolyte-Ni₃S₂ contact. Another work [108] involving a biocarbon/NiS nanocomposite studied the optimum conditions to produce uniformly dispersed NiS nanoparticles on a walnut shells-derived carbon. It was found that 8 h of hydrothermal synthesis at 180 °C resulted in the most active material, presenting a C_{sp} equal to 1688.5 F g⁻¹ (at $j = 1$ A g⁻¹) and significant cycling stability.

Apart from two works reporting post-carbonization functionalized biochar-based supercapacitor nanocomposites containing Ni/Al [109] and Ni/Mn [110], both produced from plants, *Luffa* and *Typha domingensis*, respectively, the combination Ni/Co is the clear protagonist. As an example, Figure 6 collects the synthetic protocols for several Ni/Co-BCH tested as electrode materials in supercapacitors. Thus, two studies including pomelo peel as precursor have been published [111,112]. The first of them [111] exposes the production of a carbon aerogel combined with a cobalt-nickel layered double hydroxide also involving aluminum (CoNiAl-LDH@CA). This nanocomposite was employed as supercapacitor electrode material showing significant specific capacitances of 1134 F g⁻¹ (at 1 A g⁻¹) and 902 F g⁻¹ (at 10 A g⁻¹) and admirable cycling stability with a virtually unaltered capacitance after 4000 cycles. The latter article [112] presents the growth of NiCo₂O₄ nanosheets on an interconnected honeycomb-like porous carbon. After the KOH activa-

tion and carbonization of the pomelo peels, the resulting biocarbon was loaded with Ni^{2+} and Co^{2+} ions and subsequently subjected to hydrothermal treatment. Then this material showed 1137.5 F g^{-1} (at 5 A g^{-1}) and retained 90.3% of its capacitance after 5000 cycles, and when it was tested in an asymmetric supercapacitor, using activated carbon as negative electrode, achieved an elevated energy density of $\approx 31 \text{ Wh kg}^{-1}$ (at 900 W kg^{-1}). In addition, the carbonization of catkins from diverse tree plants to produce Ni/Co-biocarbons for supercapacitors has been reported twice [113,114]. Thus, Nan et al. [113] decorated poplar catkins-derived C microsheets with NiCo_2O_4 and polydopamine (PD) (Figure 6a), testing an asymmetric supercapacitor system (positive electrode: $\text{NiCo}_2\text{O}_4/\text{PD}/\text{C}$ and negative electrode: PD/C) with excellent performance: 39.1 Wh kg^{-1} at the power density of 800 W kg^{-1} , high cycling stability with a 4.5% capacity loss after 5000 cycles, and a wide potential window of 0–1.6 V. The other work [114] reported the production of willow catkin-derived carbon microtubes with supported Ni-Co sulfides nanoparticles. By adjusting the Ni precursor/Co precursor molar ratios (in both cases the corresponding acetates), the authors controlled Ni/Co ratios in the resulting nanocomposites. They found that the Ni/Co ratio of 2 achieved the best overall performance, i.e., a pseudocapacitance = 1210 F g^{-1} at 0.5 A g^{-1} , rate capability = 83.8% (1014 F g^{-1} at 10 A g^{-1}), 5% capacity loss after 3000 charge–discharge cycles and a maximum energy density of 28.1 Wh kg^{-1} at 753 W kg^{-1} assembled in an asymmetric capacitor with activated carbon as negative electrode. Ouyang et al. [115] synthesized, via solvothermal reaction spherical, Ni-Co layered double hydroxide nanoparticles on a biocarbon support previously obtained from dry carbonization and KOH activation of water caltrop (Figure 6b). As in the previous case, the Ni/Co ratio of 2 was revealed as the more suitable to obtain highly active material electrode for supercapacitors. Thus, the synergy between the Ni-Co hydroxide and the carbon allowed this nanocomposite to develop an elevated C_{sp} of 2047 F g^{-1} at 1 A g^{-1} , while a hybrid supercapacitor system with this material as cathode achieved 139 F g^{-1} at 1 A g^{-1} , an energy density of 49 Wh kg^{-1} at 1 A g^{-1} , and 75.8% retention after 6000 cycles. Additionally, seeds of *Toona sinensis* (also known as Chinese mahogany) were used to generate a Ni-Co/biocarbon active material also including Ni-Co layered double hydroxide [116] with remarkable results derived from the high surface area ($1031.6 \text{ m}^2 \text{ g}^{-1}$) of its carbonaceous support. Thus, this nanocomposite reached 992.2 F g^{-1} of specific capacitance (at 1 A g^{-1}), and the corresponding asymmetric supercapacitor (using the carbon support as negative electrode) developed an energy density of 23.5 Wh kg^{-1} and a power density of 959.7 W kg^{-1} , working in a 1.5 V window. To finish the Ni-Co/BCH section, Chen et al. [117] presented 3D biomass carbons (derived from the KOH activation/carbonization of metasequoia wood) decorated with hydrothermally-synthesized NiCo_2S_4 nanowires. This material was assessed in a three-electrode cell system showing its highest specific capacitance of 765.8 F g^{-1} at 1 A g^{-1} in 6 M KOH electrolyte.

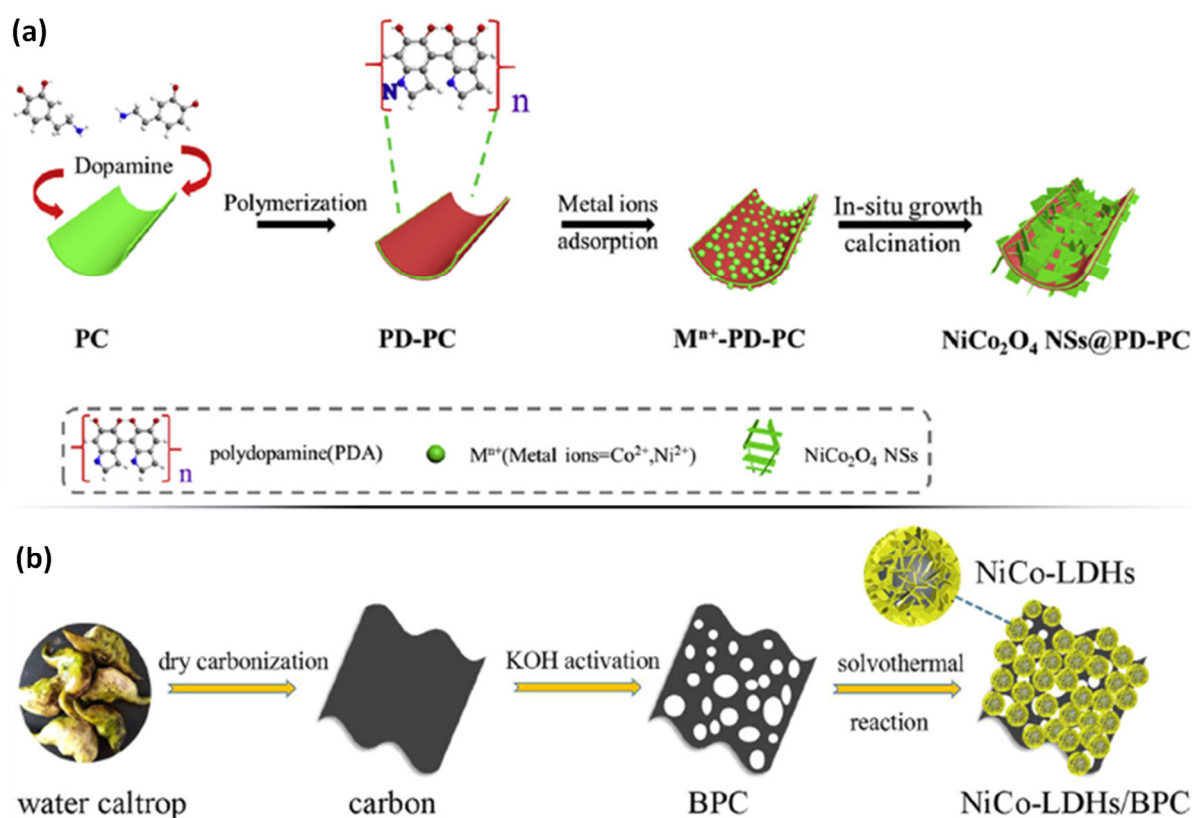


Figure 6. Selected examples of synthetic protocols for obtaining Ni-Co/biomass-derived-carbons via post-carbonization functionalization approach (a) [113] (b) [115]. Abbreviations: (a) PC: carbonized poplar catkins micro-hollow fibers, PD: polydopamine, and NSs: nanosheets; (b) BPC: biomass porous carbon, and LDHs: layered double hydroxides. Reprinted from [113], Copyright (2019), with permission from Elsevier (a). Reprinted from [115], Copyright (2020), with permission from Elsevier (b).

The second-largest group of post-activated M-BCH supercapacitor materials is constituted by those containing manganese. Except for one work involving manganese silicate [118], the remaining reported studies includes MnO_2 -decorated biocarbons. This work [118] proposes the carbonization of bamboo leaves to obtain a SiO_2 -C framework thanks to their inherent Si, followed by the loading of this support with Mn^{2+} ions and subsequent hydrothermal reaction to produce the $MnSiO_3$ /biocarbon nanocomposite. This material delivered a capacitance of 162.2 F g^{-1} (at 0.5 A g^{-1} of current density), and 85% capacitance retention over 10,000 cycles of cycling stability. In asymmetric supercapacitor device exhibited 438.5 mF cm^{-2} of capacity at 4 mA cm^{-2} , developing 24.6 Wh kg^{-1} and 604.8 W kg^{-1} of energy and power density, respectively. Focusing on the MnO_2 -containing biochars, the first publication [119] appeared in 2014 and it reports the preparation of a MnO_2 /watermelon soft tissue-derived carbon aerogel with a specific capacitance of 123.5 F g^{-1} . Then, Li et al. [120] grafted willow catkin-derived cross-linked carbon nanosheets with MnO_2 nanoplates using $KMnO_4$ as precursor. With this material, the authors assembled a hybrid supercapacitor that showed a remarkable electrochemical performance with an energy density of 23.6 Wh kg^{-1} at a power density = 188.8 W kg^{-1} working in a 1.9 V window with a minor loss of capacitance (1.4%) after 10,000 cycles at 1 A g^{-1} . Wan et al. [121] also employed $KMnO_4$ as MnO_2 precursor (and natural wood slices as carbon feedstock) to generate a core-shell MnO_2 /BCH nanocomposite exhibiting a C_{sp} of 101 F g^{-1} and a decent cyclic stability with 85% capacitance retention over 10,000 cycles. In another article [122], the carbonization and KOH activation of sugarcane bagasse biomass, along with again the utilization of potassium permanganate to produce MnO_2 , is

reported. The MnO_2 /biocarbon material prepared using a KMnO_4 /biocarbon mass ratio of 2 resulted in the best outcomes: capacitance above 400 F g^{-1} at 1 A g^{-1} in a three-electrode system, and elevated energy density of 25.9 Wh kg^{-1} at 750 W kg^{-1} within a wide potential window (1.5 V) and 94.2% capacitance retention over 2000 cycles in an asymmetric MnO_2 /biocarbon//biocarbon supercapacitor device. Regarding MnO_2 formation, Yang et al. [123] introduced a synthetic novelty using simultaneously KMnO_4 and MnSO_4 for the hydrothermal deposition of manganese oxide on a previously carbonized hemp stem biomass. Through this procedure the authors generated vertical MnO_2 nanowires on a 3D carbon network scaffold in an open pore system, exhibiting a C_{sp} value equal to 340 F g^{-1} at 1 A g^{-1} ; and forming a hybrid asymmetric supercapacitor system (utilizing the 3D carbon network without metal functionalization as anode) that delivers 14.8 kW kg^{-1} of power density with an energy density of 33.3 Wh kg^{-1} . Finally, in 2018, it was reported the use of banana peel, KMnO_4 and urea to produce MnO_2 /biomass-derived carbons [124] via a five-step methodology: KOH activation of banana peels, freeze drying, 2 h carbonization at $900 \text{ }^\circ\text{C}$, impregnation in KMnO_4 + urea solution, and final 12 h hydrothermal treatment at $120 \text{ }^\circ\text{C}$. The as-prepared electroactive material showed a specific capacitance of 139.6 F g^{-1} (at 300 mA g^{-1}), and 92.3% capacitance retention after 1000 cycles (at 1 A g^{-1}).

Apart from Ni- and Mn-post-activated biochar supercapacitors, biomass-derived carbons decorated with Fe-containing species attracted significant attention. Recently, two works reported the fabrication of Fe_2O_3 /biocarbon nanocomposites for supercapacitor applications from wheat, one of them by carbonizing wheat straw [125] and the other, wheat flour [126]. The former [125] proposed the formation of an ultrathin Fe_2O_3 film on the straw-derived carbon, generating a synergistic effect between both components that, along with a hierarchical porosity, led to a remarkable capacitance of 987.9 F g^{-1} (at 1 A g^{-1} of current density) and important cycling stability. Furthermore, the asymmetric supercapacitor assembled with this nanocomposite as anode material achieved large energy and power densities, 96.7 Wh kg^{-1} and 20.65 kW kg^{-1} , respectively. The latter article [126], published in 2020, reported the hydrothermal synthesis from $\text{Fe}(\text{NO}_3)_3 \cdot 9\text{H}_2\text{O}$ and Na_2SO_4 of porous Fe_2O_3 nanorods supported on wheat flour-derived carbon. This material showed an interesting electrochemical behavior as electrode, such as a C_{sp} value of 706 F g^{-1} , and assembled in a hybrid supercapacitor device, a specific capacitance of 212 F g^{-1} (at 1 A g^{-1}), maximum energy density of 117 Wh kg^{-1} (at 1.0 kW kg^{-1}), and only 5.8% capacitance loss over 5000 charge–discharge cycles. Two other studies involving monometallic Fe/biocarbon materials were recently published. On one hand, Pourhosseini et al. [127] explored the integration of iron oxide nanoparticles within an interconnected 3D pore network biochar derived from the macroalga *Cladophora glomerata*. The authors carried out a complete electrochemical evaluation of this nanocomposite (tagged as FCBC, Fe composite biochar) along with another two related materials: functional biochar (FBC)—macroalga-derived biochar but without Fe functionalization—and magnetic biochar (MBC)— Fe^{3+} -pre-loaded macroalga-derived biochar. Thus, two different asymmetric supercapacitors FBC//MBC and FBC//FCBC were tested, exhibiting (as can be verified in the CV, charge–discharge and Ragone plots of Figure 7) the FBC//FCBC combination a better performance but lower cyclability than the other one. On the other hand, Chen et al. [128] synthesized Fe_3O_4 /biocarbons via sugarcane bagasse KOH activation/carbonization and subsequent Fe post-activation. The nanocomposite involving a Fe_3O_4 /biocarbon mass ratio equal to 1 exhibited the largest specific capacitance, 342 F g^{-1} (at 1 A g^{-1}). Moreover, the hybrid system formed by this material and a MnO_2 /biocarbon nanocomposite as anode and cathode, respectively, delivered an energy density up to 29.1 Wh kg^{-1} , with 800 W kg^{-1} of power density, working in a 1.6 V potential range, and retained over 90% of its capacitance after 1000 cycles. Finally, Fu et al. [129] integrated Fe and Co within a crab waste-derived multi-hierarchical porous carbon by combining it with the pseudocapacitive active CoFe_2O_4 . For that, $\text{CoCl}_2 \cdot 6\text{H}_2\text{O}$ and $\text{FeCl}_3 \cdot 6\text{H}_2\text{O}$ were employed as CoFe_2O_4 precursors in a $120 \text{ }^\circ\text{C}$ heat treatment. The most active CoFe_2O_4 /carbon material reached a maximum C_{sp} of 701.8 F g^{-1} at a current density of 1 A g^{-1} and only lost $\approx 9\%$ of its capacity over 10,000 cycles.

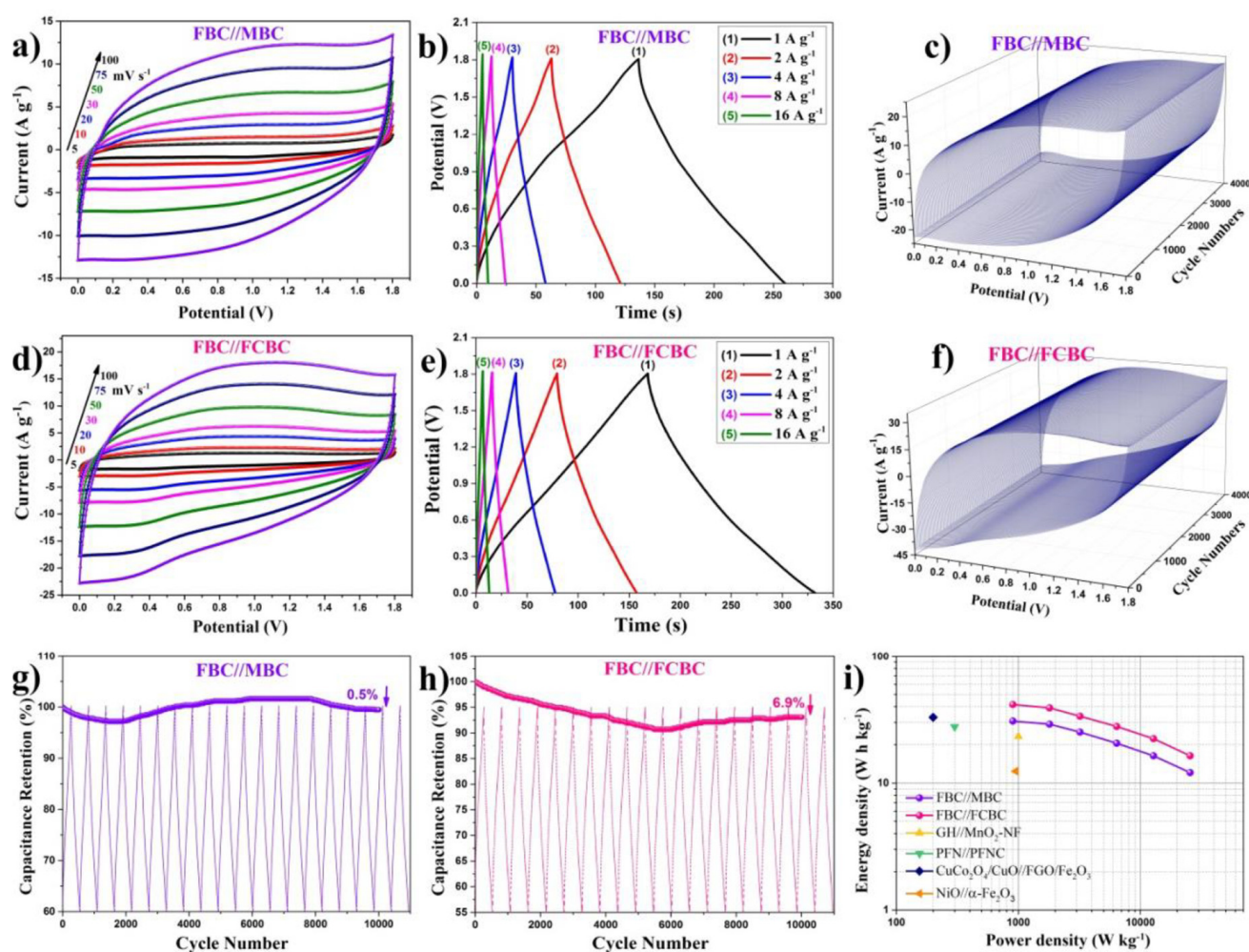


Figure 7. CV curves at different scan rates of FBC//MBC and FBC//FCBC (a,d), charge/discharge curves under different current densities of FBC//MBC and FBC//FCBC (b,e), 3D-CCV curves of the FBC//MBC and FBC//FCBC electrodes measured at scan rate of 200 mV s^{-1} (c,f), cycle performance of the FBC//MBC and FBC//FCBC electrodes at a the current density of 8 A g^{-1} (g,h), Ragone plot of FBC//MBC and FBC//FCBC (i) [127]. Reprinted with permission from [127]. Copyright 2018 American Chemical Society.

In addition to the study of Ni-Co/biocarbons and a CoFe_2O_4 /biocarbon as supercapacitor electrode materials, already described above, a pair of articles include a Co/biocarbon [130] and a bimetallic Co-Zn-containing nanocomposite [131]. The first monometallic Co/biocarbon [130] consists of Co_3O_4 /hollow carbon fibers obtained via cotton carbonization and subsequent deposition of Co_3O_4 nanoparticles, achieving a material able to reach an elevated C_{sp} (566.9 F g^{-1} at 1 A g^{-1}) and 69.4% capacitance retention up to 15 A g^{-1} in $6 \text{ M KOH}_{(aq)}$ electrolyte. Then, an asymmetric supercapacitor system with the Co_3O_4 /hollow carbon fibers and a cotton-derived carbon as positive and negative electrodes, respectively, showed a remarkable energy density (24.31 Wh kg^{-1} at a power density of 750 W kg^{-1}) and high cycling stability with no obvious capacitance decrease after 5000 cycles. The novel Co-Zn-containing material [131], reported in 2020, was fabricated by carbonizing CoZn-ZIF (zeolitic imidazole framework) previously grown on the surface of a fresh bamboo strip-derived carbon, exhibiting a maximum capacity of 757.8 F g^{-1} at 5 mV s^{-1} . Another biochar involving zinc—specifically, $\text{Zn}_4\text{Si}_2\text{O}_7(\text{OH})_2 \cdot \text{H}_2\text{O}$ anchored on bamboo-derived carbon support—was reported by Zhang et al. [132]. The authors assembled this nanocomposite within a flexible hybrid supercapacitor device using activated carbon as anode, delivering a maximum energy density of 0.69 Wh m^{-2} and showing 80% capacitance retention after

6900 cycles. From bamboo leaves as well, Wang et al. [133] described the production of CuO_x /biocarbons via the hydrothermal formation of CuO_x on the bamboo-derived carbon surfaces. This nanocomposite developed a C_{sp} equal to 147 F g^{-1} and uniquely lost 7% of its capacitance over 10,000 cycles in charge–discharge tests. In 2017, Genovese and Lian [134] proposed the integration of molybdenum into pinecone-derived biochar via polyoxometalate $[\text{PMo}_{12}\text{O}_{40}]^{3-}$ impregnation, producing a nanocomposite with a capacitance 2.5 times larger (1.19 F cm^{-2}) than that developed by the unmodified carbon. Additionally, the preparation of SnO_2 /BCH by using banana peel as feedstock and $\text{SnCl}_2 \cdot 2\text{H}_2\text{O}$ as precursor for the tin oxide was reported by Kaushal et al. [135] The SnO_2 /BCH electrode presented the following electrochemical metrics: maximum specific capacitance of 465 F g^{-1} (at 10 mV s^{-1}) and 476 F g^{-1} (at 0.15 A g^{-1}). Finally, Kouchachvili and Entchev [136] pyrolyzed residue from infested ash tree and then activated it with AgSO_4 and HNO_3 for obtaining a Ag/BCH supercapacitor material. The authors assembled two different symmetric supercapacitors—one using the Ag/BCH nanocomposite for the electrodes and the other one, with the Ag-free analog—for comparative purposes. Thereby, they observed that, at the same power density and current (366 W kg^{-1} and 1.3 mA , respectively), the first cell delivered up to 12.8 Wh kg^{-1} of energy density while the second only 8 Wh kg^{-1} .

Regarding the surface areas exhibited by the M-BCH electrodes for supercapacitors described below (see the fifth column of Table 6), the well-known positive influence of surface area developing on capacitance levels is not always clear. As can be seen in the chart below (Figure 8), the data present high dispersion and—at most current densities—negative trends with increasing surface area. This fact shows up that the pseudocapacitive effect of metals in M-BCH is preponderant and largely masks the influence of surface areas and porosity.

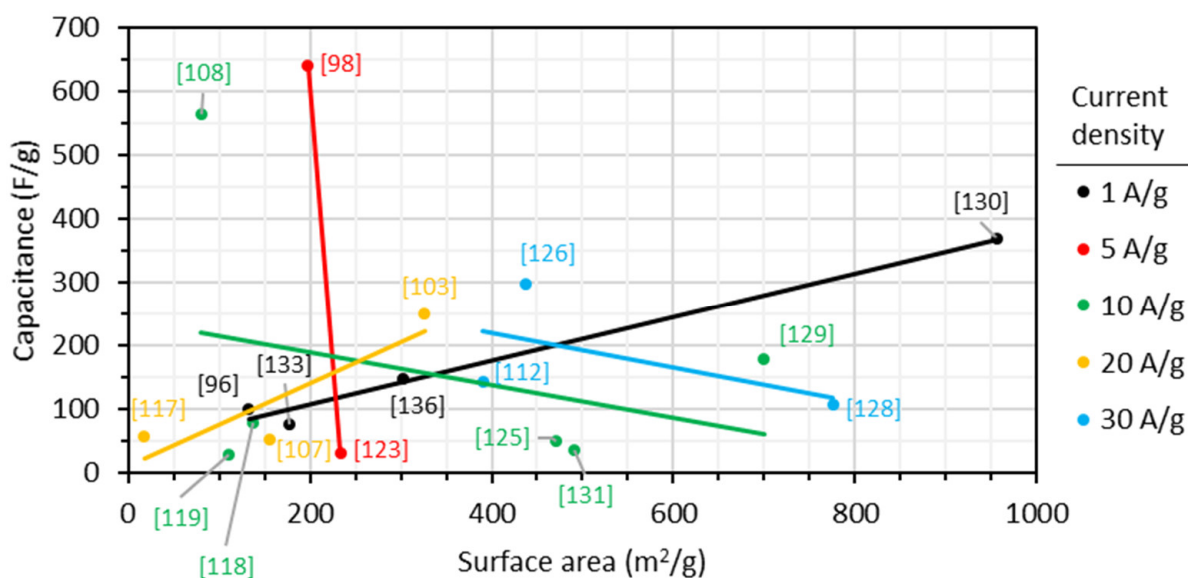


Figure 8. Relation between capacitance and surface area values of M-BCH included in this review. Only data from Table 6 expressed in F/g and m^2/g —for capacitances and surface areas, respectively—are included. Straight lines represent linear-fitted trends for each set of data. Numbers between brackets correspond to the references [own elaboration].

5.2. ORR, OER, HER

The ever-increasing energy demands all over the world and the necessity of reducing the consumption of fossil fuels has prompted the research for alternative power sources. In the last decades, electrochemical devices such as fuel cells and metal–air batteries have attracted a lot of attention as energy conversion/storage devices due to their green character and high conversion efficiency [137,138]. These technologies usually relied on electrochemical reactions, namely oxygen reduction, oxygen evolution, and hydrogen evolution

reactions (ORR, OER, and HER, respectively) on their cathodes or anodes [139]. However, all these reactions present sluggish kinetics and large overpotentials, limiting their energy efficiency [137,139,140]. Therefore, the development of adequate electrocatalysts is essential to the application of fuel cells and metal–air batteries.

Currently, platinum-based materials are considered the most promising electrocatalysts for both ORR and HER, while RuO₂ and IrO₂ exhibit the higher OER activity [140,141]. However, all these materials are known to have poor durability/stability, besides being scarce and too expensive which limits their large-scale application [140,142,143].

Carbon materials, on the other hand, are generally stable, inexpensive, and present promising electrochemical properties [138,144,145]. Furthermore, carbon catalysts doped with one or multiple heteroatoms (N, S, B, P, etc.) show an enhanced electrocatalytic performance for ORR [146], HER [147], and OER [140] mainly via induction of charge transfer and redistribution of electron density [140,146]. To date, materials such as carbon nanotubes, graphene, carbon nanofibers and activated carbon, were successfully applied as electrocatalysts for energy conversion/storage reactions [145,148–155]. However, it should be noted that the production of these materials is complex and expensive, which limits their practical application [156]. Additionally, these are produced from petrochemical products via energy-intensive or harsh synthetic processes. Meanwhile, the doped materials require heteroatom precursors which may be toxic and/or expensive and the doping process implies additional steps and costs in the catalyst synthesis [142,157].

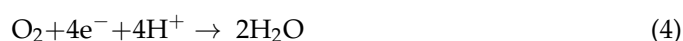
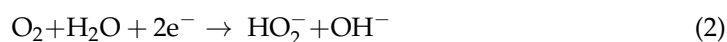
Biochars present an alternative for conventional carbon materials, being less expensive, derived from renewable and abundant feedstocks, environmentally friendly, and simple to produce [143,157,158]. Moreover, biomass is rich in functional groups, which may be beneficial for the electrocatalytic activity, and contain various heteroatoms in its composition [147,159]. Additionally, some biochars retain the original porous structure from the biomass source and various strategies can be applied for further increasing the porosity, promoting the mass transfer of reactants in catalytic reactions, and exposing active sites [142,160]. While the potential of biochars as electrocatalysts for ORR, OER, and HER is well-known [161–164], their electrocatalytic performance is still not up to the state-of-art catalysts.

Transition metals and their oxides, carbides, chalcogenides, phosphides, and nitrides also show great potential as electrocatalysts [165,166]. Their application in energy conversion and storage devices has attracted considerable attention by the scientific community due to their high specific capacity, natural abundance, low cost and toxicity, and tunable electrochemical properties [167,168]. However, these materials feature low electrical conductivity, low stability (specially in acidic electrolytes), and a tendency to agglomerate, leading to a reduction of the accessible active sites [169]. These difficulties can be suppressed by the incorporation of transition metals into a stable and highly conductive support, such as biochars. Indeed, the combination of metals and biochars (M-BCH) revealed to be extremely promising for the intended purpose. Not only the agglomeration and low stability of the metal species was limited as the overall electric conductivity of the material increased [167], but several extra advantages were reported, such as creation of more active sites, increase of specific surface area and enhanced porosity [170], leading to faster mass and charge transfers [171]. The metal species may be added before or after the carbonization of biomass and the biochar is often subject to activations or functionalization processes, since the electrocatalytic activity of biochar-based materials is strongly related with its surface area, functionalization, and aromatization degree [172].

5.2.1. Oxygen Reduction Reaction (ORR)

In aqueous electrolytes, oxygen reduction can occur through two mechanisms, involving the transfer of two (indirect pathway) or four electrons (direct pathway). The direct pathway consists in O₂ reduction to OH[−] in alkaline electrolytes (Equation (1)) or H₂O in acidic medium (Equation (4)). On the other hand, the indirect mechanism implies two reductions with the transfer of two electrons each and involves the generation of

intermediate species (HO_2^- and H_2O_2 in alkaline and acid electrolytes, respectively) before the reduction to water or OH^- . Equations (2), (3), (5) and (6) describe the two electrons mechanism in alkaline and acid medium, respectively.



The four electrons pathway is the desired one for energy conversion and storage devices, since it has a more positive potential, which allows a higher energy capacity [173]. Therefore, ORR electrocatalysts for energy storage/conversion applications should be highly selective for the direct mechanism, while showing high current densities and low overpotentials, such as Pt/C.

When comparing catalysts for ORR, some parameters should be considered, namely the onset potential (E_{onset}), diffusion-limited current density (j_L), Tafel slope (TF), and the number of electrons transferred per O_2 molecule (n_{O_2}). This last parameter can be determined by the Koutecky–Levich equation (Equation (7)), where j_K and j_L are the kinetic-limited and diffusion-limited current density, respectively [157], or via current densities measurements in bipotential mode using a rotating ring-disk electrode (RRDE). An ideal electrocatalyst for ORR presents high diffusion-limited current density, more positive E_{onset} , low Tafel slope and n_{O_2} close to 4. Besides, it should also exhibit long-term stability and, for application in methanol fuel cells, high tolerance to methanol crossover.

$$\frac{1}{j} = \frac{1}{j_L} + \frac{1}{j_K} \quad (7)$$

Recently, metal-doped biochars have attracted attention as electrocatalysts for ORR [137,143,170,174–176]. Hu et al., prepared a biomass-derived carbon doped with Co and CoO through the carbonization and activation with KOH of vegetable sponge (800 °C, 1 h) followed by immersion of the resulting material in a $\text{Co}(\text{NO}_3)_2 \cdot 6\text{H}_2\text{O}$ solution [143]. The material revealed to be a promising catalyst for ORR, showing similar Tafel slope and $E_{1/2}$ compared with Pt/C (64 vs. 54 mV/dec and 0.77 vs. 0.83 V (vs. RHE), respectively), while being selective for the four electrons pathway ($n_{\text{O}_2} = 3.91$) and extremely tolerant to methanol crossover. Since the undoped biochar presented a much lower electrocatalytic activity than the final material, with higher Tafel slope, lower selectivity and less positive E_{onset} and $E_{1/2}$, the enhancement was attributed to a synergistic effect between cobalt species and the biomass-derived carbon. Furthermore, the doping process allowed to conserve the honeycomb-like structure from the original biochar, which had a high specific surface area, increasing the amount of exposed active sites in the catalyst and, therefore, enhancing its electrocatalytic performance.

Biomass-based carbon materials co-doped with nitrogen and metal atoms, namely Fe [137,173,175], Zn [170], or Co [174], have shown interesting results in electrocatalysis, as several studies reported that metal–nitrogen–carbon (M–N–C) moieties can act as an important active site for ORR [137,174,177,178] by generating charge delocalization, promoting an easier O_2 adsorption [170]. Indeed, Zhang et al., reported a biomass-modified carbon black doped with nitrogen and iron exhibiting excellent ORR activity in alkaline electrolyte [173]. The catalyst, prepared by pyrolysis of a mixture containing acid treated leaves of *Ipomoea aquatica*, carbon black, and $\text{FeCl}_3 \cdot 6\text{H}_2\text{O}$ (900 °C, 2 h, N_2 atmosphere), presented a n_{O_2} around 3.90 and an onset potential of 0.05 V vs. Hg/HgO (0.91 V vs. RHE), which constituted a slightly higher overpotential than Pt/C but a similar n_{O_2} . Furthermore,

it also showed better durability than Pt/C over 2000 cycles and an excellent tolerance to methanol crossover. Besides the effect of Fe-N-C moieties, the catalytic performance was also attributed to the presence of pyrrolic-N in the material. It is known that pyrrolic, pyridinic, and graphitic N contribute greatly to the enhancement of ORR activity: pyrrolic N can enhance the chemisorption of O₂, graphitic N can increase the electrical conductivity and the limiting current density of the catalyst, while pyridinic N can act as an electron supply and has a positive effect on the overpotential for ORR; both pyridinic and graphitic N promote the cleavage of O=O bond, by modifying the electron distribution [168,179].

A zinc and nitrogen doped carbon derived from chitosan (Zn-N-C) also revealed to have promising activity towards ORR electrocatalysis in alkaline medium [170]. The material was obtained via carbonization of chitosan and Zn(NO₃)₂·6H₂O at 900 °C for 2 h; an acid treatment was then performed to remove undoped Zn and Zn oxides. The catalyst showed an onset and half-wave potential of 0.96 V and 0.86 V vs. RHE, respectively, which correspond to more positive values than the ones observed with Pt/C (0.94 and 0.81 V vs. RHE, respectively). Its limiting current density, around 6.7 mA cm⁻², was also more advantageous than the state-of-the-art catalyst (≈5.8 mA cm⁻²), while also presenting better tolerance to methanol crossover, higher durability, and similar selectivity toward four electrons pathway ($n_{\text{O}_2} = 3.88\text{--}4.01$). According to the authors, Zn-N species were essential for the electrocatalytic performance, as well as a large specific surface area.

A nanoporous carbon derived from corn silks was doped with N, P, and Fe by Wan et al. and applied as ORR catalysts, exhibiting a remarkable activity in alkaline medium [176]. The metal incorporation was effectuated after the carbonization (180 °C, 10 h), using FeCl₃ as precursor, and an annealing in NH₃ atmosphere (850 °C, 1 h) was performed after and before the incorporation, in order to introduce N and increase the porosity of the biochar. The synergistic effect between Fe, N, P, and the biochar, the presence of pyridinic and graphitic N and the interactions between N and P (P=N and P-N bonds) and N and Fe, led to more positive onset potential (0.957 V vs. RHE) and half-wave potential (0.852 V vs. RHE) than Pt/C (0.927 and 0.826 V vs. RHE, respectively), while maintaining the same selectivity for the desired pathway (Figure 9). Comparing the performance of the four M-doped catalysts presented above, all studied in alkaline medium (0.1 M KOH), M, N co-doped biochars appear to be more promising than the one doped only with metal, probably due to the presence of highly active M-N-C sites.

On the other hand, Zhang and coworkers decorated N-doped porous carbon derived from *porphyra* with single Fe atoms [178]. Their strategy consisted of limiting the agglomeration of single Fe atoms, that can act as active sites for ORR in Fe-N-C moieties, by the utilization of a porous biomass-derived carbon support. The iron source selected was hemin, added after a carbonization/activation process of the biomass in presence of KOH (900 °C, 2 h, Ar atmosphere); a second carbonization was effectuated after the metal introduction (800 °C, 2 h, Ar atmosphere). The resulting material showed high BET surface area and the original porous structure of the biomass, with a large quantity of microporous and mesoporous, providing active sites for ORR and improving the mass transport. The single Fe atoms in Fe-N-C complexes revealed to be extremely active sites, as deduced from the excellent ORR activity of the catalysts: $j_L = 5.0 \text{ mA cm}^{-2}$, $E_{1/2} = 0.87 \text{ V}$ (vs. RHE), $TS = 52 \text{ mV dec}^{-1}$, $n_{\text{O}_2} = 4.0$; for comparison, Pt/C catalyst presented similar values for j_L and n_{O_2} , but higher TS (61 mV dec⁻¹) and less positive $E_{1/2}$ (0.84 V).

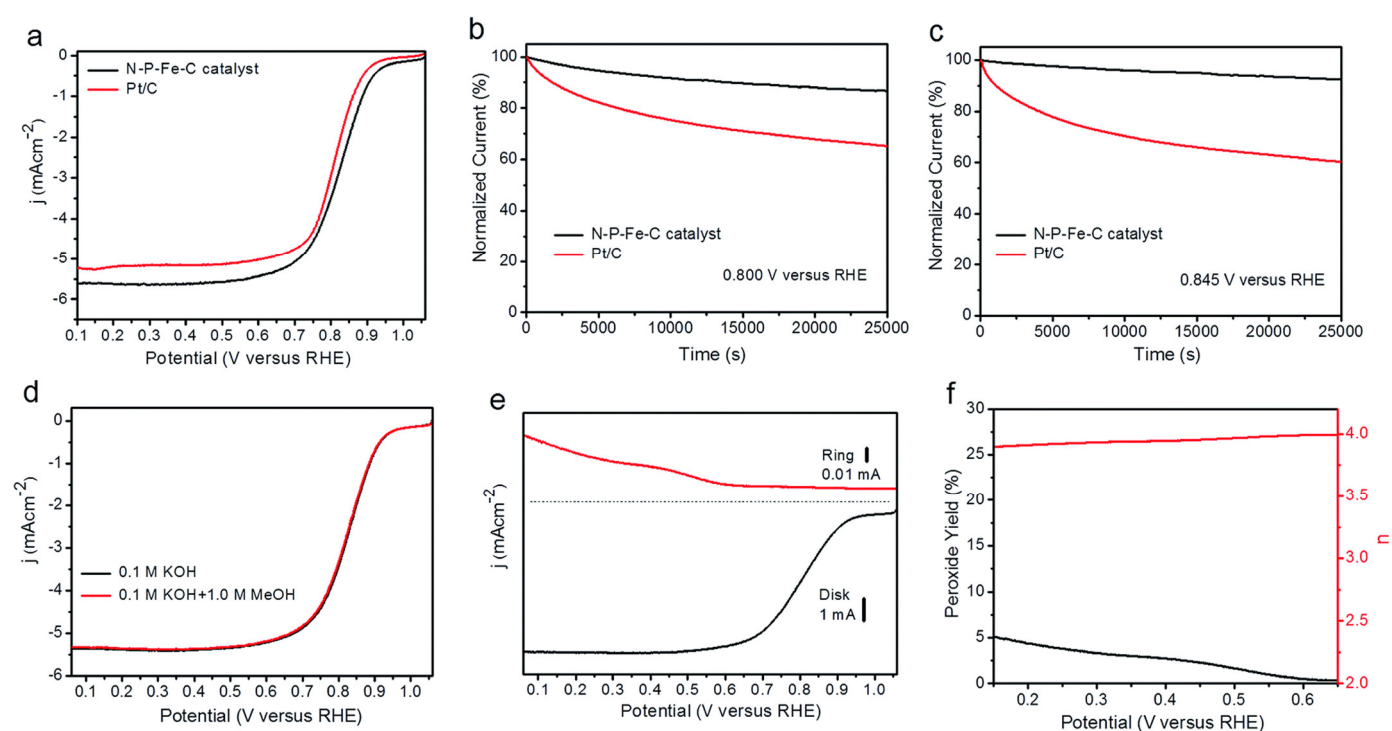


Figure 9. (a) Polarization curves for N, P, Fe tri-doped biochar (N-P-Fe-C) and Pt/C obtained at 1600 rpm in 0.1 M KOH; (b) chronoamperograms obtained at $E = 0.800$ V vs. RHE or (c) $E = 0.845$ V vs. RHE; (d) polarization curves for N-P-Fe-C catalyst in absence/presence of methanol; (e) RRDE voltammograms; (f) peroxide yield and number of electrons transferred per O₂ molecule for N-P-Fe-C. Reproduced from [176] with permission from the Royal Society of Chemistry.

Various transition metal oxides supported on biochars have also attracted attention as electrocatalysts for ORR in alkaline electrolytes, namely α -MnO₂ [171], CeO₂ [172], Ni-Co oxides [167], CoO [180], and LaMnO₃ [142]. For example, Pi et al. obtained a CeO₂-encapsulated N-doped biochar catalyst by two processes: in the first method, a metal accumulating plant (*Iris sibirica* L.) was pyrolyzed (900 °C, 2 h, N₂ atmosphere) after having extracted Ce cations from environment; the second strategy consisted of the plant carbonization (900 °C, 2 h, N₂ atmosphere) before the accumulation of Ce, followed by loading of CeO₂ NPs via sonication. The first approach resulted in better catalytic properties as the stronger interaction between CeO₂ and the N-doped biochar allowed a synergistic effect, which was not observed in the second material. Furthermore, the first material presented similar catalytic performance to that of Pt/C, with an onset potential of 0.90 V (vs. RHE), diffusion limiting current density of 2.02 mA cm⁻² and n_{O_2} around 3.55, while showing excellent stability. Through XPS results, the authors concluded that Ce³⁺ was present in the CeO₂ NPs, which generated oxygen vacancies and promoted the chemisorption and activation processes of O₂. Additionally, DFT calculations showed that (1) CeO₂ has the ability to store and release O₂, increasing the access of O₂ to the catalyst; (2) pyridinic N had a strong positive influence in O₂ chemisorption; and (3) defective CeO₂ crystals led to a higher selectivity towards the four electrons pathway (Figure 10).

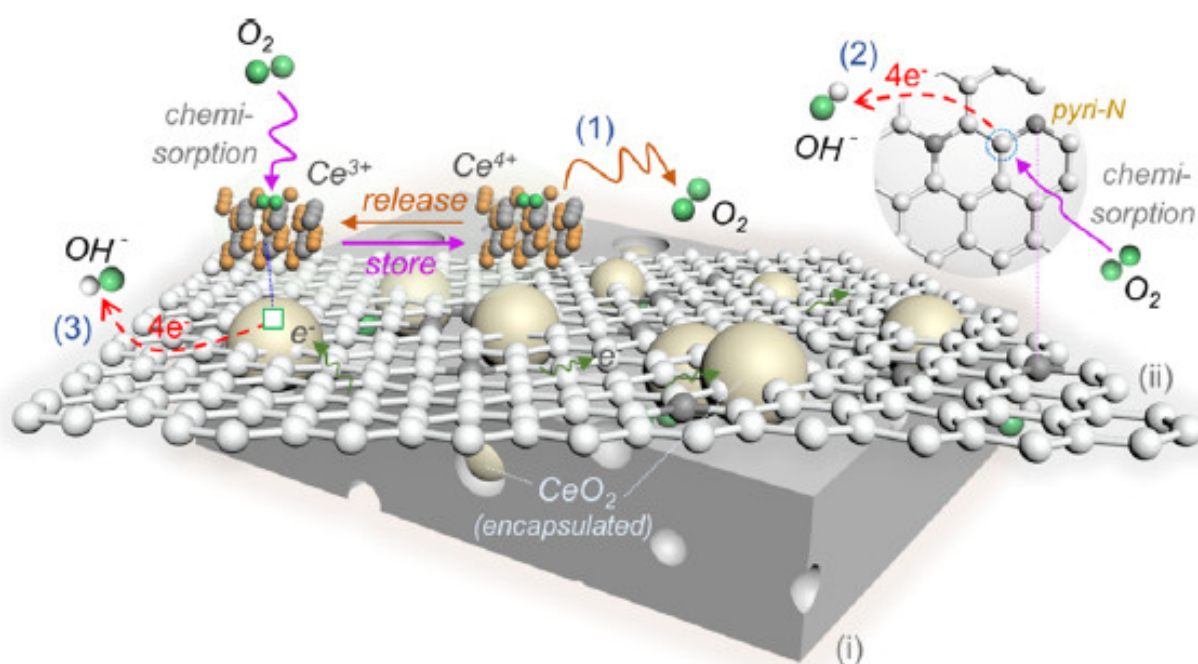
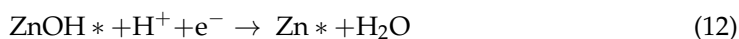
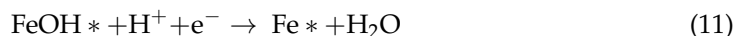
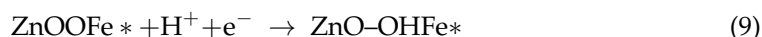


Figure 10. Mechanism for ORR electrocatalysis by (i) CeO₂-encapsulated N-doped biochar and (ii) an aromatic cluster. Reprinted with permission from [172]. Copyright 2020 American Chemical Society.

Another popular strategy for enhancing ORR activity consists of introducing metal sulfides in carbon materials [181–185]. For instance, Jiang et al., obtained an excellent electrocatalyst and highly selective for the four-electron pathway in alkaline medium by incorporating FeS and ZnS in N, S-doped carbon derived from Sichuan pepper [186]. The metal sulfides were loaded on the biomass source before carbonization at 900 °C (2 h, N₂ atmosphere) using NaSCN, FeCl₃, ZnCl₂, and 2,2-bipyridine as reactants. HR-TEM and Mott–Schottky results indicated the formation of numerous FeS/ZnS heterojunctions, which reportedly have the effect of increasing the electron transfer rate [179,187] and enhancing the absorption capacity of O₂ molecules [186]. Furthermore, as both metal sulfides are semiconductors and heterojunctions are photo-responsive, the catalytic properties of the material can be enhanced via light irradiation. Indeed, it was observed a significant increase in the diffusion-limiting current density (6.02 vs. 5.60 mA cm⁻²) and a shift for more positive potentials of E_{onset} (1.10 vs. 1.00 V (vs. RHE)) and $E_{1/2}$ (0.885 vs. 0.880 V (vs. RHE)) under light irradiation (Figure 11). It is important to notice that even without the light influence the material presented slightly better ORR performance than Pt/C, which showed a less positive $E_{1/2}$ (0.860 V vs. RHE) and lower diffusion-limiting current density (5.50 mA cm⁻²), while obtaining similar E_{onset} compared with the non-irradiated material. DFT calculations confirmed that the FeS/ZnS heterojunctions led to enhanced absorption capacity of O₂ and higher charge transfer. The authors proposed the following ORR mechanism (Equations (8)–(12)), where * indicates active site:



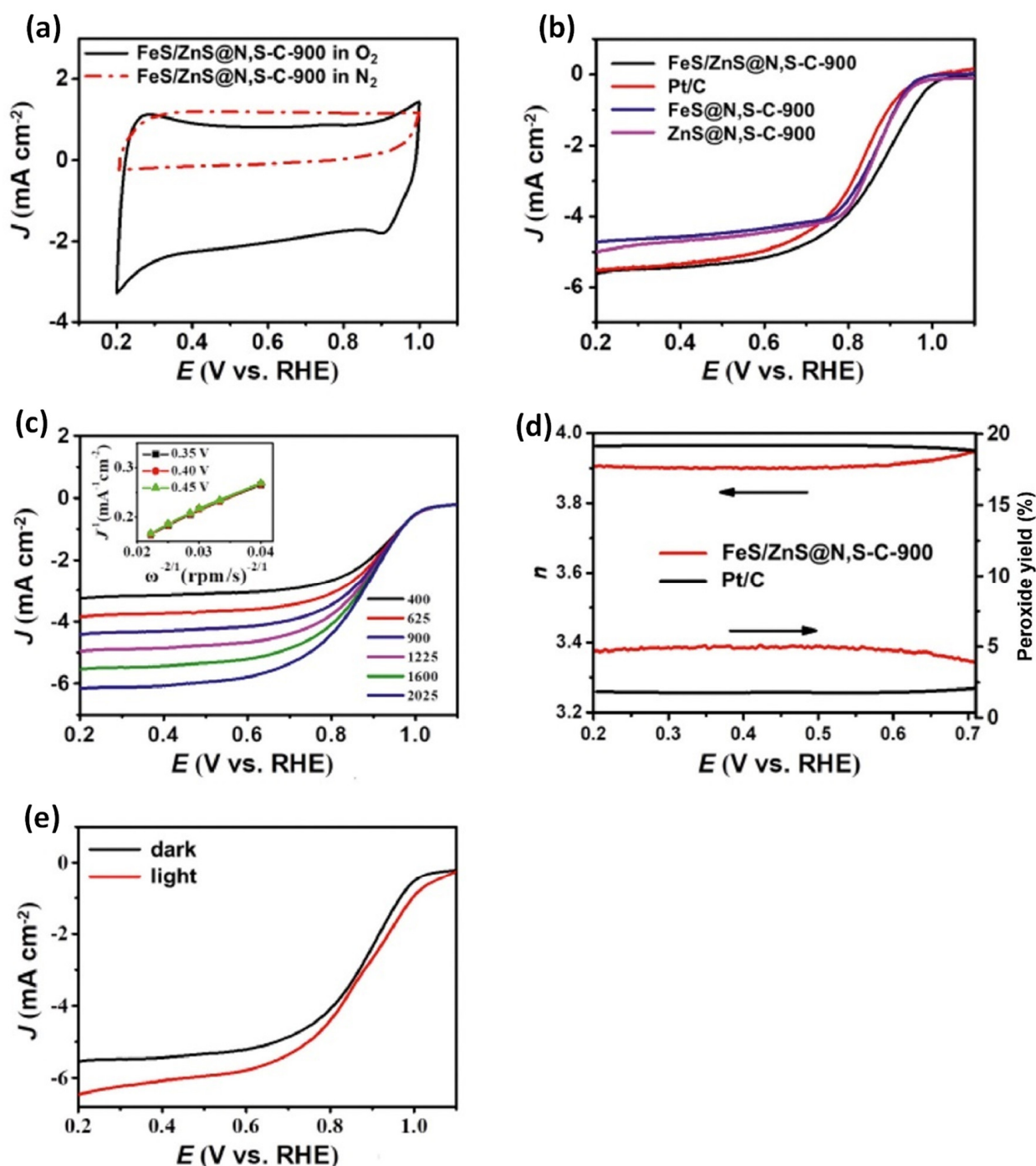


Figure 11. (a) CVs of FeS and ZnS incorporated in N, S-doped carbon derived from Sichuan pepper (FeS/ZnS@N,S-C-900) in N₂ and O₂-saturated 0.1 M KOH electrolyte; (b) LSV curves of the original FeS/ZnS@N,S-C-900, the catalyst prepared without ZnS (FeS@N,S-C-900) or FeS (ZnS@N,S-C-900), and commercial Pt/C; (c) LSV curves of FeS/ZnS@N,S-C-900 at different rotation speeds with the corresponding K-L plots; (d) number of electron transferred per O₂ molecule and H₂O₂ yield at the potential window of 0.2–0.7 V vs. RHE; and (e) LSV curves of FeS/ZnS@N,S-C-900 obtained in dark conditions or under light irradiation in O₂-saturated 0.1 M KOH electrolyte (1600 rpm, 10 mV s⁻¹). Reprinted from [186], Copyright (2020), with permission from Elsevier.

Recently, Lee and coworkers supported Co₂P NPs on porous N-doped carbon derived from bean sprouts via carbonization of the biomass source and CoCl₂ at 900 °C (Ar atmosphere) followed by annealing at 750 °C in NH₃ atmosphere to promote the formation of

micropores and, thus, the increase of the specific surface area [146]. While the material is not totally selective for the four-electron pathway ($n_{O_2} = 3.56$), it still showed a more positive $E_{1/2}$ (0.836 vs. 0.825 V vs. RHE) and lower Tafel slope (81.71 vs. 93.44 mV dec⁻¹) than Pt/C in alkaline electrolyte. The promising electrocatalytic performance was mainly attributed to the presence of pyridinic N and Co coordinated with N, which provide important active sites for ORR, and to the reported synergistic effect between pyridinic N and Co.

Transition metal carbides-based materials have also been successfully applied in electrocatalysis, due to their high electrical conductivity, chemical stability, and similar electronic properties to Pt [10,188,189]. In the last years, Wu et al. [177] and Xiong et al. [168] supported transition metal carbides on biochars to enhance the number and accessibility of active sites for ORR in the catalyst. In the first case, Fe₃C particles were retested with N-doped graphitic carbon derived from biomass in a core-shell structure through carbonization of microalgae and FeCl₂·5H₂O in NH₃ atmosphere at high temperature (1000 °C, 1 h). The resulting material was highly selective for the four-electron pathway ($n_{O_2} = 3.91$) and presented similar E_{onset} (1.0 V vs. RHE) and Tafel slope (65.3 mV dec⁻¹) and slightly more positive $E_{1/2}$ (0.864 V vs. RHE) compared with the ones obtained with Pt/C in alkaline electrolyte. These results confirmed the activity of Fe₃C towards ORR, which in combination with N-doped biochar generated a synergistic effect responsible for the excellent electrocatalytic activity.

The WC/N-doped carbon nanocomposite derived from corn crumbs prepared by Xiong et al. displayed a good ORR performance in alkaline medium, exhibiting higher diffusion-limiting current density, durability, and tolerance to methanol crossover than Pt/C, despite the slightly less positive onset potential (0.865 V vs. RHE) [168]. The catalyst, obtained via a pyrolysis/electrolysis route (750 °C, 3.0 V, 24 h) of a mixture of corn crumbs and WS₂ in molten NaCl-KCl salt, presented a one-dimensional geometry containing gnarled nanofibers. These structures had an important effect in the electrocatalytic activity of the material by promoting the charge transfer and O₂ diffusion. Simultaneously, WC and the nitrogen doped in graphitic and pyridinic positions provided a large number of active sites for ORR, enhancing the catalytic performance.

Up to date, the application of M-BCH as ORR electrocatalysts in neutral and acidic media is less frequent than in alkaline media, as can be observed in Table 7, since ORR catalysis is usually more favorable in the latter. Nevertheless, Fe, N-co-doped biochars derived from soybean straw [138] and catkins [190] have been used as electrocatalysts for ORR in acidic electrolytes with considerable success. Meanwhile, in neutral media, MnO₂ nanocrystals [158], iron oxides NPs [157], Fe₃C/WC [191], and Fe₃Se₄/FeSe [179] were anchored onto carbons derived from vegetal biomass, showing promising electrocatalytic activity towards ORR.

Table 7. Electrocatalytic performance of metal-supported biochar-based materials for ORR in alkaline, neutral, and acidic electrolytes.

Nanomaterial Properties				ORR Metrics						Ref.
Biochar Feedstock ^(a)	Synthesis	Metal Specie(s)	Biochar Nanocomposite	Electrolyte	j_L (mA cm ⁻²)	E_{onset} (V)	$E_{1/2}$ (V)	TS (mV dec ⁻¹)	n_{O_2}	
Alkaline Medium										
Wetland plant (<i>Iris sibirica</i> L.)	The plant extracted Ce cations under a hydroponic environment; pyrolysis at 900 °C (2 h) under N ₂ flow	CeO ₂ NPs	CeO ₂ -encapsulated N-doped biochar	1 M KOH	2.02	0.90 (vs. RHE)	0.84 (vs. RHE)	71	3.55 ^(a)	[172]
Vegetable sponge	Pre-carbonization at 500 °C (4 h, N ₂ atmosphere); activation with KOH at 800 °C (1 h); immersion on Co(NO ₃) _x ·6H ₂ O aqueous solution; ultrasonication (30 min)	Co and CoO	Biomass-derived carbon with cobalt/cobalt oxide doping	0.1 M KOH	≈4.7	0.86 (vs. RHE)	0.77 (vs. RHE)	64	3.91 ^(a)	[143]
Pomelo peel	Mixing of pomelo peels with melamine, cobalt nitrate and KOH; pyrolysis/activation at 800 °C (1 h, N ₂ atmosphere); acid leaching (HCl)	Co	Biomass-derived carbon with N/Co doping	0.1 M KOH	5	0.87 (vs. RHE)	0.78 (vs. RHE)	-	3.90 ^(a) or 3.85 ^(b)	[174]
Biomass tar	Mixing of biomass tar, urea and FeCl ₃ in aqueous solution followed by freeze-drying; carbonization at 700 °C (3 h, N ₂ atmosphere); immersion in HCl solution	Fe	Hierarchically porous Fe, N-co-doped carbon with in situ coated graphene from biomass tar	0.1 M KOH	≈5	0.04 (vs. Ag/AgCl)	-	-	3.98 ^(a)	[137]
Red dates	Mixing of red dated with g-C ₃ N ₄ and Fe(AcO) ₂ ; pyrolysis at 800 °C (1 h, N ₂ atmosphere); washing with HCl	Fe	Biomass based iron and nitrogen co-doped 3D porous carbon	0.1 M KOH	4.5	0.08 (vs. Hg/HgO)	-0.05 (vs. Hg/HgO)	-	3.71 ^(a)	[175]
Fresh leaves of <i>Ipomoea aquatica</i>	Acid etching of leaves (H ₂ SO ₄); mixing of the treated leaves with FeCl ₃ ·6H ₂ O and carbon black via ball milling; pyrolysis at 900 °C (2 h, N ₂ atmosphere)	Fe	Biomass-modified carbon black	0.1 M KOH	-	0.05 (vs. Hg/HgO)	-	-	~3.90 ^(a)	[173]

Table 7. Cont.

Nanomaterial Properties				ORR Metrics						Ref.
Biochar Feedstock ^(a)	Synthesis	Metal Specie(s)	Biochar Nanocomposite	Electrolyte	j_L (mA cm ⁻²)	E_{onset} (V)	$E_{1/2}$ (V)	TS (mV dec ⁻¹)	n_{O_2}	
Alkaline Medium										
Corn silks	Hydrothermal carbonization (180 °C, 10 h); annealing in NH ₃ atmosphere (850 °C, 1 h); mixing with FeCl ₃ ; annealing in NH ₃ atmosphere (850 °C, 1 h)	Fe	N-, P- and Fe-tridoped nanoporous carbon derived from plant biomass	0.1 M KOH	-	0.957 (vs. RHE)	0.852 (vs. RHE)	-	3.87–3.99 ^(b)	[176]
Soybean straw	Pyrolysis at 800 °C using soybean straw, melamine, magnesium oxide and ferric nitrate (2 h, N ₂ atmosphere); treatment with HCl	Fe, Fe ₃ C and Fe ₃ O ₄	Biomass-derived Fe-N co-doped porous carbon with honeycomb structure	0.1 M KOH	-	0.989 (vs. RHE)	0.854 (vs. RHE)	69	3.97 ^(a)	[138]
Catkins	Mixing of catkins with melamine and FeCl ₃ in aqueous medium (100 °C until complete water evaporation); pyrolysis at 800 °C (2 h); immersion in H ₂ SO ₄ (80 °C)	Fe	Fe/N co-doped CNT@hollow carbon fibers derived from plant biomass	0.1 M KOH	4.08	-0.098 (vs. Ag/AgCl)	-0.194 (vs. Ag/AgCl)	65.8	3.915 ^(a)	[190]
Chitosan	Mixing of chitosan and Zn(NO ₃) ₂ ·6H ₂ O in aqueous solution; drying at 80 °C; thermal treatment at 900 °C (2 h, air) + treatment with HCl	Zn	Zn-N-carbon from biomass resource chitosan	0.1 M KOH	≈6.7	0.96 (vs. RHE)	0.86 (vs. RHE)	-	3.88–4.01 ^(a)	[170]
Porphyra	Pre-carbonization of porphyra (300 °C, 1 h, air); carbonization/activation process with KOH (900 °C, 2 h, Ar atmosphere); washing with acid; mixing with hemin; carbonization (800 °C, 2 h, Ar atmosphere)	Single Fe atoms	Biomass derived N-doped porous carbon supported single Fe atoms	0.1 M KOH	5.0	-	0.87 (vs. RHE)	52	4.0 ^(a)	[178]

Table 7. Cont.

Nanomaterial Properties				ORR Metrics						Ref.
Biochar Feedstock ^(a)	Synthesis	Metal Specie(s)	Biochar Nanocomposite	Electrolyte	j_L (mA cm ⁻²)	E_{onset} (V)	$E_{1/2}$ (V)	TS (mV dec ⁻¹)	n_{O_2}	
Alkaline Medium										
Jackfruit seed	Hydrothermal treatment of jackfruit seed (180 °C, 24 h); carbonization (700 °C, N ₂ atmosphere); formation of Pt NPs from adsorbed Pt ions (chemical reduction of H ₂ PtCl ₆ using NaBH ₄)	Pt NPs	Bio-derived carbon enriched with N and decorated with Pt NPs	0.1 M KOH	4.9	0.89 (vs. RHE)	0.75 (vs. RHE)	74	3.8 ^(a)	[192]
Corncobs	Hydrothermal carbonization at 250 °C (12 h); activation with KOH (90 °C, 30 min); thermal treatment at 600 °C (1 h, N ₂ atmosphere); incorporation of MnO ₂ (hydrothermal method, 120 °C, 3 h)	α-MnO ₂	Hydrochars supporting α-MnO ₂	0.1 M KOH	2.85	−0.23 (vs. Ag/AgCl)	−0.32 (vs. Ag/AgCl)	-	3.27–3.81 ^(a)	[171]
<i>Typha domingensis</i>	Mixing of Co(II) and Ni(II) precursors with <i>Typha domingensis</i> in aqueous solution; heating of the resulting solution at 200 °C (12 h); centrifugation; pyrolysis at 700 °C (3 h) under argon atmosphere	Ni-Co oxides nanocapsules	Biomass-based carbon nanofibers composited with nickel-cobalt oxides	1 M KOH	0.23	−0.15 (vs. Ag/AgCl)	−0.32 (vs. Ag/AgCl)	-	-	[167]
Okara	Pyrolysis at 300 °C (2 h, N ₂ atmosphere); activation with KOH; pyrolysis at 700 °C (2 h, N ₂ atmosphere); treatment with HNO ₃ ; deposition of LaMnO ₃ NPs (sol-gel method); calcination at 350 °C (5 h, air) and 600 °C (4 h, vacuum)	LaMnO ₃ NPs	Perovskite LaMnO ₃ NPs anchored on biomass-derived N, P co-doped porous carbon	0.1 M KOH	≈4.2	-	-	76	3.82 ^(a)	[142]

Table 7. Cont.

Nanomaterial Properties				ORR Metrics						Ref.
Biochar Feedstock ^(a)	Synthesis	Metal Specie(s)	Biochar Nanocomposite	Electrolyte	j_L (mA cm ⁻²)	E_{onset} (V)	$E_{1/2}$ (V)	TS (mV dec ⁻¹)	n_{O_2}	
Alkaline Medium										
Soybean straws	KOH activation/pyrolysis (800 °C, 1 h, N ₂ atmosphere); mixing with CoCl ₂ in aqueous medium; drying (80 °C); carbonization at 800 °C (1 h, NH ₃ atmosphere); washing with HCl	CoO NPs	Sponge-like N-doped carbon materials with Co-based NPs derived from biomass	0.1 M KOH	5.8	0.87 (vs. RHE)	0.79 (vs. RHE)	-	4.03 ^(a) or 3.75 ^(b)	[180]
Sichuan pepper	Mixing of Sichuan pepper, NaSCN, FeCl ₃ , ZnCl ₂ and 2,2-bipyridine in aqueous medium (25 °C); drying at 60 °C; pyrolysis at 900 °C (2 h, N ₂ atmosphere)	ZnS and FeS	ZnS/FeS heterojunctions on biomass-derived porous carbon	0.1 M KOH	5.60	1.00 (vs. RHE)	0.880 (vs. RHE)	78	4 ^(a) or ≈3.9 ^(b)	[186]
Bean sprouts	Mixing with CoCl ₂ in aqueous medium (18 °C); drying (80 °C); heat-treatment at 900 °C (Ar atmosphere); annealing at 750 °C (NH ₃ atmosphere)	Co ₂ P NPs	Bio-derived Co ₂ P NPs supported on N-doped carbon	0.1 M KOH	-	-	0.836 (vs. RHE)	81.71	3.56 ^(a)	[146]
Microalgae	Mixing of microalgae powder with FeCl ₂ ·5H ₂ O; carbonization in NH ₃ atmosphere at 1000 °C (1 h)	Fe ₃ C	N-doped graphitic carbon from biomass	0.1 M KOH	-	1.0 (vs. RHE)	0.864 (vs. RHE)	65.3	3.91 ^(a) or 3.98 ^(b)	[177]
Corn crumbs	Mixing of corn crumbs with WS ₂ in molten NaCl-KCl; pyrolysis/electrolysis process (750 °C, 3.0 V, 24 h)	WC	WC/N-doped carbon nanocomposite	1 M KOH	-	0.865 (vs. RHE)	-	61.52	3.80 ^(a)	[168]
Neutral medium										
Microalgae <i>Chlorella pyrenoidosa</i>	Hydrothermal method at 180 °C (microalgae mixed with FeCl ₂ aq. solution, 12 h); pyrolysis at 900 °C (2 h, N ₂ atmosphere); ball milling	FeOOH, Fe ₃ O ₄ and α-Fe ₂ O ₃ NPs	Iron oxide NPs-embedded N-doped biocarbon	50 mM phosphate buffer solution	5.43	0.811 (vs. RHE)	0.589 (vs. RHE)	65.1	3.98 ^(b)	[157]

Table 7. Cont.

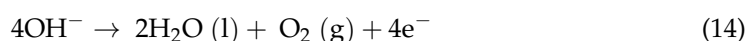
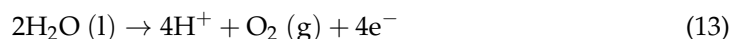
Nanomaterial Properties				ORR Metrics						Ref.
Biochar Feedstock ^(a)	Synthesis	Metal Specie(s)	Biochar Nanocomposite	Electrolyte	j_L (mA cm ⁻²)	E_{onset} (V)	$E_{1/2}$ (V)	TS (mV dec ⁻¹)	n_{O_2}	
Neutral medium										
Pine wood lumber	High temperature gasification (up to 1000 °C); alkaline pos-treatment	MnO ₂ nanocrystals	Graphitic biochar with supported MnO ₂	0.1 M Na ₂ SO ₄ (pH adjusted)	-	-	-	-	-	[158]
Cornstalk cores	Mixing of cornstalk cores, melamine, hydrazine hydrate, FeCl ₃ and Se powder (80 °C); drying; carbonization at 850 °C (2 h, N ₂ atmosphere)	Fe ₃ Se ₄ and FeSe	Fe ₃ Se ₄ /FeSe heterojunctions in cornstalk-derived N-doped carbon	50 mM phosphate buffer solution	-	-	-	-	3.764–4.06 ^(a)	[179]
Pomelo peels	Mixing of pomelo peels, K ₄ Fe(CN) ₆ and Na ₂ WO ₄ ; carbonization at 600–1100 °C (1.5 h, N ₂ atmosphere)	Fe ₃ C and WC NPs	Biomass-derived porous Fe ₃ C/WC/GC nanocomposite	50 mM phosphate buffer solution	-	-	-	-	3.95 ^(a)	[191]
Acidic medium										
Soybean straw	Pyrolysis at 800 °C using soybean straw, melamine, magnesium oxide and ferric nitrate (2 h, N ₂ atmosphere); treatment with HCl	Fe ₃ C and Fe ₃ O ₄	Biomass-derived Fe-N co-doped porous carbon	0.1 M KClO ₄	-	0.886 (vs. RHE)	0.754 (vs. RHE)	76	3.89 ^(a) or 3.65 ^(b)	[138]
Catkins	Mixing of catkins with melamine and FeCl ₃ in aqueous medium (100 °C until complete water evaporation); pyrolysis at 800 °C (2 h, N ₂ atmosphere); immersion in H ₂ SO ₄ (80 °C)	Fe	Fe/N co-doped CNT@hollow carbon fibers derived from plant biomass	0.5 M H ₂ SO ₄	-	0.586 (vs. Ag/AgCl)	-	-	3.9 ^(b)	[190]

^(a) Determined by Koutecky–Levich equation; ^(b) Determined by RRDE measurements.

In summary, biochar-based electrocatalysts containing non-precious metal species demonstrated excellent electrocatalytic properties for ORR, exhibiting similar or even superior catalytic performance than benchmark Pt-based materials.

5.2.2. Oxygen Evolution Reaction (OER)

In oxygen evolution reaction (OER), water or OH^- is oxidized to produce a O_2 molecule via a complex process involving several steps of electron transfer and numerous intermediates [193]. In acidic and neutral electrolytes this reaction is overall translated by Equation (13), while in alkaline electrolytes the process occurs slightly differently and according to Equation (14).



Similar to ORR, this reaction also suffers from large overpotentials and slow kinetics. Currently, rare metal oxides are the state-of-the-art catalysts for OER, with special focus on RuO_2 and IrO_2 [140]. To compare different electrocatalyst for this reaction, some electrochemical parameters must be taken in consideration, namely the exchange current density (j_0), overpotential (η_{10}) required by the catalyst to achieve a $j = 10 \text{ mA cm}^{-2}$, Tafel slope (TS) and turnover frequency (TOF). For both OER and HER this value of $j = 10 \text{ mA cm}^{-2}$ is the current density of interest since in the solar water splitting process this is the current density expected for a 12.3% efficient solar to hydrogen device, which would be required for cost-competitive photoelectrochemical water splitting [141].

Gao et al. reported the excellent electrocatalytic activity towards OER of a hierarchical mesoporous N-doped carbon derived from *Jasminum mesnyi* flower and decorated with FeNi NPs [140]. The catalyst was prepared through in situ freeze-drying of a mixture containing the biomass source, FeSO_4 and NiSO_4 , followed by pyrolysis at $900 \text{ }^\circ\text{C}$ (2 h, Ar atmosphere). Compared to IrO_2/C , the composite exhibited lower overpotential at 10 mA cm^{-2} (301 vs. 342 mV) and TS (49.7 vs. 64.5 mV dec^{-1}), much lower E_{onset} and higher stability in alkaline electrolyte. The enhanced performance was explained by the excellent intrinsic activity of FeNi NPs, the numerous active sites present in N-doped carbon, resulting from the high porosity and specific surface area, and by the presence of a synergistic effect between FeNi NPs and the carbon support.

Guo et al., on the other hand, opted for anchoring Ni-P in a 3D carbon support derived from biomass [194]. To obtain this material, holly leaves were firstly calcinated at $800 \text{ }^\circ\text{C}$ (2 h in N_2 atmosphere) and then Ni-P was introduced via electroless deposition. The composite showed a similar OER electrocatalytic performance compared to RuO_2 (Figure 12), obtaining a lower overpotential at 40 mA cm^{-2} (300 mV vs. 360 mV) but a higher Tafel slope (115.8 vs. 56.2 mV dec^{-1}). The high electrical conductivity and the hierarchical porosity of the overall material allowed an efficient charge and mass transport, which coupled to the high intrinsic catalytic activity of Ni-P led to a very promising catalytic performance for OER.

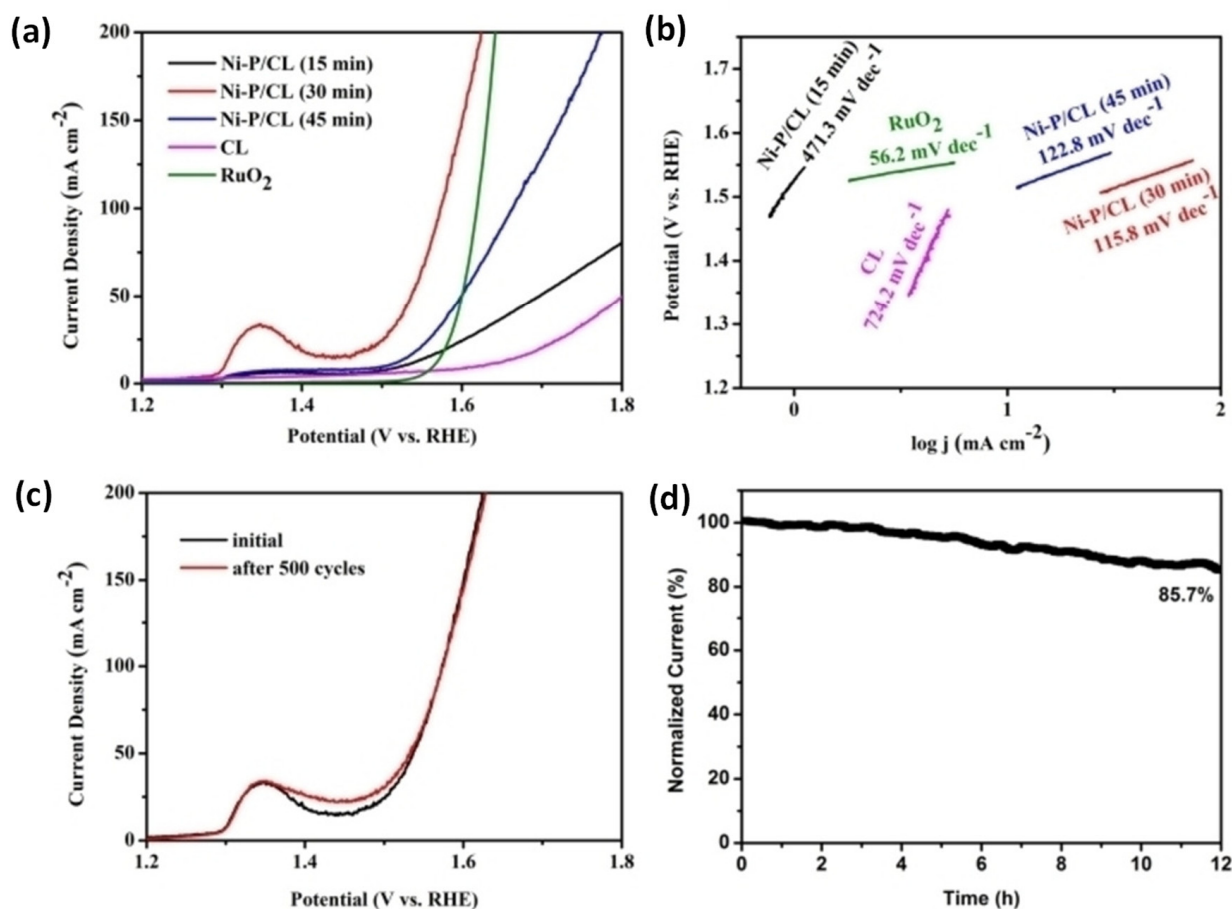


Figure 12. (a) LSV curves and (b) Tafel plots of Ni-P anchored in holly leaves-derived carbon (Ni-P/CL) with different deposition times (15, 30, and 45 min), the original carbon substrate (CL) and commercial RuO₂; (c) LSV curves of Ni-P/CL (30 min) during the initial and 500th cycle; and (d) chronoamperogram obtained at $E = 1.6$ V vs. RHE. Reproduced from [194] with the permission of Wiley.

5.2.3. Hydrogen Evolution Reaction (HER)

During hydrogen evolution reaction (HER), H₂ molecules are generated in acidic electrolyte via the reduction of H⁺ ions (Equation (15)) [141,156]. The overall process occurs through two steps: the first one involves the adsorption of a hydrogen atom (Volmer step), followed by the combination of two adsorbed hydrogens (Tafel step) or the reaction with a proton (Heyrovsky step) [141]. It should be noticed that an excellent catalyst for HER must absorb hydrogen atoms easily but not too strongly to allow these second steps [141].



In this reaction, electrocatalysts should be evaluated according to their overpotential (η), current density (j), Tafel slope (TS), turnover frequency (TOF), exchange current density (j_0), and Faradaic efficiency.

Nowadays, Pt-based materials show the most promising electrocatalytic activity towards HER [195,196]. To considerably reduce the utilization of Pt in HER electrocatalysis, Wang et al. loaded a trace amount of Pt NPs (0.15%) on a carbon support derived from wood, via magnetron sputtering [197]. This composite obtained a very low overpotential of 0.050 V at $j = 10$ mA cm⁻² and a Tafel slope of only 64 mV dec⁻¹ in alkaline media, suggesting that the HER process occurred through the Heyrovsky–Volmer mechanism. Surprisingly, a commercial Pt/C catalyst, containing 20% Pt, exhibited higher overpotentials and much lower current density at -0.2 V (vs. RHE) than the prepared material.

The authors attributed the enhanced electrocatalytic activity to the unique properties of the biochar, which presented a porous structure with an extremely ordered microtexture, contributing to a faster mass transport and promoting hydrogen adsorption/desorption.

On the other hand, in M-BCH electrocatalysts, Pt is usually replaced with non-precious materials, namely transition metal NPs [198] or metal phosphides [169], carbides [147,199] or sulfides [156]. For instance, Min et al. decorated a porous carbon membrane derived from biomass with Co NPs by mixing pomelo peels with $\text{Co}(\text{NO}_3)_2$ and annealing the mixture in air at 260 °C, followed by carbonization at 800 °C in N_2 atmosphere [198]. The material presented a 3D porous structure, with interconnected pores, highly dispersed Co NPs confined by a thin graphene layer and high surface area. The catalyst was tested for HER in alkaline electrolyte, obtaining an $\eta_{10} = 154$ mV, a Tafel slope of 106.4 mV dec^{-1} and an exchange current density of 1.009 mA cm^{-2} (Figure 13). Comparing to Pt foil, that corresponds to a considerably higher overpotential and Tafel slope (94 mV and 59.2 mV dec^{-1} , respectively), but a similar exchange current density (1.020 mA cm^{-2}). Furthermore, the prepared catalyst showed an excellent long-term stability (Figure 13) and a Faradaic efficiency close to 100%. The unique properties of this material contributed to its electrocatalytic performance: the hierarchical porosity allowed a fast diffusion of electrolyte and H_2 , the high graphitization degree of the carbon membrane conferred excellent electrical conductivity, promoting the charge transfer, and the homogeneously distributed Co NPs acted as active sites for HER.

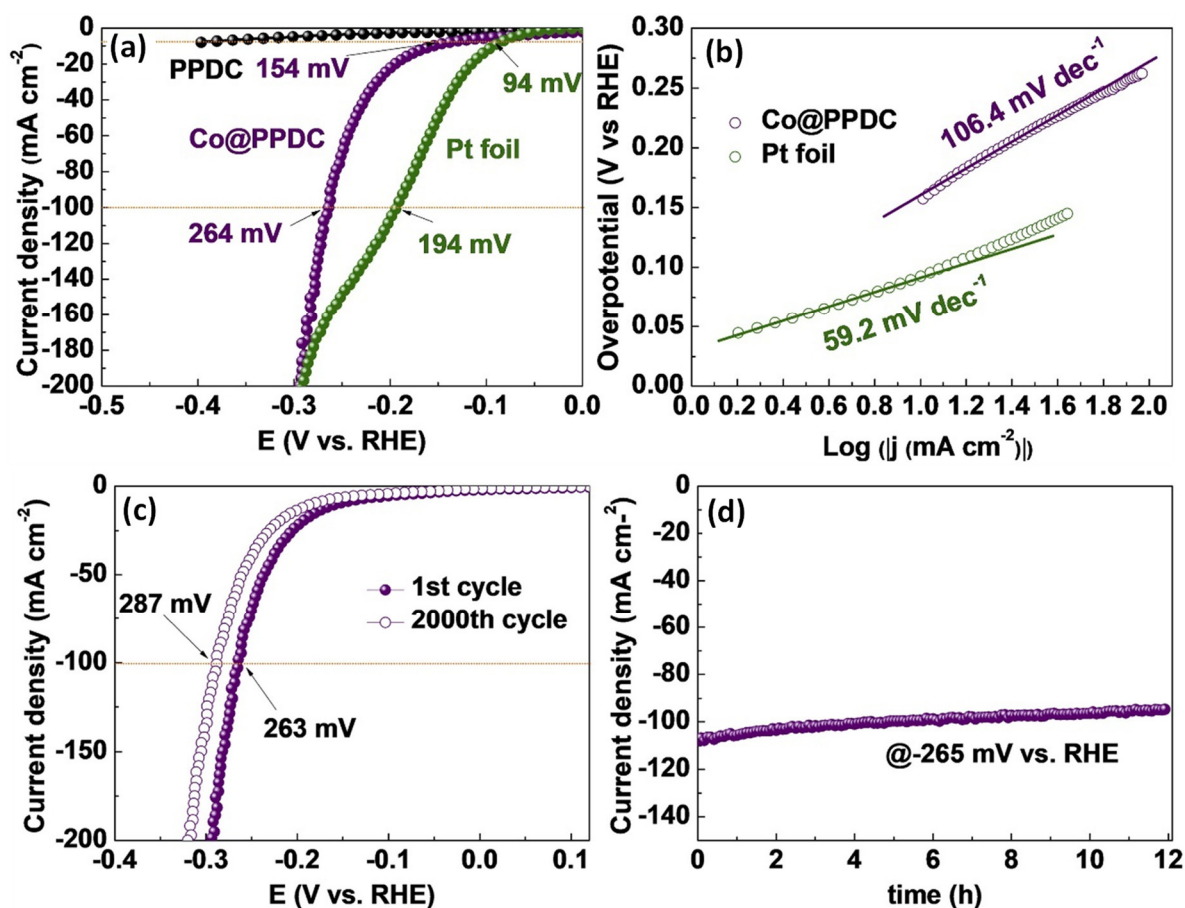


Figure 13. (a) LSV curves (1.0 M KOH, scan rate = 0.5 mV s^{-1}); (b) Tafel plots for a pomelo peel-derived porous carbon membrane embedded with Co NPs (Co@PPDC) and Pt foil; (c) LSV curves of Co@PPDC during the 1st and 2000th catalytic cycles; and (d) long-term stability tests of Co@PPDC at an overpotential of 265 mV in 1.0 M KOH electrolyte. Adapted from [198], Copyright (2020), with permission from Elsevier.

An et al., loaded Mo₂C in a S, N-doped carbon derived from sunflower seeds and evaluated its electrocatalytic activity for HER in both acid and alkaline medium [147]. In 1 M KOH electrolyte, the obtained performance was comparable to the one of Pt, presenting a low η_{10} of 60 mV, a Tafel slope of 71 mV dec⁻¹, an exchange current density of 1.07 mA cm⁻² and a Faradaic efficiency close to 100%. In 0.5 M H₂SO₄ media, the overall electrocatalytic activity is poorer, showing higher overpotential (146 mV) and Tafel slope (83 mV dec⁻¹) and significantly lower exchange current density (0.136 mA cm⁻²). In both cases, the material showed an outstanding long-term stability. Mo₂C is a promising material for HER, as it shows comparable energy band structures to Pt [147]. The introduction of graphitic S, N-carbon compensated for the low electrical conductivity of the carbide. Furthermore, Mo₂C particles were highly dispersed on the carbon matrix, which provided numerous active sites for HER and allowed a fast charge transfer. Finally, the high surface area of the catalyst also contributed to its excellent electrocatalytic performance by promoting diffusion of H₂ and ions and exposing active sites.

Guo et al., obtained similar results with a Mo₂C/C electrocatalyst, in which carbon was obtained from carbonization of pomelo peels and co-activated with N and K [199]. The electrocatalytic performance was also better in alkaline electrolytes than in acidic ones, but long-term stability was obtained in both media. However, this catalyst showed slightly higher Tafel slopes and overpotentials at $j = 10 \text{ mA cm}^{-2}$ than the values presented by the material prepared by An et al.

MoS₂ nanosheets are also promising HER electrocatalysts due to their outstanding electrocatalytic activity and relatively low cost [156]. To minimize the large overpotentials obtained with this material, MoS₂ should be assembled with a highly conductive porous carbon support. This strategy was applied by Qiao et al., which dispersed MoS₂ nanosheets in a carbon tube matrix (MoS₂/BCTM) [156]. In this case, wild celery, a plant with a very characteristic micropipe structure, was used as carbon source and template for the tube morphology (Figure 14). Carbon tubes are chemically stable, highly conductive materials and this specific structure allows enhanced mass transfer, as it provides additional transfer pathways [156]. Furthermore, the high surface area implies numerous exposed active sites, leading to a superior electrocatalytic performance. Indeed, the prepared electrocatalyst showed good activity for HER in acid medium, obtaining a Tafel slope of 51 mV dec⁻¹, $\eta_{10} = 176 \text{ mV}$ at $j = 10 \text{ mA cm}^{-2}$ and $j_0 = 0.01 \text{ mA cm}^{-2}$, which corresponds to a slightly higher Tafel slope and overpotential and lower exchange current density compared to Pt/C.

To summarize, biochars decorated with Mo₂C, Co NPs, MoS₂, Pt NPs, CoP, and Ni₂P have successfully catalyzed the hydrogen evolution reaction, in acidic or alkaline media. To the best of our knowledge, the electrocatalytic performance towards HER of all the M-BCH reported in literature is compared in Table 8.

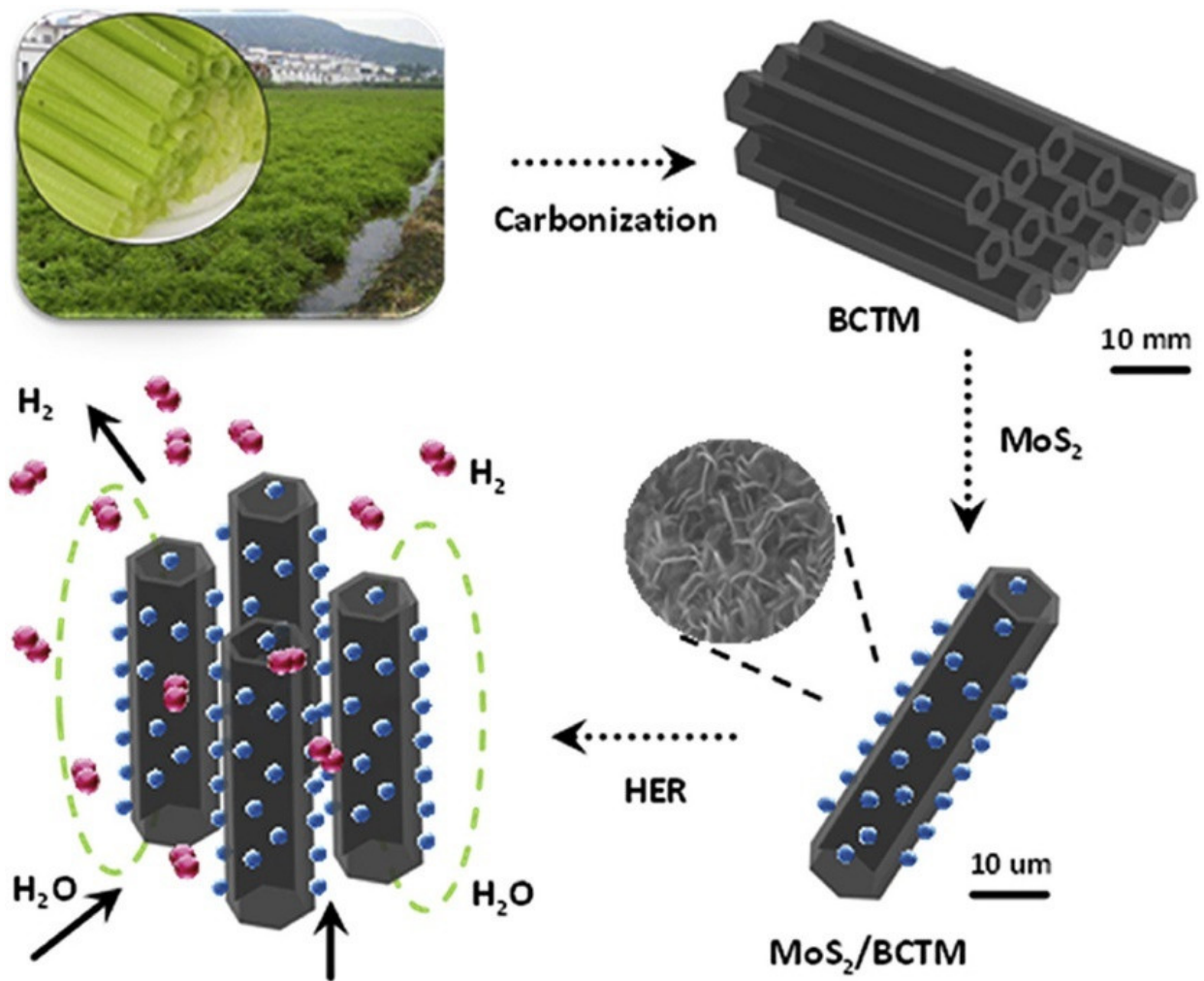


Figure 14. Preparation of MoS₂/BCTM electrocatalyst and its application in HER. Reprinted from [156], Copyright (2019), with permission from Elsevier.

Table 8. Electrocatalytic performance of metal-supported biochar-based materials for HER.

Nanomaterial Properties					HER Metrics				Ref.
Biochar Feedstock	Synthesis	Metal Specie(s)	Biochar Nanocomposite	Electrolyte	η_{10} (mV)	j_0 (mA cm ⁻²)	TS (mV dec ⁻¹)	Faraday Efficiency (%)	
Pomelo peels	Pre-carbonization with urea (400 °C); activation with KOH; mixing with (NH ₄) ₆ Mo ₇ O ₂₄ ; pyrolysis (800 °C, Ar)	Mo ₂ C	N, K Co-Activated biochar-derived molybdenum carbide	0.5 M H ₂ SO ₄	161	-	57	-	[199]
				1 M KOH	144	-	53	-	
Sunflower seeds	Treatment with 2 M HCl (10 h) and H ₃ PMo ₁₂ O ₄₀ (24 h); carbonization at 800 °C (4 h, Ar atmosphere)	Mo ₂ C	Mo ₂ C@S,N-carbon	0.5 M H ₂ SO ₄	146	0.136	83	-	[147]
				1 M KOH	60	1.07	71	≈100	
Pomelo peels	Mixing of pomelo peels with Co(NO ₃) ₂ ; annealing in air (260 °C, 6 h); carbonization (N ₂ atmosphere, 800 °C, 6 h)	Co NPs	Biomass-derived porous C membrane embedded with Co NPs	1 M KOH	154	1.009	106.4	≈100	[198]
Wild celery	Washing with HCl; carbonization at 750 °C (3 h, N ₂ atmosphere); incorporation of MoS ₂ (heating of biochar and an aqueous solution containing thiourea and hexaammonium heptamolybdate tetrahydrate at 220 °C, 18 h)	MoS ₂	Biomass carbon tube matrix auxiliary MoS ₂ heterojunction	0.5 M H ₂ SO ₄	176	0.01	51	-	[156]
Wood of Australian jarrah	Carbonization at 1000 °C, (Ar atmosphere); Pt incorporation via magnetron sputtering method (10 s, 10 mA)	Pt NPs	Platinum supported on carbonized biomorphic wood	1 M KOH	50	-	64	-	[197]
Seaweed	Graphene oxide (GO) was prepared using a modified Hummer's method and mixed with sodium alginate and then with Co(NO ₃) ₂ ·6H ₂ O; the mixture was dehydrated and carbonized with red phosphorus at 800 °C (240 min, N ₂ atmosphere)	CoP	Co _x P@C Core-shell NPs Embedded in 3D Cross-linked Graphene Aerogel	0.5 M H ₂ SO ₄	120	-	57	-	[169]
				1 M KOH	225	—	66	—	
Seaweed	Graphene oxide (GO) was prepared using a modified Hummer's method and mixed with sodium alginate and then with Ni(NO ₃) ₂ ·6H ₂ O; the mixture was dehydrated and carbonized with red phosphorus at 800 °C (240 min, N ₂ atmosphere)	Ni ₂ P	Ni _x P@C core-shell NPs embedded in 3D cross-linked graphene aerogel	0.5 M H ₂ SO ₄	305	-	74	-	[169]
				1 M KOH	340	—	97	—	

While only a small selection of metallic species has been immobilized on biochars, it is known that other metals—namely Fe, W, Cu, and Ru—are able to enhance the activity of distinct carbon materials towards HER [200–202]. For instance, Yang et al., reported the excellent catalytic performance of a WS₂ nanosheets/reduced graphene oxide composite for HER, which was attributed to the fast charge transfer resulting from the strong interaction between the metallic species and carbon support [202]. Encapsulated Fe/Fe₃C particles on S, N co-doped graphitic carbon also revealed promising electrocatalytic activity for HER—the incorporation of a doped-carbon support led to an increase of the number of available active sites, enhancing the Fe₃C performance [203]. Additional examples of metal/carbon catalysts for HER can be found in the comprehensive reviews provided by Wang [204]. Since the properties of biochars can be tuned to mimic conventional carbon materials (e.g., graphene, activated carbon, nanoporous carbon, etc.), it is expected that the immobilization of Fe, Cu, and W species could also improve their electrocatalytic performance towards HER. Nevertheless, experimental studies are still required to verify this hypothesis.

5.2.4. Multifunctional Electrocatalysts

Multifunctional electrocatalysts are able to catalyze more than one reaction, being specifically important in systems where several reactions with sluggish kinetics occur simultaneously. For instance, water splitting requires catalysts for both OER and HER [205], while some fuel cells, such as unitized regenerative fuel cells, and rechargeable metal–air batteries relies on OER and ORR [206,207]. The design of multifunctional electrocatalysts is challenging, as the reaction mechanisms and optimal experimental conditions are very distinct, and often the state-of-the-art catalysts for one reaction are not active towards other reactions [205–207].

Wang et al. prepared a bifunctional electrocatalyst for ORR and OER through the pyrolysis of a mixture containing *Chlorella*, cobaltous acetate, and melamine at 900 °C (1 h, Ar atmosphere), followed by an acid treatment and a second carbonization at 900 °C [208]. The resulting material presented Co NPs encapsulated in a bamboo-like N-doped carbon nanotubes, which is a highly beneficial structure for mass and electron transfer. In alkaline electrolyte, the catalyst showed better electrocatalytic performance for ORR and OER than commercial Pt/C and IrO₂/C, respectively: related to ORR, the material obtained a more positive half-wave potential (0.84 vs. 0.83 V vs. RHE) and a similar n_{O_2} , while also presenting a lower η_{10} value (352 vs. 375 mV) and Tafel slope (60 vs. 75 mV dec⁻¹) for OER. According to the authors, Co NPs acted as active sites for both reactions, while pyridinic N and graphitic N sites contributed mostly for ORR and OER process, respectively. As the catalyst possessed a high amount of these three species, it was able to efficiently promote both reactions.

Yang et al. also obtained an efficient bifunctional electrocatalyst for ORR and OER by co-doping a peanut shells-derived porous carbon with N and FeNi alloy [209]. The material was obtained via the carbonization of a mixture of peanut shells, melamine, and KOH at 900 °C (2 h, N₂) followed by the addition of FeCl₂·4H₂O and NiCl₂·6H₂O and the second carbonization step (900 °C, 2 h, N₂). The high specific surface area, high electrical conductivity, and suitable ratio of micro/mesopores of the resulting electrocatalyst, in combination with a high content of graphitic and pyridinic N, led to ORR and OER performances comparable to the state-of-the-art catalysts (Pt/C and IrO₂, respectively).

On the other hand, Lin et al. prepared an electrocatalyst for HER and OER to apply in electrochemical water splitting [210]. The material consisted of Co₂P@CoP core–shell structures embedded in porous carbon derived from ginkgo leaf, obtained from the carbonization of the biomass source, cobalt (II) nitrate and ammonium nitrate at 500 °C (N₂ atmosphere), followed by a thermal treatment at 350 °C in presence of sodium hypophosphite. Its electrocatalytic activity for OER and HER was evaluated in acidic and alkaline media, demonstrating to be an excellent catalyst for both processes over a wide range of pH due to the high intrinsic activity of Co₂P@CoP heterostructure, which favors hydrogen

and oxygen evolutions, while the high electrochemical active surface area of the porous carbon led to numerous active sites for both processes and the N, S doping promoted electron-donating, enhancing the overall electrochemical activity.

CoO NPs anchored on a watermelon peel-derived biochar also showed promising bifunctional electrocatalytic behavior towards OER and HER [211]. The nanocomposite, denoted as CCW-700, was prepared via a pre-carbonization at 400 °C (2 h, N₂ atmosphere), followed by a hydrothermal reaction in presence of CoCl₂·6H₂O at 120 °C (10 h), an activation treatment with KOH and calcination at 700 °C (2 h, N₂ atmosphere). The electrocatalyst showed a very promising OER performance in alkaline electrolyte, obtaining lower values of η_{10} and Tafel slope than commercial RuO₂. The HER performance of CCW-700 was adequate, although not comparable with Pt/C. Nevertheless, the electrocatalyst was successfully applied in water splitting and a good hydrogen production efficiency was achieved.

Liu et al. grew hollow porous MnFe₂O₄ spheres into a biochar (MnFe₂O₄/BC) by a one-pot solvothermal route (200 °C, 20 h), using MnCl₂·4H₂O and FeCl₃·6H₂O as metal precursors [212]. The biochar was obtained from the calcination of elm moneys at 600 °C for 2 h under N₂ atmosphere. The resulting composite achieved excellent OER and HER performances in alkaline medium, presenting low overpotentials and Tafel slopes and good stability. Moreover, MnFe₂O₄/BC was applied as cathode and anode in a water electrolyzer, requiring a low potential to achieve 10 mA cm⁻². Its outstanding electrocatalytic activity was explained by: (i) the numerous active sites for both reactions; (ii) the hollow porous structure of MnFe₂O₄, which contributes to efficient ion transport and exposure of active sites; (iii) the presence of oxygen vacancies and lattice defects, leading to lower activation energy for water dissociation; and (iv) favorable hydrophilicity of the overall material, facilitating the access of electrolyte to the catalyst.

A trifunctional electrocatalyst for ORR, OER, and HER in alkaline media, constituted by Ni NPs dispersed on P-doped carbon derived from waste carrot, was reported by Hoang et al. [139]. The material, prepared via carbonization at 800 °C of carrots and nickel (II) acetate tetrahydrate (2 h, in N₂), showed excellent activity towards OER, expressed by lower overpotential (368 mV), onset potential (1.52 V vs. RHE), and Tafel slope (67.6 mV dec⁻¹) compared to commercial IrO₂. Its ORR performance was also promising, presenting an onset and half-wave potentials of 0.81 and 0.67 V vs. RHE, a kinetic and limiting current densities of 13.66 and 4.19 mA cm⁻²; however, the electrocatalyst only achieved a moderate selectivity towards the four-electron pathway ($n_{O_2} = 3.2$). Meanwhile, the catalyst showed an appropriate electrocatalytic activity for HER ($E_{\text{onset}} = -0.157$ V vs. RHE, $\eta_{10} = 297$ mV, Tafel slope = 134.9 mV dec⁻¹), although lower than the one presented by Pt/C. According to the authors, Ni NPs displayed an important role in the material's electrocatalytic activity, by providing numerous active sites for the three processes and increasing the electrochemical active surface area, OH⁻ diffusion and electrical conductivity, while reducing the charge transfer resistance.

As so, some M-BCH materials showed potential to catalyze two or more energy-related reactions simultaneously without compromising its electrocatalytic performance.

6. Conclusions

Metal-supported biochar emerges as a sustainable and low-cost catalyst material for biorefinery and electrochemical applications, giving performance comparable or superior to traditionally commercial materials.

Due to the abundance of oxygen-containing functional groups (C=O and COOH) in the biochar obtained from hydrothermal carbonization of biomass feedstocks, this production method facilitates the incorporation of metal nanoparticles, providing an outstanding contribution to the dispersion and stability of metal active sites. Biochar matrix can also act as reductant of incorporated metal oxides, constituting a key advantage in terms of energy efficiency. This review highlights the activation methodology as crucial towards promising metal-supported biochar materials, since it strongly affects the final physicochemical prop-

erties (surface area, porosity, surface functionalization, metal dispersion, oxidation number, etc.). The relative significance of this step varies depending on type of biochar, metal precursors and loadings, being maneuvered through innovative synthesis/modification methodologies.

In this review, we have attempted to summarize methods for synthesizing and preparing metal-supported biochar catalysts for specific biorefinery reactions. Although these applications are expanding rapidly, the performance of these catalysts in some processes (except perhaps transesterification and tar removal/gasification reactions) is still limited in terms of selectivity and stability due to their complex surface chemistry and heterogeneity. It remains a challenge to gain a more precise understanding of the biochar structures and the synergies/interactions between the metal phase and the biochar matrix in order to understand the dominant reaction mechanisms.

Similarly, biochar-based electrodes containing non-precious metals also show interesting catalytic behavior towards supercapacitors, ORR, OER, and HER, displaying comparable or even better performance than the state-of-the-art electrocatalysts. Moreover, some biochars successfully acted as multifunctional electrocatalysts. Carefully tuning the textural and physical properties of metal/biochar-based materials may be challenging but is crucial for electrocatalysis application. Furthermore, the catalytic mechanism for the mentioned reactions in metal-supported biochar materials is not yet fully disclosed and needs further study. This limitation can be overcome by combining experimental and computational studies. For instance, DFT methods can greatly contribute to clarifying catalytic mechanisms.

Author Contributions: Conceptualization, A.F.P., D.M.F. and R.R.; writing—original draft preparation, A.F.P., D.M.F., R.R., R.M. and V.K.A.-F.; writing—review and editing, A.F.P., D.M.F., R.R., R.M. and V.K.A.-F.; visualization, A.F.P. and D.M.F.; supervision, A.F.P. and D.M.F.; funding acquisition, A.F.P. All authors have read and agreed to the published version of the manuscript.

Funding: This research received no external funding.

Acknowledgments: This work was funded by Fundação para a Ciência e a Tecnologia FCT/MCTES through national funds, projects: UIDB/50006/2020 and PTDC/BII-BIO/30884/2017. RRV thanks the project PTDC/BII-BIO/30884/2017 contract based on DL57/2016 funded by FCT/MCTES through national funds. DF thanks FCT/MCTES for their work contract supported by national funds (OE). AFP acknowledges FCT funding under the Scientific Employment Stimulus ref: 2020.01614.CEECIND/CP1596/CT0007. RM thanks FCT the PhD fellowship 2020.05342.BD.

Conflicts of Interest: The authors declare no conflict of interest.

References

1. Narayan, R. Biomass (renewable) resources for production of materials, chemicals, and fuels: A paradigm shift. *ACS Symp. Ser.* **1992**, *476*, 1–10.
2. Patel, M.; Zhang, X.; Kumar, A. Techno-economic and life cycle assessment on lignocellulosic biomass thermochemical conversion technologies: A review. *Renew. Sustain. Energy Rev.* **2016**, *53*, 1486–1499. [[CrossRef](#)]
3. Wang, S.; Li, H.; Wu, M. Advances in metal/ biochar catalysts for biomass hydro-upgrading: A review. *J. Clean. Prod.* **2021**, *303*, 126825. [[CrossRef](#)]
4. Sun, X.; Atiyeh, H.K.; Li, M.; Chen, Y. Biochar facilitated bioprocessing and biorefinery for productions of biofuel and chemicals: A review. *Bioresour. Technol.* **2020**, *295*, 122252. [[CrossRef](#)] [[PubMed](#)]
5. Li, D.-C.; Jiang, H. The thermochemical conversion of non-lignocellulosic biomass to form biochar: A review on characterizations and mechanism elucidation. *Bioresour. Technol.* **2017**, *246*, 57–68. [[CrossRef](#)] [[PubMed](#)]
6. Weber, K.; Quicker, P. Properties of biochar. *Fuel* **2018**, *217*, 240–261. [[CrossRef](#)]
7. Lee, J.; Kim, K.-H.; Kwon, E.E. Biochar as a catalyst. *Renew. Sustain. Energy Rev.* **2017**, *77*, 70–79. [[CrossRef](#)]
8. Liu, W.-J.; Jiang, H.; Yu, H.-Q. Development of biochar-based functional materials: Toward a sustainable platform carbon material. *Chem. Rev.* **2015**, *115*, 12251–12285. [[CrossRef](#)]
9. Oliveira, F.R.; Patel, A.K.; Jaisi, D.P.; Adhikari, S.; Lu, H.; Khanal, S.K. Environmental application of biochar: Current status and perspectives. *Bioresour. Technol.* **2017**, *246*, 110–122. [[CrossRef](#)]
10. Tan, X.; Liu, Y.; Zeng, G.; Wang, X.; Hu, X.; Gu, Y.; Yang, Z.J.C. Application of biochar for the removal of pollutants from aqueous solutions. *Chemosphere* **2015**, *125*, 70–85. [[CrossRef](#)]

11. Ali, S.; Rizwan, M.; Qayyum, M.F.; Ok, Y.S.; Ibrahim, M.; Riaz, M.; Arif, M.S.; Hafeez, F.; Al-Wabel, M.I.; Shahzad, A.N.J.E.S.; et al. Biochar soil amendment on alleviation of drought and salt stress in plants: A critical review. *Environ. Sci. Pollut. Res.* **2017**, *24*, 12700–12712. [[CrossRef](#)]
12. Van Zwieten, L.; Singh, B.; Joseph, S.; Kimber, S.; Cowie, A.; Chan, K.Y. Biochar and emissions of non-CO₂ greenhouse gases from soil. In *Biochar for Environmental Management Science and Technology*; Lehmann, J., Joseph, S., Eds.; Earthscan: London, UK, 2009; Volume 1, pp. 227–249.
13. Liu, R.; Xiao, H.; Guan, S.; Zhang, J.; Yao, D. Technology and method for applying biochar in building materials to evidently improve the carbon capture ability. *J. Clean. Prod.* **2020**, *273*, 123154. [[CrossRef](#)]
14. Mian, M.M.; Liu, G. Recent progress in biochar-supported photocatalysts: Synthesis, role of biochar, and applications. *RSC Adv.* **2018**, *8*, 14237–14248. [[CrossRef](#)]
15. Wang, S.; Shan, R.; Wang, Y.; Lu, L.; Yuan, H. Synthesis of calcium materials in biochar matrix as a highly stable catalyst for biodiesel production. *Renew. Energy* **2019**, *130*, 41–49. [[CrossRef](#)]
16. Chi, N.T.L.; Anto, S.; Ahamed, T.S.; Kumar, S.S.; Shanmugam, S.; Samuel, M.S.; Mathimani, T.; Brindhadevi, K.; Pugazhendhi, A. A review on biochar production techniques and biochar-based catalyst for biofuel production from algae. *Fuel* **2021**, *287*, 119411. [[CrossRef](#)]
17. Nguyen, H.K.D.; Pham, V.V.; Do, H.T. Preparation of Ni/biochar catalyst for hydrotreating of bio-oil from microalgae biomass. *Catal. Lett.* **2016**, *146*, 2381–2391. [[CrossRef](#)]
18. Wang, D.; Yuan, W.; Ji, W. Char and char-supported nickel catalysts for secondary syngas cleanup and conditioning. *Appl. Energy* **2011**, *88*, 1656–1663. [[CrossRef](#)]
19. Lyu, H.; Zhang, Q.; Shen, B. Application of biochar and its composites in catalysis. *Chemosphere* **2020**, *240*, 124842. [[CrossRef](#)]
20. Li, X.; Wang, C.; Zhang, J.; Liu, J.; Liu, B.; Chen, G. Preparation and application of magnetic biochar in water treatment: A critical review. *Sci. Total Environ.* **2020**, *711*, 134847. [[CrossRef](#)]
21. Cheng, B.-H.; Zeng, R.J.; Jiang, H. Recent developments of post-modification of biochar for electrochemical energy storage. *Bioresour. Technol.* **2017**, *246*, 224–233. [[CrossRef](#)]
22. Lobos, M.L.N.; Sieben, J.M.; Comignani, V.; Duarte, M.; Volpe, M.A.; Moyano, E.L. Biochar from pyrolysis of cellulose: An alternative catalyst support for the electro-oxidation of methanol. *Int. J. Hydrog. Energy* **2016**, *41*, 10695–10706. [[CrossRef](#)]
23. Yue, Y.; Lin, Q.; Irfan, M.; Chen, Q.; Zhao, X. Characteristics and potential values of bio-oil, syngas and biochar derived from *Salsola collina* Pall. in a fixed bed slow pyrolysis system. *Bioresour. Technol.* **2016**, *220*, 378–383. [[CrossRef](#)]
24. Brewer, C.E.; Schmidt-Rohr, K.; Satrio, J.A.; Brown, R.C. Characterization of biochar from fast pyrolysis and gasification systems. *Environ. Prog. Sustain. Energy* **2009**, *28*, 386–396. [[CrossRef](#)]
25. You, S.; Ok, Y.S.; Chen, S.S.; Tsang, D.C.; Kwon, E.E.; Lee, J.; Wang, C.-H. A critical review on sustainable biochar system through gasification: Energy and environmental applications. *Bioresour. Technol.* **2017**, *246*, 242–253. [[CrossRef](#)]
26. Kim, D.; Lee, K.; Park, K.Y. Upgrading the characteristics of biochar from cellulose, lignin, and xylan for solid biofuel production from biomass by hydrothermal carbonization. *J. Ind. Eng. Chem.* **2016**, *42*, 95–100. [[CrossRef](#)]
27. Hossain, N.; Nizamuddin, S.; Griffin, G.; Selvakannan, P.; Mubarak, N.M.; Mahlia, T.M.I. Synthesis and characterization of rice husk biochar via hydrothermal carbonization for wastewater treatment and biofuel production. *Sci. Rep.* **2020**, *10*, 1–15. [[CrossRef](#)]
28. Cha, J.S.; Park, S.H.; Jung, S.-C.; Ryu, C.; Jeon, J.-K.; Shin, M.-C.; Park, Y.-K. Production and utilization of biochar: A review. *J. Ind. Eng. Chem.* **2016**, *40*, 1–15. [[CrossRef](#)]
29. Cao, X.; Sun, S.; Sun, R.J.R. Application of biochar-based catalysts in biomass upgrading: A review. *RSC Adv.* **2017**, *7*, 48793–48805. [[CrossRef](#)]
30. Peixoto, A.F.; Ramos, R.; Moreira, M.M.; Soares, O.S.G.P.; Ribeiro, L.S.; Pereira, M.F.R.; Delerue-Matos, C.; Freire, C. Production of ethyl levulinate fuel bioadditive from 5-hydroxymethylfurfural over sulfonic acid functionalized biochar catalysts. *Fuel* **2021**, *303*, 121227. [[CrossRef](#)]
31. Xiong, X.; Iris, K.; Cao, L.; Tsang, D.C.; Zhang, S.; Ok, Y.S. A review of biochar-based catalysts for chemical synthesis, biofuel production, and pollution control. *Bioresour. Technol.* **2017**, *246*, 254–270. [[CrossRef](#)]
32. Cheng, F.; Li, X. Preparation and application of biochar-based catalysts for biofuel production. *Catalysts* **2018**, *8*, 346. [[CrossRef](#)]
33. Li, R.; Shahbazi, A.; Wang, L.; Zhang, B.; Chung, C.-C.; Dayton, D.; Yan, Q. Nanostructured molybdenum carbide on biochar for CO₂ reforming of CH₄. *Fuel* **2018**, *225*, 403–410. [[CrossRef](#)]
34. Thompson, E.; Danks, A.; Bourgeois, L.; Schnepf, Z. Iron-catalyzed graphitization of biomass. *Green Chem.* **2015**, *17*, 551–556. [[CrossRef](#)]
35. Wang, Y.-Y.; Ling, L.-L.; Jiang, H. Selective hydrogenation of lignin to produce chemical commodities by using a biochar supported Ni–Mo₂C catalyst obtained from biomass. *Green Chem.* **2016**, *18*, 4032–4041. [[CrossRef](#)]
36. Shan, R.; Han, J.; Gu, J.; Yuan, H.; Luo, B.; Chen, Y. A review of recent developments in catalytic applications of biochar-based materials. *Resour. Conserv. Recycl.* **2020**, *162*, 105036. [[CrossRef](#)]
37. Kumar, M.; Xiong, X.; Sun, Y.; Yu, I.K.; Tsang, D.C.; Hou, D.; Gupta, J.; Bhaskar, T.; Pandey, A. Critical review on biochar-supported catalysts for pollutant degradation and sustainable biorefinery. *Adv. Sustain. Syst.* **2020**, *4*, 1900149. [[CrossRef](#)]
38. Dehkhoda, A.M.; West, A.H.; Ellis, N. Biochar-based solid acid catalyst for biodiesel production. *Appl. Catal. A Gen.* **2010**, *382*, 197–204. [[CrossRef](#)]

39. Wang, S.; Zhao, C.; Shan, R.; Wang, Y.; Yuan, H. A novel peat biochar supported catalyst for the transesterification reaction. *Energy Convers. Manag.* **2017**, *139*, 89–96. [[CrossRef](#)]
40. Zhao, C.; Lv, P.; Yang, L.; Xing, S.; Luo, W.; Wang, Z. Biodiesel synthesis over biochar-based catalyst from biomass waste pomelo peel. *Energy Convers. Manag.* **2018**, *160*, 477–485. [[CrossRef](#)]
41. Dhawane, S.H.; Kumar, T.; Halder, G. Central composite design approach towards optimization of flamboyant pods derived steam activated carbon for its use as heterogeneous catalyst in transesterification of Hevea brasiliensis oil. *Energy Convers. Manag.* **2015**, *100*, 277–287. [[CrossRef](#)]
42. di Bitonto, L.; Reynel-Ávila, H.E.; Mendoza-Castillo, D.I.; Bonilla-Petriciolet, A.; Durán-Valle, C.J.; Pastore, C. Synthesis and characterization of nanostructured calcium oxides supported onto biochar and their application as catalysts for biodiesel production. *Renew. Energy* **2020**, *160*, 52–66. [[CrossRef](#)]
43. Zhang, F.; Wu, X.-H.; Yao, M.; Fang, Z.; Wang, Y.-T. Production of biodiesel and hydrogen from plant oil catalyzed by magnetic carbon-supported nickel and sodium silicate. *Green Chem.* **2016**, *18*, 3302–3314. [[CrossRef](#)]
44. Hazmi, B.; Rashid, U.; Ibrahim, M.L.; Nehdi, I.A.; Azam, M.; Al-Resayes, S.I. Synthesis and characterization of bifunctional magnetic nano-catalyst from rice husk for production of biodiesel. *Environ. Technol. Innov.* **2021**, *21*, 101296. [[CrossRef](#)]
45. Tantirungrotechai, J.; Thepwatee, S.; Yoosuk, B. Biodiesel synthesis over Sr/MgO solid base catalyst. *Fuel* **2013**, *106*, 279–284. [[CrossRef](#)]
46. Zhao, C.; Yang, L.; Xing, S.; Luo, W.; Wang, Z.; Lv, P. Biodiesel production by a highly effective renewable catalyst from pyrolytic rice husk. *J. Clean. Prod.* **2018**, *199*, 772–780. [[CrossRef](#)]
47. Liu, G.-H.; Zong, Z.-M.; Liu, Z.-Q.; Liu, F.-J.; Zhang, Y.-Y.; Wei, X.-Y. Solvent-controlled selective hydrodeoxygenation of bio-derived guaiacol to arenes or phenols over a biochar supported Co-doped MoO₂ catalyst. *Fuel Process. Technol.* **2018**, *179*, 114–123. [[CrossRef](#)]
48. Casoni, A.I.; Hoch, P.M.; Volpe, M.A.; Gutierrez, V.S. Catalytic conversion of furfural from pyrolysis of sunflower seed hulls for producing bio-based furfuryl alcohol. *J. Clean. Prod.* **2018**, *178*, 237–246. [[CrossRef](#)]
49. Ido, A.L.; de Luna, M.D.G.; Ong, D.C.; Capareda, S.C. Upgrading of Scenedesmus obliquus oil to high-quality liquid-phase biofuel by nickel-impregnated biochar catalyst. *J. Clean. Prod.* **2019**, *209*, 1052–1060. [[CrossRef](#)]
50. Lee, Y.; Lee, S.W.; Tsang, Y.F.; Kim, Y.T.; Lee, J. Engineered rice-straw biochar catalysts for the production of value-added chemicals from furan. *Chem. Eng. J.* **2020**, *387*, 124194. [[CrossRef](#)]
51. Lee, Y.; Kim, Y.T.; Kwon, E.E.; Lee, J. Biochar as a catalytic material for the production of 1,4-butanediol and tetrahydrofuran from furan. *Environ. Res.* **2020**, *184*, 109325. [[CrossRef](#)]
52. Zhu, C.; Wang, H.; Li, H.; Cai, B.; Lv, W.; Cai, C.; Wang, C.; Yan, L.; Liu, Q.; Ma, L. Selective Hydrodeoxygenation of 5-Hydroxymethylfurfural to 2,5-Dimethylfuran over Alloyed Cu–Ni Encapsulated in Biochar Catalysts. *ACS Sustain. Chem. Eng.* **2019**, *7*, 19556–19569. [[CrossRef](#)]
53. Chen, T.; Li, D.; Jiang, H.; Xiong, C. High-performance Pd nanoalloy on functionalized activated carbon for the hydrogenation of nitroaromatic compounds. *Chem. Eng. J.* **2015**, *259*, 161–169. [[CrossRef](#)]
54. Santos, J.L.; Mäki-Arvela, P.; Monzón, A.; Murzin, D.Y.; Centeno, M.Á. Metal catalysts supported on biochars: Part I synthesis and characterization. *Appl. Catal. B Environ.* **2020**, *268*, 118423. [[CrossRef](#)]
55. Santos, J.L.; Mäki-Arvela, P.; Wärnå, J.; Monzón, A.; Centeno, M.A.; Murzin, D.Y. Hydrodeoxygenation of vanillin over noble metal catalyst supported on biochars: Part II: Catalytic behavior. *Appl. Catal. B Environ.* **2020**, *268*, 118425. [[CrossRef](#)]
56. Kostyniuk, A.; Grilc, M.; Likozar, B. Catalytic Cracking of biomass-derived hydrocarbon tars or model compounds to form biobased benzene, toluene, and xylene isomer mixtures. *Ind. Eng. Chem. Res.* **2019**, *58*, 7690–7705. [[CrossRef](#)]
57. Gómez-Barea, A.; Leckner, B. Gasification of biomass and waste. In *Handbook of Combustion*; Wiley & Sons: Hoboken, NJ, USA, 2010; pp. 365–397.
58. Shen, Y.; Yoshikawa, K. Tar conversion and vapor upgrading via in situ catalysis using silica-based nickel nanoparticles embedded in rice husk char for biomass pyrolysis/gasification. *Ind. Eng. Chem. Res.* **2014**, *53*, 10929–10942. [[CrossRef](#)]
59. Shen, Y.; Areeprasert, C.; Prabowo, B.; Takahashi, F.; Yoshikawa, K. Metal nickel nanoparticles in situ generated in rice husk char for catalytic reformation of tar and syngas from biomass pyrolytic gasification. *RSC Adv.* **2014**, *4*, 40651–40664. [[CrossRef](#)]
60. Shen, Y.; Zhao, P.; Shao, Q.; Ma, D.; Takahashi, F.; Yoshikawa, K. In-situ catalytic conversion of tar using rice husk char-supported nickel-iron catalysts for biomass pyrolysis/gasification. *Appl. Catal. B Environ.* **2014**, *152–153*, 140–151. [[CrossRef](#)]
61. Chen, J.; Wang, M.; Wang, S.; Li, X. Hydrogen production via steam reforming of acetic acid over biochar-supported nickel catalysts. *Int. J. Hydrog. Energy* **2018**, *43*, 18160–18168. [[CrossRef](#)]
62. Qian, K.; Kumar, A. Reforming of lignin-derived tars over char-based catalyst using Py-GC/MS. *Fuel* **2015**, *162*, 47–54. [[CrossRef](#)]
63. Qian, K.; Kumar, A. Catalytic reforming of toluene and naphthalene (model tar) by char supported nickel catalyst. *Fuel* **2017**, *187*, 128–136. [[CrossRef](#)]
64. Yao, D.; Hu, Q.; Wang, D.; Yang, H.; Wu, C.; Wang, X.; Chen, H. Hydrogen production from biomass gasification using biochar as a catalyst/support. *Bioresour. Technol.* **2016**, *216*, 159–164. [[CrossRef](#)] [[PubMed](#)]
65. Kastner, J.R.; Mani, S.; Juneja, A. Catalytic decomposition of tar using iron supported biochar. *Fuel Process. Technol.* **2015**, *130*, 31–37. [[CrossRef](#)]
66. Zhang, S.; Asadullah, M.; Dong, L.; Tay, H.-L.; Li, C.-Z. An advanced biomass gasification technology with integrated catalytic hot gas cleaning. Part II: Tar reforming using char as a catalyst or as a catalyst support. *Fuel* **2013**, *112*, 646–653. [[CrossRef](#)]

67. Wang, X.-B.; Yang, S.-Q.; Xu, C.; Ma, H.-D.; Zhang, Z.-H.; Du, Z.-Y.; Li, W.-Y. Effect of boron doping on the performance of Ni/Biochar catalysts for steam reforming of toluene as a tar model compound. *J. Anal. Appl. Pyrolysis* **2021**, *155*, 105033. [CrossRef]
68. Kaewpanha, M.; Guan, G.; Ma, Y.; Hao, X.; Zhang, Z.; Reubroychareon, P.; Kusakabe, K.; Abudula, A. Hydrogen production by steam reforming of biomass tar over biomass char supported molybdenum carbide catalyst. *Int. J. Hydrog. Energy* **2015**, *40*, 7974–7982. [CrossRef]
69. Postma, R.S.; Kersten, S.R.A.; van Rossum, G. Potassium-salt-catalyzed tar reduction during pyrolysis oil gasification. *Ind. Eng. Chem. Res.* **2016**, *55*, 7226–7230. [CrossRef]
70. Yan, Q.; Lu, Y.; To, F.; Li, Y.; Yu, F. Synthesis of tungsten carbide nanoparticles in biochar matrix as a catalyst for dry reforming of methane to syngas. *Catal. Sci. Technol.* **2015**, *5*, 3270–3280. [CrossRef]
71. Chen, Y.H.; Schmid, M.; Chang, C.C.; Chang, C.Y.; Scheffknecht, G. Lab-scale investigation of palm shell char as tar reforming catalyst. *Catalysts* **2020**, *10*, 25. [CrossRef]
72. Du, Z.Y.; Zhang, Z.H.; Xu, C.; Wang, X.B.; Li, W.Y. Low-temperature steam reforming of toluene and biomass tar over biochar-supported Ni nanoparticles. *ACS Sustain. Chem. Eng.* **2019**, *7*, 3111. [CrossRef]
73. Świerczyński, D.; Libs, S.; Courson, C.; Kiennemann, A. Steam reforming of tar from a biomass gasification process over Ni/olivine catalyst using toluene as a model compound. *Appl. Catal. B—Environ.* **2007**, *74*, 211–222. [CrossRef]
74. Li, J.; Tao, J.; Yan, B.; Jiao, L.; Chen, G.; Hu, J. Review of microwave-based treatments of biomass gasification tar. *Renew. Sustain. Energy Rev.* **2021**, *150*, 111510. [CrossRef]
75. Richardson, Y.; Motuzas, J.; Julbe, A.; Volle, G.; Blin, J. Catalytic investigation of in situ generated Ni metal nanoparticles for Tar conversion during biomass pyrolysis. *J. Phys. Chem. C* **2013**, *117*, 23812–23831. [CrossRef]
76. Richardson, Y.; Blin, J.; Volle, G.; Motuzas, J.; Julbe, A. In situ generation of Ni metal nanoparticles as catalyst for H₂-rich syngas production from biomass gasification. *Appl. Catal. A Gen.* **2010**, *382*, 220–230. [CrossRef]
77. Poggi, L.A.; Singh, K. Thermal degradation capabilities of modified bio-chars and fluid cracking catalyst (FCC) for acetic acid. *Biomass Bioenergy* **2016**, *90*, 243–251. [CrossRef]
78. Guizani, C.; Escudero Sanz, F.J.; Salvador, S. The nature of the deposited carbon at methane cracking over a nickel loaded wood-char. *C. R. Chim.* **2016**, *19*, 423–432. [CrossRef]
79. Nejati, B.; Adami, P.; Bozorg, A.; Tavasoli, A.; Mirzahosseini, A.H. Catalytic pyrolysis and bio-products upgrading derived from *Chlorella vulgaris* over its biochar and activated biochar-supported Fe catalysts. *J. Anal. Appl. Pyrolysis* **2020**, *152*, 104799. [CrossRef]
80. Liu, Q.-Y.; Yang, F.; Liu, Z.-H.; Li, G. Preparation of SnO₂-Co₃O₄/C biochar catalyst as a Lewis acid for corncob hydrolysis into furfural in water medium. *J. Ind. Eng. Chem.* **2015**, *26*, 46–54. [CrossRef]
81. Zhang, C.; Fu, Z.; Dai, B.; Zen, S.; Liu, Y.; Xu, Q.; Kirk, S.R.; Yin, D. Biochar sulfonic acid immobilized chlorozincate ionic liquid: An efficiently biomimetic and reusable catalyst for hydrolysis of cellulose and bamboo under microwave irradiation. *Cellulose* **2014**, *21*, 1227–1237. [CrossRef]
82. Zhang, C.; Fu, Z.; Dai, B.; Zen, S.; Liu, Y.; Xu, Q.; Kirk, S.R.; Yin, D. Chlorocuprate ionic liquid functionalized biochar sulfonic acid as an efficiently biomimetic catalyst for direct hydrolysis of bamboo under microwave irradiation. *Ind. Eng. Chem. Res.* **2013**, *52*, 11537–11543. [CrossRef]
83. Wei, Y.; Shen, C.; Xie, J.; Bu, Q. Study on reaction mechanism of superior bamboo biochar catalyst production by molten alkali carbonates pyrolysis and its application for cellulose hydrolysis. *Sci. Total Environ.* **2020**, *712*, 136435. [CrossRef] [PubMed]
84. Yan, Q.; Wan, C.; Liu, J.; Gao, J.; Yu, F.; Zhang, J.; Cai, Z. Iron nanoparticles in situ encapsulated in biochar-based carbon as an effective catalyst for the conversion of biomass-derived syngas to liquid hydrocarbons. *Green Chem.* **2013**, *15*, 1631. [CrossRef]
85. Wang, S.; Wang, H.; Yin, Q.; Zhu, L.; Yin, S. Methanation of bio-syngas over a biochar supported catalyst. *New J. Chem.* **2014**, *38*, 4471. [CrossRef]
86. Moazami, N.; Mahmoudi, H.; Rahbar, K.; Panahifar, P.; Tsolakis, A.; Wyszynski, M.L. Catalytic performance of cobalt-silica catalyst for Fischer-Tropsch synthesis: Effects of reaction rates on efficiency of liquid synthesis. *Chem. Eng. Sci.* **2015**, *134*, 374–384. [CrossRef]
87. Zhu, L.; Yin, S.; Yin, Q.; Wang, H.; Wang, S. Biochar: A new promising catalyst support using methanation as a probe reaction. *Energy Sci. Eng.* **2015**, *3*, 126–134. [CrossRef]
88. Enslow, K.R.; Bell, A.T. SnCl₄-catalyzed isomerization/dehydration of xylose and glucose to furanics in water. *Catal. Sci. Technol.* **2015**, *5*, 2839–2847. [CrossRef]
89. Yang, X.; Yu, I.K.M.; Cho, D.-W.; Chen, S.S.; Tsang, D.C.W.; Shang, J.; Yip, A.C.K.; Wang, L.; Ok, Y.S. Tin-Functionalized Wood Biochar as a Sustainable Solid Catalyst for Glucose Isomerization in Biorefinery. *ACS Sustain. Chem. Eng.* **2019**, *7*, 4851–4860. [CrossRef]
90. Iris, K.; Xiong, X.; Tsang, D.C.; Wang, L.; Hunt, A.J.; Song, H.; Shang, J.; Ok, Y.S.; Poon, C.S. Aluminium-biochar composites as sustainable heterogeneous catalysts for glucose isomerisation in a biorefinery. *Green Chem.* **2019**, *21*, 1267–1281. [CrossRef]
91. Sheng, K.; Zhang, S.; Liu, J.; Shuang, E.; Jin, C.; Xu, Z.; Zhang, X. Hydrothermal carbonization of cellulose and xylan into hydrochars and application on glucose isomerization. *J. Clean. Prod.* **2019**, *237*, 117831. [CrossRef]
92. Zhang, H.; Zhang, Z.; Luo, J.D.; Qi, X.T.; Yu, J.; Cai, J.X.; Yang, Z.Y. Molten-salt-assisted synthesis of hierarchical porous MnO@Biocarbon composites as promising electrode materials for supercapacitors and lithium-ion batteries. *Chemsuschem* **2019**, *12*, 283–290. [CrossRef]

93. Zhang, H.; Zhang, Z.; Qi, X.T.; Yu, J.; Cai, J.X.; Yang, Z.Y. Manganese monoxide/biomass-inherited porous carbon nanostructure composite based on the high water-absorbent agaric for asymmetric supercapacitor. *ACS Sustain. Chem. Eng.* **2019**, *7*, 4284–4294. [[CrossRef](#)]
94. Zhao, N.; Deng, L.B.; Luo, D.W.; Zhang, P.X. One-step fabrication of biomass-derived hierarchically porous carbon/MnO nanosheets composites for symmetric hybrid supercapacitor. *Appl. Surf. Sci.* **2020**, 526. [[CrossRef](#)]
95. Paravannoor, A. One-pot synthesis of biochar wrapped Ni/NiO nanobrick composites for supercapacitor applications. *J. Electroanal. Chem.* **2018**, *823*, 656–662. [[CrossRef](#)]
96. Golmohammadi, F.; Amiri, M. Facile synthesis of nanofiber composite based on biomass-derived material conjugated with nanoparticles of Ni-Co oxides for high-performance supercapacitors. *J. Mater. Sci. Mater. Electron.* **2020**, *31*, 2269–2279. [[CrossRef](#)]
97. Shi, Z.J.; Xing, L.; Liu, Y.; Gao, Y.F.; Liu, J.R. A porous biomass-based sandwich-structured Co_3O_4 @Carbon Fiber@ Co_3O_4 composite for high-performance supercapacitors. *Carbon* **2018**, *129*, 819–825. [[CrossRef](#)]
98. Thines, K.R.; Abdullah, E.C.; Ruthiraan, M.; Mubarak, N.M.; Tripathi, M. A new route of magnetic biochar-based polyaniline composites for supercapacitor electrode materials. *J. Anal. Appl. Pyrolysis* **2016**, *121*, 240–257. [[CrossRef](#)]
99. Thines, K.R.; Abdullah, E.C.; Mubarak, N.M.; Ruthiraan, M. In-situ polymerization of magnetic biochar polypyrrole composite: A novel application in supercapacitor. *Biomass Bioenergy* **2017**, *98*, 95–111. [[CrossRef](#)]
100. Zhao, G.; Cheng, Y.L.; Sun, P.X.; Ma, W.X.; Hao, S.H.; Wang, X.K.; Xu, X.J.; Xu, Q.Q.; Liu, M.Q. Biocarbon based template synthesis of uniform lamellar MoS_2 nanoflowers with excellent energy storage performance in lithium-ion battery and supercapacitors. *Electrochim. Acta* **2020**, *331*, 135262. [[CrossRef](#)]
101. Yang, Z.; Xiang, M.; Zhu, W.; Hui, J.; Qin, H.F. Biomass heteroatom carbon/cerium dioxide composite nanomaterials electrode for high-performance supercapacitors. *ACS Sustain. Chem. Eng.* **2020**, *8*, 6675–6681. [[CrossRef](#)]
102. Wang, Y.F.; Zhang, Y.; Pei, L.; Ying, D.W.; Xu, X.Y.; Zhao, L.; Jia, J.P.; Cao, X.D. Converting Ni-loaded biochars into supercapacitors: Implication on the reuse of exhausted carbonaceous sorbents. *Sci. Rep.* **2017**, *7*, 41523. [[CrossRef](#)]
103. Fu, M.; Zhu, Z.T.; Zhang, Z.H.; Zhuang, Q.R.; Chen, W.; Liu, Q.Y. Microwave deposition synthesis of $\text{Ni}(\text{OH})_2$ /sorghum stalk biomass carbon electrode materials for supercapacitors. *J. Alloy. Compd.* **2020**, *846*, 156376. [[CrossRef](#)]
104. Li, Q.; Lu, C.X.; Xiao, D.J.; Zhang, H.F.; Chen, C.M.; Xie, L.J.; Liu, Y.D.; Yuan, S.X.; Kong, Q.Q.; Zheng, K.; et al. β - $\text{Ni}(\text{OH})_2$ nanosheet arrays grown on biomass-derived hollow carbon microtubes for high-performance asymmetric supercapacitors. *ChemElectroChem* **2018**, *5*, 1279–1287. [[CrossRef](#)]
105. Nagaraju, G.; Cha, S.M.; Yu, J.S. Ultrathin nickel hydroxide nanosheet arrays grafted biomass-derived honeycomblike porous carbon with improved electrochemical performance as a supercapacitive material. *Sci. Rep.* **2017**, *7*, 45201. [[CrossRef](#)]
106. Nguyen, N.T.; Le, P.A.; Phung, V.B.T. Biomass-derived carbon hooks on Ni foam with free binder for high performance supercapacitor electrode. *Chem. Eng. Sci.* **2021**, *229*, 116053. [[CrossRef](#)]
107. Wang, H.L.; Wen, J. Biomass porous carbon-based composite for high performance supercapacitor. *Mater. Res. Express* **2020**, *7*, 442. [[CrossRef](#)]
108. Yang, H.F.; Tang, Y.H.; Sun, X.Y.; Liu, Q.; Huang, X.G.; Wang, L.X.; Fu, Z.X.; Zhang, Q.T.; Or, S.W. Biomass-derived porous carbon materials with NiS nanoparticles for high performance supercapacitors. *J. Mater. Sci. Mater. Electron.* **2017**, *28*, 14874–14883. [[CrossRef](#)]
109. Golmohammadi, F.; Amiri, M. Biomass-derived graphene-based nanocomposite: A facile template for decoration of ultrathin nickel-aluminum layered double hydroxide nanosheets as high-performance supercapacitors. *Int. J. Hydrog. Energy* **2020**, *45*, 15578–15588. [[CrossRef](#)]
110. Zhang, M.M.; Song, Z.X.; Liu, H.; Ma, T.J. Biomass-derived highly porous nitrogen-doped graphene orderly supported NiMn_2O_4 nanocrystals as efficient electrode materials for asymmetric supercapacitors. *Appl. Surf. Sci.* **2020**, *507*, 145065. [[CrossRef](#)]
111. Zhang, S.D.; Liu, J.; Huang, P.P.; Wang, H.; Cao, C.Y.; Song, W.G. Carbonaceous aerogel and CoNiAl-LDH@CA nanocomposites derived from biomass for high performance pseudo-supercapacitor. *Sci. Bull.* **2017**, *62*, 841–845. [[CrossRef](#)]
112. Guo, D.X.; Zhang, L.; Song, X.M.; Tan, L.C.; Ma, H.Y.; Jiao, J.; Zhu, D.; Li, F.B. NiCo_2O_4 nanosheets grown on interconnected honeycomb-like porous biomass carbon for high performance asymmetric supercapacitors. *N. J. Chem.* **2018**, *42*, 8478–8484. [[CrossRef](#)]
113. Nan, J.X.; Shi, Y.; Xiang, Z.Q.; Wang, S.; Yang, J.W.; Zhang, B. Ultrathin NiCo_2O_4 nanosheets assembled on biomass-derived carbon microsheets with polydopamine for high-performance hybrid supercapacitors. *Electrochim. Acta* **2019**, *301*, 107–116. [[CrossRef](#)]
114. Wang, K.; Yan, R.; Tian, X.D.; Wang, Y.; Lei, S.W.; Li, X.; Yang, T.; Wang, X.J.; Song, Y.; Liu, Y.Q.; et al. Multi-scale biomass-based carbon microtubes decorated with Ni-Co sulphides nanoparticles for supercapacitors with high rate performance. *Electrochim. Acta* **2019**, *302*, 78–91. [[CrossRef](#)]
115. Ouyang, Y.H.; Xing, T.; Chen, Y.L.; Zheng, L.P.; Peng, J.; Wu, C.; Chang, B.B.; Luo, Z.G.; Wang, X.Y. Hierarchically structured spherical nickel cobalt layered double hydroxides particles grown on biomass porous carbon as an advanced electrode for high specific energy asymmetric supercapacitor. *J. Energy Storage* **2020**, *30*, 10154. [[CrossRef](#)]
116. Zhang, D.; Guo, X.M.; Tong, X.Z.; Chen, Y.F.; Duan, M.T.; Shi, J.; Jiang, C.W.; Hu, L.L.; Kong, Q.H.; Zhang, J.H. High-performance battery-type supercapacitor based on porous biocarbon and biocarbon supported Ni-Co layered double hydroxide. *J. Alloy. Compd.* **2020**, *837*, 155529. [[CrossRef](#)]

117. Chen, H.; Zhao, L.; Fang, W.; Li, W.X.; He, X.A.; Zhang, F.Q. Construction of hierarchical NiCo₂S₄ nanowires on 3D biomass carbon for high-performance supercapacitors. *J. Mater. Sci. Mater. Electron.* **2018**, *29*, 9573–9581. [[CrossRef](#)]
118. Wang, Q.S.; Zhang, Y.F.; Jiang, H.M.; Meng, C.G. In-situ grown manganese silicate from biomass-derived heteroatom-doped porous carbon for supercapacitors with high performance. *J. Colloid Interface Sci.* **2019**, *534*, 142–155. [[CrossRef](#)]
119. Ren, Y.M.; Xu, Q.; Zhang, J.M.; Yang, H.X.; Wang, B.; Yang, D.Y.; Hu, J.H.; Liu, Z.M. Functionalization of biomass carbonaceous aerogels: Selective preparation of MnO₂@CA composites for supercapacitors. *ACS Appl. Mater. Interfaces* **2014**, *6*, 9689–9697. [[CrossRef](#)]
120. Li, Y.J.; Yu, N.; Yan, P.; Li, Y.G.; Zhou, X.M.; Chen, S.L.; Wang, G.L.; Wei, T.; Fan, Z.J. Fabrication of manganese dioxide nanoplates anchoring on biomass-derived cross-linked carbon nanosheets for high-performance asymmetric supercapacitors. *J. Power Sources* **2015**, *300*, 309–317. [[CrossRef](#)]
121. Wan, C.C.; Jiao, Y.; Li, J. Core-shell composite of wood-derived biochar supported MnO₂ nanosheets for supercapacitor applications. *RSC Adv.* **2016**, *6*, 64811–64817. [[CrossRef](#)]
122. Chen, J.; Qiu, J.H.; Wang, B.; Feng, H.X.; Yu, Y.L.; Sakai, E. Manganese dioxide/biocarbon composites with superior performance in supercapacitors. *J. Electroanal. Chem.* **2017**, *791*, 159–166. [[CrossRef](#)]
123. Yang, M.H.; Kim, D.S.; Hong, S.B.; Sim, J.W.; Kim, J.; Kim, S.S.; Choi, B.G. MnO₂ nanowire/biomass-derived carbon from hemp stem for high-performance supercapacitors. *Langmuir* **2017**, *33*, 5140–5147. [[CrossRef](#)]
124. Yang, G.J.; Park, S.J. MnO₂ and biomass-derived 3D porous carbon composites electrodes for high performance supercapacitor applications. *J. Alloy. Compd.* **2018**, *741*, 360–367. [[CrossRef](#)]
125. Fang, K.L.; Chen, J.Z.; Zhou, X.Y.; Mei, C.T.; Tian, Q.H.; Xu, J.L.; Wong, C.P. Decorating biomass-derived porous carbon with Fe₂O₃ ultrathin film for high-performance supercapacitors. *Electrochim. Acta* **2018**, *261*, 198–205. [[CrossRef](#)]
126. Yu, P.P.; Duan, W.; Jiang, Y.F. Porous Fe₂O₃ nanorods on hierarchical porous biomass carbon as advanced anode for high-energy-density asymmetric supercapacitors. *Front. Chem.* **2020**, *8*, 611852. [[CrossRef](#)]
127. Pourhosseini, S.E.M.; Norouzi, O.; Salimi, P.; Naderi, H.R. Synthesis of a novel interconnected 3D pore network algal biochar constituting iron nanoparticles derived from a harmful marine biomass as high-performance asymmetric supercapacitor electrodes. *ACS Sustain. Chem. Eng.* **2018**, *6*, 4746–4758. [[CrossRef](#)]
128. Chen, J.; Qiu, J.H.; Wang, B.; Feng, H.X.; Ito, K.; Sakai, E. Fe₃O₄/biocarbon composites with superior performance in supercapacitors. *J. Electroanal. Chem.* **2017**, *804*, 232–239. [[CrossRef](#)]
129. Fu, M.; Chen, W.; Ding, J.X.; Zhu, X.X.; Liu, Q.Y. Biomass waste derived multi-hierarchical porous carbon combined with CoFe₂O₄ as advanced electrode materials for supercapacitors. *J. Alloy. Compd.* **2019**, *782*, 952–960. [[CrossRef](#)]
130. Liu, W.; Fan, H.L.; Shen, W.Z.; Qu, S.J. Facile and Sustainable Synthesis of Co₃O₄@ hollow-carbon-fiber for a binder-free supercapacitor electrode. *Chem. Select* **2016**, *1*, 6469–6475. [[CrossRef](#)]
131. Zhang, C.Y.; Huang, L.N.; Zhao, Y.Y.; Su, L.; Li, J.N.; Qin, H.F. Biomass carbon-modified CoZn/C as a high-performance electrode for supercapacitors. *Ionics* **2020**, *26*, 5179–5188. [[CrossRef](#)]
132. Zhang, Y.F.; Jiang, H.M.; Wang, Q.S.; Meng, C.G. In-situ hydrothermal growth of Zn₄Si₂O₇(OH)₂·H₂O anchored on 3D N, S-enriched carbon derived from plant biomass for flexible solid-state asymmetrical supercapacitors. *Chem. Eng. J.* **2018**, *352*, 519–529. [[CrossRef](#)]
133. Wang, Q.S.; Zhang, Y.F.; Xiao, J.Q.; Jiang, H.M.; Hu, T.; Meng, C.G. Copper oxide/cuprous oxide/hierarchical porous biomass-derived carbon hybrid composites for high-performance supercapacitor electrode. *J. Alloy. Compd.* **2019**, *782*, 1103–1113. [[CrossRef](#)]
134. Genovese, M.; Lian, K. Polyoxometalate modified pine cone biochar carbon for supercapacitor electrodes. *J. Mater. Chem. A* **2017**, *5*, 3939–3947. [[CrossRef](#)]
135. Kaushal, I.; Maken, S.; Sharma, A.K. SnO₂ mixed banana peel derived biochar composite for supercapacitor application. *Korean Chem. Eng. Res.* **2018**, *56*, 694–704. [[CrossRef](#)]
136. Kouchachvili, L.; Entchev, E. Ag/Biochar composite for supercapacitor electrodes. *Mater. Today Energy* **2017**, *6*, 136–145. [[CrossRef](#)]
137. Yuan, H.R.; Chen, H.B.; Li, D.N.; Deng, L.F.; Chen, J.; Fan, Y.K.; He, M.Y.; Sun, F. Catalytic synthesis and simultaneous co-doping of hierarchically porous carbon with in-situ coated graphene from biomass tar as efficient catalyst for ORR. *Electrochem. Commun.* **2019**, *100*, 52–59. [[CrossRef](#)]
138. Liu, Y.; Su, M.J.; Li, D.H.; Li, S.S.; Li, X.Y.; Zhao, J.W.; Liu, F.J. Soybean straw biomass-derived Fe-N co-doped porous carbon as an efficient electrocatalyst for oxygen reduction in both alkaline and acidic media. *RSC Adv.* **2020**, *10*, 6763–6771. [[CrossRef](#)]
139. Hoang, V.C.; Gomes, V.G.; Dinh, K.N. Ni- and P-doped carbon from waste biomass: A sustainable multifunctional electrode for oxygen reduction, oxygen evolution and hydrogen evolution reactions. *Electrochim. Acta* **2019**, *314*, 49–60. [[CrossRef](#)]
140. Gao, Y.; Hu, S.Q.; Zhou, Y.G.; Zhang, S.G. Template-free synthesis of biomass-derived hierarchically mesoporous carbon with ultra-small FeNi nanoparticles for oxygen evolution reaction. *Int. J. Hydrog. Energy* **2019**, *44*, 27806–27815. [[CrossRef](#)]
141. Freire, C.; Fernandes, D.M.; Nunes, M.; Abdelkader, V.K. POM & MOF-based electrocatalysts for energy-related reactions. *ChemCatChem* **2018**, *10*, 1703–1730. [[CrossRef](#)]
142. Hu, J.; Shi, Z.W.; Su, C.; Lu, B.Q.; Shao, Z.P.; Huang, H. Anchoring perovskite LaMnO₃ nanoparticles on biomass-derived N, P co-doped porous carbon for efficient oxygen reduction. *Electrochim. Acta* **2018**, *274*, 40–48. [[CrossRef](#)]
143. Hu, S.N.; Tan, Y.; Feng, C.Q.; Wang, S.Q.; Sun, Z.G.; Wu, H.M.; Zhang, G.X. Improving biomass-derived carbon with cobalt/cobalt oxide doping for oxygen reduction reaction. *J. Solid State Electrochem.* **2019**, *23*, 2291–2299. [[CrossRef](#)]

144. Borghei, M.; Lehtonen, J.; Liu, L.; Rojas, O.J. Advanced biomass-derived electrocatalysts for the oxygen reduction reaction. *Adv. Mater.* **2018**, *30*, 27. [CrossRef]
145. Nemiwal, M.; Zhang, T.C.; Kumar, D. Graphene-based electrocatalysts: Hydrogen evolution reactions and overall water splitting. *Int. J. Hydrog. Energy* **2021**, *46*, 10161–10588. [CrossRef]
146. Lee, D.W.; Jang, J.H.; Jang, I.; Kang, Y.S.; Jang, S.; Lee, K.Y.; Jang, J.H.; Kim, H.J.; Yoo, S.J. Bio-derived Co₂P nanoparticles supported on nitrogen-doped carbon as promising oxygen reduction reaction electrocatalyst for anion exchange membrane fuel cells. *Small* **2019**, *15*, 8. [CrossRef]
147. An, K.L.; Xu, X.X.; Liu, X.X. Mo₂C-based electrocatalyst with biomass-derived sulfur and nitrogen Co-doped carbon as a matrix for hydrogen evolution and organic pollutant removal. *ACS Sustain. Chem. Eng.* **2018**, *6*, 1446–1455. [CrossRef]
148. Pavodi, F.; Tavakkoli, M.; Lahtinen, J.; Kallio, T. Straightforward synthesis of nitrogen-doped carbon nanotubes as highly active bifunctional electrocatalysts for full water splitting. *J. Catal.* **2017**, *353*, 19–27. [CrossRef]
149. Cheng, Y.; Xu, C.W.; Jia, L.C.; Gale, J.D.; Zhang, L.L.; Liu, C.; Shen, P.K.; Jiang, S.P. Pristine carbon nanotubes as non-metal electrocatalysts for oxygen evolution reaction of water splitting. *Appl. Catal. B—Environ.* **2015**, *163*, 96–104. [CrossRef]
150. Cui, W.; Liu, Q.; Cheng, N.Y.; Asiri, A.M.; Sun, X.P. Activated carbon nanotubes: A highly-active metal-free electrocatalyst for hydrogen evolution reaction. *Chem. Commun.* **2014**, *50*, 9340–9342. [CrossRef]
151. Yang, H.B.; Miao, J.W.; Hung, S.F.; Chen, J.Z.; Tao, H.B.; Wang, X.Z.; Zhang, L.P.; Chen, R.; Gao, J.J.; Chen, H.M.; et al. Identification of catalytic sites for oxygen reduction and oxygen evolution in N-doped graphene materials: Development of highly efficient metal-free bifunctional electrocatalyst. *Sci. Adv.* **2016**, *2*, 11. [CrossRef]
152. Zhang, W.; Wu, Z.Y.; Jiang, H.L.; Yu, S.H. Nanowire-Directed templating synthesis of metal-organic framework nanofibers and their derived porous doped carbon nanofibers for enhanced electrocatalysis. *J. Am. Chem. Soc.* **2014**, *136*, 14385–14388. [CrossRef]
153. Wu, M.G.; Wang, Y.Q.; Wei, Z.X.; Wang, L.; Zhuo, M.; Zhang, J.T.; Han, X.P.; Ma, J.M. Ternary doped porous carbon nanofibers with excellent ORR and OER performance for zinc-air batteries dagger. *J. Mater. Chem. A* **2018**, *6*, 10918–10925. [CrossRef]
154. Kordek, K.; Jiang, L.X.; Fan, K.C.; Zhu, Z.J.; Xu, L.; Al-Mamun, M.; Dou, Y.H.; Chen, S.; Liu, P.R.; Yin, H.J.; et al. Two-step activated carbon cloth with oxygen-rich functional groups as a high-performance additive-free air electrode for flexible zinc-air batteries. *Adv. Energy Mater.* **2019**, *9*, 9. [CrossRef]
155. Yan, X.C.; Jia, Y.; Odedairo, T.; Zhao, X.J.; Jin, Z.; Zhu, Z.H.; Yao, X.D. Activated carbon becomes active for oxygen reduction and hydrogen evolution reactions. *Chem. Commun.* **2016**, *52*, 8156–8159. [CrossRef]
156. Qiao, S.L.; Zhao, J.; Zhang, B.Y.; Liu, C.H.; Li, Z.; Hu, S.Z.; Li, Q. Micrometer-Scale biomass carbon tube matrix auxiliary MoS₂ heterojunction for electrocatalytic hydrogen evolution. *Int. J. Hydrog. Energy* **2019**, *44*, 32019–32029. [CrossRef]
157. Fan, Z.Y.; Li, J.; Yang, W.; Fu, Q.; Sun, K.; Song, Y.C.; Wei, Z.D.; Liao, Q.; Zhu, X. Green and facile synthesis of iron oxide nanoparticle-embedded N-doped biocarbon as an efficient oxygen reduction electrocatalyst for microbial fuel cells. *Chem. Eng. J.* **2020**, *385*, 10. [CrossRef]
158. Huggins, T.M.; Pietron, J.J.; Wang, H.M.; Ren, Z.J.; Biffinger, J.C. Graphitic biochar as a cathode electrocatalyst support for microbial fuel cells. *Bioresour. Technol.* **2015**, *195*, 147–153. [CrossRef]
159. Rahman, M.Z.; Edvinsson, T.; Kwong, P. Biochar for electrochemical applications. *Curr. Opin. Green Sustain. Chem.* **2020**, *23*, 25–30. [CrossRef]
160. Tran, T.; Song, M.Y.; Kang, T.H.; Samdani, J.; Park, H.Y.; Kim, H.; Jhung, S.H.; Yu, J.S. Iron phosphide incorporated into iron-treated heteroatoms-doped porous bio-carbon as efficient electrocatalyst for the oxygen reduction reaction. *ChemElectroChem* **2018**, *5*, 1944–1953. [CrossRef]
161. Pi, Y.T.; Xing, X.Y.; Lu, L.M.; He, Z.B.; Ren, T.Z. Hierarchical porous activated carbon in OER with high efficiency. *RSC Adv.* **2016**, *6*, 102422–102427. [CrossRef]
162. Prabu, N.; Kesavan, T.; Maduraiveeran, G.; Sasidharan, M. Bio-derived nanoporous activated carbon sheets as electrocatalyst for enhanced electrochemical water splitting. *Int. J. Hydrog. Energy* **2019**, *44*, 19995–20006. [CrossRef]
163. Gong, X.B.; Peng, L.; Wang, X.H.; Wu, L.L.; Liu, Y. Duckweed derived nitrogen self-doped porous carbon materials as cost-effective electrocatalysts for oxygen reduction reaction in microbial fuel cells. *Int. J. Hydrog. Energy* **2020**, *45*, 15336–15345. [CrossRef]
164. Li, M.; Zhang, H.G.; Xiao, T.F.; Wang, S.D.; Zhang, B.P.; Chen, D.Y.; Su, M.H.; Tang, J.F. Low-cost biochar derived from corncob as oxygen reduction catalyst in air cathode microbial fuel cells. *Electrochim. Acta* **2018**, *283*, 780–788. [CrossRef]
165. Humagain, G.; MacDougall, K.; MacInnis, J.; Lowe, J.M.; Coridan, R.H.; MacQuarrie, S.; Dasog, M. Highly efficient, biochar-derived molybdenum carbide hydrogen evolution electrocatalyst. *Adv. Energy Mater.* **2018**, *8*, 5. [CrossRef]
166. Xiong, X.L.; You, C.; Liu, Z.; Asiri, A.M.; Sun, X.P. Co-doped CuO Nanoarray: An efficient oxygen evolution reaction electrocatalyst with enhanced activity. *ACS Sustain. Chem. Eng.* **2018**, *6*, 2883–2887. [CrossRef]
167. Golmohammadi, F.; Amiri, M. Fabrication of MEA from biomass-based carbon nanofibers composited with nickel-cobalt oxides as a new electrocatalyst for oxygen reduction reaction in passive direct methanol fuel cells. *Electrocatalysis* **2021**, *11*, 485–496. [CrossRef]
168. Xiong, X.; Jiang, R.; Deng, B.W.; Yang, J.; Wang, D.H. Bionic structural design and electrochemical manufacture of WC/N-Doped carbon hybrids as efficient ORR catalyst. *J. Electrochem. Soc.* **2020**, *167*, 7. [CrossRef]
169. Zhao, W.T.; Lu, X.Q.; Selvaraj, M.; Wei, W.; Jiang, Z.F.; Ullah, N.; Liu, J.; Xie, J.M. MXP(M = Co/Ni)@carbon core-shell nanoparticles embedded in 3D cross-linked graphene aerogel derived from seaweed biomass for hydrogen evolution reaction. *Nanoscale* **2018**, *10*, 9698–9706. [CrossRef]

170. Hu, L.B.; Yu, F.; Wang, F.; Yang, S.C.; Peng, B.H.; Chen, L.; Wang, G.; Hou, J.; Dai, B.; Tian, Z.Q. Overwhelming electrochemical oxygen reduction reaction of zinc-nitrogen-carbon from biomass resource chitosan via a facile carbon bath method. *Chin. Chem. Lett.* **2020**, *31*, 1207–1212. [[CrossRef](#)]
171. Panganoron, H.O.; Pascasio, J.D.A.; Esparcia, E.A.; del Rosario, J.A.D.; Ocon, J.D. Hydrothermally carbonized waste biomass as electrocatalyst support for alpha-MnO₂ in oxygen reduction reaction. *Catalysts* **2020**, *10*, 18. [[CrossRef](#)]
172. Pi, L.; Jiang, R.; Cai, W.X.; Wang, L.; Wang, Y.Y.; Cai, J.H.; Mao, X.H. Bionic Preparation of CeO₂-Encapsulated nitrogen self-doped biochars for highly efficient oxygen reduction. *ACS Appl. Mater. Interfaces* **2020**, *12*, 3642–3653. [[CrossRef](#)] [[PubMed](#)]
173. Zhang, Y.Q.; Guo, C.Z.; Ma, Z.L.; Wu, H.J.; Chen, C.G. Inexpensive ipomoea aquatica biomass-modified carbon black as an active Pt-free electrocatalyst for oxygen reduction reaction in an alkaline medium. *Materials* **2015**, *8*, 6658–6667. [[CrossRef](#)] [[PubMed](#)]
174. Zhang, M.; Jin, X.; Wang, L.N.; Sun, M.J.; Tang, Y.; Chen, Y.M.; Sun, Y.Z.; Yang, X.J.; Wan, P.Y. Improving biomass-derived carbon by activation with nitrogen and cobalt for supercapacitors and oxygen reduction reaction. *Appl. Surf. Sci.* **2017**, *411*, 251–260. [[CrossRef](#)]
175. Xu, Z.Q.; Ma, J.H.; Shi, M.H.; Xie, Y.H.; Feng, C. Biomass based iron and nitrogen co-doped 3D porous carbon as an efficient oxygen reduction catalyst. *J. Colloid Interface Sci.* **2018**, *523*, 144–150. [[CrossRef](#)]
176. Wan, W.; Wang, Q.; Zhang, L.; Liang, H.W.; Chen, P.; Yu, S.H. N-, P- and Fe-tridoped nanoporous carbon derived from plant biomass: An excellent oxygen reduction electrocatalyst for zinc-air batteries. *J. Mater. Chem. A* **2016**, *4*, 8602–8609. [[CrossRef](#)]
177. Wu, X.X.; Chen, K.Q.; Lin, Z.P.; Zhang, Y.M.; Meng, H. Nitrogen doped graphitic carbon from biomass as non noble metal catalyst for oxygen reduction reaction. *Mater. Today Energy* **2019**, *13*, 100–108. [[CrossRef](#)]
178. Zhang, Z.P.; Gao, X.J.; Dou, M.L.; Ji, J.; Wang, F. Biomass derived N-doped porous carbon supported single Fe atoms as superior electrocatalysts for oxygen reduction. *Small* **2017**, *13*, 8. [[CrossRef](#)]
179. Jing, B.J.; You, S.J.; Ma, Y.Y.; Xing, Z.P.; Chen, H.; Dai, Y.; Zhang, C.Y.; Ren, N.Q.; Zou, J.L. Fe₃Se₄/FeSe heterojunctions in cornstalk-derived N-doped carbon framework enhance charge transfer and cathodic oxygen reduction reaction to boost bio-electricity generation. *Appl. Catal. B—Environ.* **2019**, *244*, 465–474. [[CrossRef](#)]
180. Lu, G.L.; Li, Z.Y.; Fan, W.X.; Wang, M.; Yang, S.C.; Li, J.Y.; Chang, Z.Y.; Sun, H.; Liang, S.; Liu, Z.N. Sponge-like N-doped carbon materials with Co-based nanoparticles derived from biomass as highly efficient electrocatalysts for the oxygen reduction reaction in alkaline media. *RSC Adv.* **2019**, *9*, 4843–4848. [[CrossRef](#)]
181. Hao, L.; Yu, J.; Xu, X.; Yang, L.; Xing, Z.P.; Dai, Y.; Sun, Y.; Zou, J.L. Nitrogen-doped MoS₂/carbon as highly oxygen-permeable and stable catalysts for oxygen reduction reaction in microbial fuel cells. *J. Power Sources* **2017**, *339*, 68–79. [[CrossRef](#)]
182. Chen, B.L.; Li, R.; Ma, G.P.; Gou, X.L.; Zhu, Y.Q.; Xia, Y.D. Cobalt sulfide/N,S codoped porous carbon core-shell nanocomposites as superior bifunctional electrocatalysts for oxygen reduction and evolution reactions. *Nanoscale* **2015**, *7*, 20674–20684. [[CrossRef](#)]
183. Wang, J.; Li, L.Q.; Chen, X.; Lu, Y.L.; Yang, W.S. Monodisperse cobalt sulfides embedded within nitrogen-doped carbon nanoflakes: An efficient and stable electrocatalyst for the oxygen reduction reaction. *J. Mater. Chem. A* **2016**, *4*, 11342–11350. [[CrossRef](#)]
184. Liu, B.; Qu, S.X.; Kou, Y.; Liu, Z.; Chen, X.; Wu, Y.T.; Han, X.P.; Deng, Y.D.; Hu, W.B.; Zhong, C. In situ electrodeposition of cobalt sulfide nanosheet arrays on carbon cloth as a highly efficient bifunctional electrocatalyst for oxygen evolution and reduction reactions. *ACS Appl. Mater. Interfaces* **2018**, *10*, 30433–30440. [[CrossRef](#)]
185. Shen, M.X.; Ruan, C.P.; Chen, Y.; Jiang, C.H.; Ai, K.L.; Lu, L.H. Covalent entrapment of cobalt-iron sulfides in N-Doped mesoporous carbon: Extraordinary bifunctional electrocatalysts for oxygen reduction and evolution reactions. *ACS Appl. Mater. Interfaces* **2015**, *7*, 1207–1218. [[CrossRef](#)]
186. Jiang, R.; Chen, X.; Deng, J.X.; Wang, T.Y.; Wang, K.; Chen, Y.L.; Jiang, J.Z. In-situ growth of ZnS/FeS heterojunctions on biomass-derived porous carbon for efficient oxygen reduction reaction. *J. Energy Chem.* **2020**, *47*, 79–85. [[CrossRef](#)]
187. Sun, Z.H.; Wang, Y.K.; Zhang, L.B.; Wu, H.; Jin, Y.C.; Li, Y.H.; Shi, Y.C.; Zhu, T.X.; Mao, H.; Liu, J.M.; et al. Simultaneously realizing rapid electron transfer and mass transport in jellyfish-like Mott-Schottky nanoreactors for oxygen reduction reaction. *Adv. Funct. Mater.* **2020**, *30*, 12. [[CrossRef](#)]
188. Lang, P.; Yuan, N.N.; Jiang, Q.Q.; Zhang, Y.C.; Tang, J.G. Recent advances and prospects of metal-based catalysts for oxygen reduction reaction. *Energy Technol.* **2020**, *8*, 18. [[CrossRef](#)]
189. Liu, Y.; Kelly, T.G.; Chen, J.G.G.; Mustain, W.E. Metal carbides as alternative electrocatalyst supports. *ACS Catal.* **2013**, *3*, 1184–1194. [[CrossRef](#)]
190. Li, M.; Xiong, Y.P.; Liu, X.T.; Han, C.; Zhang, Y.F.; Bo, X.J.; Guo, L.P. Iron and nitrogen co-doped carbon nanotube@hollow carbon fibers derived from plant biomass as efficient catalysts for the oxygen reduction reaction. *J. Mater. Chem. A* **2015**, *3*, 9658–9667. [[CrossRef](#)]
191. Ma, M.; You, S.J.; Wang, W.; Liu, G.S.; Qi, D.P.; Chen, X.D.; Qu, J.H.; Ren, N.Q. Biomass-derived porous Fe₃C/Tungsten carbide/graphitic carbon nanocomposite for efficient electrocatalysis of oxygen reduction. *ACS Appl. Mater. Interfaces* **2016**, *8*, 32307–32316. [[CrossRef](#)] [[PubMed](#)]
192. Kasturi, P.R.; Arunchander, A.; Kalpana, D.; Selvan, R.K. Bio-derived carbon as an efficient supporting electrocatalyst for the oxygen reduction reaction. *J. Phys. Chem. Solids* **2019**, *124*, 305–311. [[CrossRef](#)]
193. Gong, M.; Dai, H.J. A mini review of NiFe-based materials as highly active oxygen evolution reaction electrocatalysts. *Nano Res.* **2015**, *8*, 23–39. [[CrossRef](#)]

194. Guo, X.M.; Zhang, W.; Shi, R.H.; Zhu, H.W.; Qian, C.; Yang, H.X.; Zhang, J.H.; Yuan, A.H.; Zhou, Y.Z. Facile fabrication of amorphous Ni-P supported on a 3D biocarbon skeleton as an efficient electrocatalyst for the oxygen evolution reaction. *ChemElectroChem* **2019**, *6*, 3071–3076. [[CrossRef](#)]
195. Safizadeh, F.; Ghali, E.; Houlachi, G. Electrocatalysis developments for hydrogen evolution reaction in alkaline solutions-A Review. *Int. J. Hydrog. Energy* **2015**, *40*, 256–274. [[CrossRef](#)]
196. Zhao, G.Q.; Rui, K.; Dou, S.X.; Sun, W.P. Heterostructures for electrochemical hydrogen evolution reaction: A review. *Adv. Funct. Mater.* **2018**, *28*, 26. [[CrossRef](#)]
197. Wang, M.; Gonullu, Y.; Pyeon, M.; Diao, Z.D.; Czypiel, L.; Singh, M.; Shen, S.H.; Mathur, S. Trace amount of platinum supported on carbonized biomorphic wood for efficient electrochemical hydrogen evolution in alkaline condition. *Chem. Select* **2018**, *3*, 2140–2143. [[CrossRef](#)]
198. Min, S.X.; Duan, Y.; Li, Y.N.; Wang, F. Biomass-derived self-supported porous carbon membrane embedded with Co nanoparticles as an advanced electrocatalyst for efficient and robust hydrogen evolution reaction. *Renew. Energy* **2020**, *155*, 447–455. [[CrossRef](#)]
199. Guo, T.; Zhang, X.Y.; Liu, T.Y.; Wu, Z.Z.; Wang, D.Z. N, K Co-activated biochar-derived molybdenum carbide as efficient electrocatalysts for hydrogen evolution. *Appl. Surf. Sci.* **2020**, *509*, 8. [[CrossRef](#)]
200. Kannimuthu, K.; Sangeetha, K.; Sam Sankar, S.; Karmakar, A.; Madhu, R.; Kundu, S. Investigation on nanostructured Cu-based electrocatalysts for improvising water splitting: A review. *Inorg. Chem. Front.* **2021**, *8*, 234–272. [[CrossRef](#)]
201. Huang, H.; Yan, M.; Yang, C.; He, H.; Jiang, Q.; Yang, L.; Lu, Z.; Sun, Z.; Xu, X.; Bando, Y.; et al. Graphene nanoarchitectonics: Recent advances in graphene-based electrocatalysts for hydrogen evolution reaction. *Adv. Mater.* **2019**, *31*, 1903415. [[CrossRef](#)]
202. Yang, J.; Voiry, D.; Ahn, S.J.; Kang, D.; Kim, A.Y.; Chhowalla, M.; Shin, H.S. Two-dimensional hybrid nanosheets of tungsten disulfide and reduced graphene oxide as catalysts for enhanced hydrogen evolution. *Angew. Chem. Int. Ed.* **2013**, *52*, 13751–13754. [[CrossRef](#)]
203. Jaiswal, A.; Kumar, R.; Prakash, R. Iron/Iron carbide (Fe/Fe₃C) encapsulated in S, N codoped graphitic carbon as a robust HER electrocatalyst. *Energy Fuels* **2021**, *35*, 16046–16053. [[CrossRef](#)]
204. Wang, J.; Xu, F.; Jin, H.; Chen, Y.; Wang, Y. Non-noble metal-based carbon composites in hydrogen evolution reaction: Fundamentals to applications. *Adv. Mater.* **2017**, *29*, 1605838. [[CrossRef](#)]
205. Oh, N.K.; Seo, J.; Lee, S.; Kim, H.J.; Kim, U.; Lee, J.; Han, Y.K.; Park, H. Highly efficient and robust noble-metal free bifunctional water electrolysis catalyst achieved via complementary charge transfer. *Nat. Commun.* **2021**, *12*, 12. [[CrossRef](#)]
206. Jiang, Z.; Jiang, Z.-J.; Maiyalagan, T.; Manthiram, A. Cobalt oxide-coated N- and B-doped graphene hollow spheres as bifunctional electrocatalysts for oxygen reduction and oxygen evolution reactions. *J. Mater. Chem. A* **2016**, *4*, 5877–5889. [[CrossRef](#)]
207. Araujo, M.P.; Nunes, M.; Rocha, I.M.; Pereira, M.F.R.; Freire, C. Co₃O₄ nanoparticles anchored on selectively oxidized graphene flakes as bifunctional electrocatalysts for oxygen reactions. *Chem. Select* **2018**, *3*, 10064–10076. [[CrossRef](#)]
208. Wang, G.H.; Deng, Y.J.; Yu, J.N.; Zheng, L.; Du, L.; Song, H.Y.; Liao, S.J. From chlorella to nestlike framework constructed with doped carbon nanotubes: A biomass-derived, high-performance, bifunctional oxygen reduction/evolution catalyst. *ACS Appl. Mater. Interfaces* **2017**, *9*, 32168–32178. [[CrossRef](#)]
209. Yang, L.; Zeng, X.F.; Wang, D.; Cao, D.P. Biomass-derived FeNi alloy and nitrogen-codoped porous carbons as highly efficient oxygen reduction and evolution bifunctional electrocatalysts for rechargeable Zn-air battery. *Energy Storage Mater.* **2018**, *12*, 277–283. [[CrossRef](#)]
210. Lin, C.Q.; Kang, M.Z.; Zheng, L.Z.; Fu, X.Q.; Wang, S. Ammonium nitrate-assisted low-temperature synthesis of Co, Co₂P@CoP embedded in biomass-derived carbons as efficient electrocatalysts for hydrogen and oxygen evolution reaction. *Chem. Select* **2020**, *5*, 7338–7346. [[CrossRef](#)]
211. Yang, Z.; Yang, R.M.; Dong, G.X.; Xiang, M.; Hui, J.; Ou, J.F.; Qin, H.F. Biochar nanocomposite derived from watermelon peels for electrocatalytic hydrogen production. *ACS Omega* **2021**, *6*, 2066–2073. [[CrossRef](#)]
212. Liu, X.; Huo, Y.Q.; Yan, L.K.; Fan, N.; Cai, K.Z.; Su, Z.M. Hollow porous MnFe₂O₄ sphere grown on elm-money-derived biochar towards energy-saving full water electrolysis. *Chem. A Eur. J.* **2020**, *26*, 14397–14404. [[CrossRef](#)]